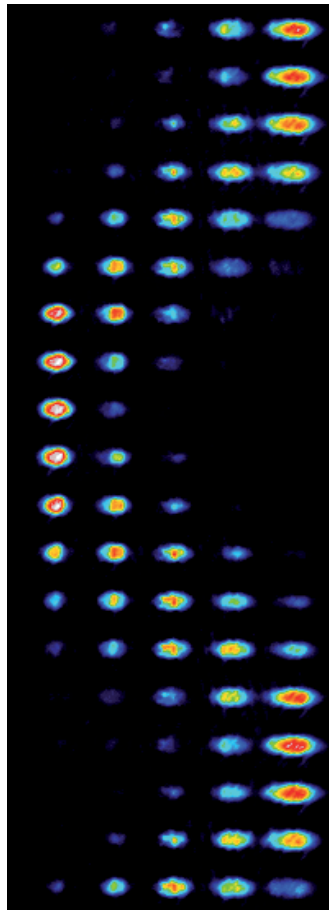


Ivan Herrera Benzaquén

Degenerate quantum gases production and coherent manipulation on atom chips



"I'm going to make him an offer he can't refuse."

VITO CORLEONE, *The Godfather*

Déjame citarte otros cuerpos cuya existencia
material deberás admitir aún siendo invisibles,

LUCRECIO *De la Naturaleza*

Degenerate quantum gases production and coherent manipulation on atom chips



Ivan Herrera Benzaquén
Departamento de Física de Materiales
Universidad Autónoma de Madrid

A thesis submitted for the degree of

Doctor of Philosophy

2012 November

Tutor: Francesco Cataliotti

Cotutor: José Manuel Calleja

Tribunal: Chiara Fort
Morgan Mitchell
Fernando Sols
Hermann Suderow
Luis Viña

Universidad Autónoma de Madrid
Departamento de Física de Materiales

The work described in this thesis was carried out in the group "Quantum Gases" at LENS Institute of the University of Florence in collaboration with Universidad Autónoma de Madrid.

Abstract

This thesis describes the creation of the first Bose-Einstein condensates (BEC) to be made on an **atom chip** in Italy and its integration with a **multi-state interferometer**. The theory, construction and optimization of the experiment are all detailed.

Like an electronic chip, an atom chip consists of an array of wires. The magnetic fields produced by the wires are used to trap and manipulate neutral atoms. Our atom chip was prepared in collaboration with the University of Wien, the rest of the experimental apparatus is built at the LENS Institute, University of Florence.

The condensate is produced using the magnetic field of a conductor on the chip surface and the interferometer exploits the near field produced by additional conductors integrated into the chip.

The atom chip was loaded with ^{87}Rb atoms cooled to $\sim 100 \mu\text{K}$ in a mirror-MOT formed 8 mm above the surface. After the loading process more than 2×10^7 atoms were trapped in a magnetic trap $\sim 200 \mu\text{m}$ above the surface. To reach Bose-Einstein condensation, the atoms were further cooled over 2.5 s using forced RF evaporative cooling. The condensate began to form at a temperature of $\sim 50 \text{ nK}$, and contained up to $\sim 3 \times 10^4$ atoms.

Matter-wave interferometry is a powerful tool for high-precision measurements of the quantum properties of atoms, many-body phenomena and gravity. The most precise matter-wave interferometers exploit the excellent localization in momentum space and coherence of the degenerate gases. Further enhancement of sensitivity and reduction of complexity are crucial conditions for success and widening of their applications.

At the end of the thesis is presented an alternative multi-state cold-atom interferometer that is easy-to-use and fully merged with an atom chip. We do not rely on external variables i.e. on spatially separated paths, but use internal atomic states. The multi-state functionality is achieved by coherent manipulation by means of radio-frequency (RF) and static magnetic fields of BECs in different Zeeman states of the same hyperfine level. The interferometric fringes are sharpened due to the higher-harmonic phase contributions of the multiple energetically equidistant Zeeman states. The complete coherence of the atom transfer between the condensates guarantees a visibility of nearly unity. The increase in sensitivity is paid by a reduction of the interferometer sensing range and an undesirable cross-sensitivity to magnetic fields. In addition, our interferometer does not require neither high precision alignment nor high resolution imaging.

Resumen

En esta tesis se describe la creación de un condensado de Bose-Einstein (BEC) con un "**atom chip**" así como, la integración de este con un **interferómetro** a "**multi-estado**". La teoría, construcción y optimización del experimento serán descritos en detalle.

Así como un normal chip electrónico, el "atom chip" consiste en un conjunto de conductores distribuidos en un plano. Los campos magnéticos producidos por estos conductores serán usados para atrapar y manipular átomos de Rubidio. Nuestro "atom chip" fue preparado en colaboración con la Universidad de Viena, mientras que el resto de aparato experimental esta construido en el instituto LENS, Universidad de Florencia.

El condensado viene producido usando el campo magnético de un conductor en la superficie del chip, así como el interferómetro aprovecha del campo cercano producido de los conductores integrados en el chip.

El "atom chip" es cargado con átomos de ^{87}Rb enfriados hasta $\sim 100 \mu\text{K}$ en una "mirror-MOT" a unos 8 mm sobre la superficie del chip. Después de la fase de carga unos 2×10^7 átomos son atrapados en la trampa magnética $\sim 200 \mu\text{m}$ sobre la superficie del chip. Para llegar al proceso de condensación de Bose-Einstein, los átomos son posteriormente enfriados a través del "RF evaporative cooling" durante 2.5 segundos. El condensado se forma con una temperatura crítica de 500 nK, con $\sim 3 \times 10^4$ átomos.

La interferometría de ondas de materia es una herramienta útil para medir con alta precisión propiedades cuánticas de los átomos, fenómenos a multi-cuerpos y gravedad. Muchos de los interferómetros atómicos usan la excelente localización en el espacio de momentos

y la coherencia de los condensados de Bose-Einstein. El aumento de la sensibilidad y la reducción de la complejidad son elementos cruciales para el éxito de su aplicación.

Al final de la tesis se presenta un nuevo interferómetro de átomos fríos a multi-estado que es simple como construcción. El interferómetro no está basado en variables externas, es decir en una separación espacial de los caminos, sino en el uso de estados internos del átomo. Esta característica multi-estado se consigue a través de un control coherente de los subestados Zeeman del mismo nivel hiperfino de un condensado con impulsos de radiofrecuencia (RF) y un campo magnético estático. Las franjas son agudizadas gracias al alto contenido armónico que viene de las fases de los diferentes subestados Zeeman cuando son energéticamente equidistantes. La transferencia coherente y completa de las poblaciones atómicas entre los diferentes subestados nos garantiza una visibilidad de casi la unidad. El aumento de la sensibilidad tiene como contrapartida una reducción en campo del interferómetro y una no deseada sensibilidad a los campos magnéticos. En compensación nuestro interferómetro no requiere ni alineamientos ópticos de precisión ni sistemas de "imaging" de alta resolución.

A mi familia...

Acknowledgements

I'll never forget my first day at Lens Institute. At that time Lens was situated on the marvelous Arcetri hill and it consisted of no more than some prefabricated blocks, hidden in this bunker-like hill. A bit lost and very shy, I was looking for the lab where I was supposed to work. I remember someone walking the corridors and singing something from an opera: it was Prof. **Massimo Inguscio**. When he saw me, he said aloud "hola" to me, and then he asked me what I was doing there. I answered him quickly and he told me: "But don't you know we are making a condensate of Bose-Einstein, do you?" That was my beginning with atomic physics, and first of all I want to say thanks to Massimo, who pushed and helped me to work in this world of condensates.

Many people have been involved in the hard work described in this thesis. Saying a simple thanks is not enough to describe my gratitude for being there with me and for me.

Thanks to my supervisor, **Francesco Cataliotti**, for opening for me a door-way to this exciting field of microtraps, and for his support throughout the last years. And thanks to my tutor in Spain, **Jose Manuel Calleja**, for all the headaches I caused him.

Building the lab was possible only with the close and joint work with **Saverio Bartalini**, who has been my partner in carrying out all the little steps on the way in the lab, from learning the basics together, to discussing subtleties in our work. Many will testify that in building the lab together, we had a special connection between us, and I am happy we did it together.

Special thanks goes to my colleague, **Jovana Petrovich**, with whom I had the pleasure to collaborate on many of the papers we have written in this thesis.

Thanks for all the suggestions from **Chiara Fort** and **Giacomo Roati**, they resolved great part of my question with practical and successful answers, making my life much easier. They are a true source of knowledge in atomic physics, the phrase *Chiara Fort ha sempre ragione* was repeated many times in the lab.

I would like to thank the people who gave a contribution to the experiment: **Luigi Consolino**, **Antonio Mio**, **Vera Guerrera**, **Pietro Lombardi**, **Jessica Lye**, **Florian Schaefer** and **Mario Siciliani** for the hard work and great company. I feel truly lucky to have had the opportunity to work with them and have fun with such a great team.

I would like to thank the continuous support I received from the **LENS** institute in Florence, and the **university of Florence**, the **university of Catania** and the **scuola superiore di Catania**. I have had the joy of being in a group of excellent people working in very different fields, from which I have learned about more than only my own field of research. I feel enriched for having been a fellow.

In Florence the work in the lab could not have been carried out without our electronics wizards headed by the amazing **Mauro Giuntini**, **Marco de Pas**, and **Alessio Montori**, the guys at the mechanical workshop, and our wonderful administrative staff over the years, who made sure the group keeps running.

I want to remember special people from Catania who collaborated with me, in the Sicilian period, from Professor **Emanuele Rimini**, **Natale Marino**, a man for all, electronic, mechanic, politic, **Giuseppe Pappalardo**, **Giuseppe d'Arrigo**, and all the volcanic guys of the Catania mechanical workshop. And in special remembrance to professor **Giuseppe Angilella** a pillar of the Dipartimento di Fisica and the Scuola Superiore. I had the opportunity to work with him discovering a be great friend who believes in me, and thanks for the tea.

Words are just not enough to explain the ever present love and support I get from my parents, **Esther Benzaquén** and **Antonio Herrera**. You are the source of power that makes it possible for me to fulfill my wishes.

Contents

1	Introduction	1
2	Atom–Chip background theory	5
2.1	Overview	5
2.2	Laser Cooling	7
2.2.1	Slowing atoms with light	7
2.2.2	Optical Molasses	8
2.2.3	Sub–Doppler Mechanisms	9
2.2.4	Magneto–optical trap	13
2.2.5	Other Cooling Techniques, CMOT	17
2.2.6	Optical Pumping	19
2.3	Magnetic trapping and guiding on an atom chip	20
2.3.1	The interaction of an atom with a static magnetic field	20
2.3.2	Majorana spin flips	22
2.3.3	Quadrupole and Ioffe-Pritchard traps	22
2.3.4	Trapping fields from planar current distributions	25
2.3.5	Three-dimensional wire traps.	27
2.3.6	Advantages and limits of scale reduction	30
2.3.7	Simulations	34
2.4	The thermodynamics of cold atoms	35
2.4.1	The thermodynamics of cold atoms	35
2.4.2	Thermal clouds in a harmonic trap	37
2.4.3	Expansion of thermal clouds	37
2.5	Bose-Einstein condensate in a harmonic trap	38
2.5.1	Density distribution of a BEC in the Thomas Fermi limit	41
2.6	Forced evaporative cooling	43

2.6.1	A simple model for evaporative cooling.	44
2.6.1.1	Collisional properties of rubidium	47
3	Apparatus and methods	49
3.1	Overview	49
3.2	Vacuum system	50
3.2.1	Vacuum chamber	51
3.2.2	Vacuum procedure	55
3.3	Atom-Chip	58
3.3.1	Chip	58
3.3.2	Under-chip	60
3.3.3	Assembly	64
3.4	Magnetic coils suit	66
3.4.1	Coils suit	67
3.4.2	Current power supplies	70
3.5	Radio-Frequency Evaporative Cooling	75
3.6	Laser System	78
3.6.1	Overview	78
3.6.2	DFB	80
3.6.3	DFB master laser	81
3.6.4	DFB repump	90
3.6.5	Shutters	92
3.6.6	Spatial filtering	93
3.6.7	MOT optical setup	94
3.7	Extracting the Information from Atoms Clouds	94
3.7.1	Fluorescence	96
3.7.2	Absorption imaging	97
3.7.3	Optical setup	98
3.7.4	Resolution	100
3.7.5	CCD Camera	101
3.7.6	Absorption imaging procedure	101
3.7.7	Imaging Spectrum	104
3.7.8	Magnification	107
3.7.9	Image Fitting	107

3.7.10	Signal to noise ratio between absorption and fluorescence imaging	108
3.8	The remote control electronics and software	109
4	Reaching BEC	113
4.1	Overview	113
4.2	Mirror MOT	115
4.2.1	Pulsed dispenser	115
4.2.2	Mirror MOT	117
4.3	CMOT and Molasses	122
4.4	Optical Pumping	124
4.5	The magnetic trapping	127
4.6	The compressed trap	136
4.7	Evaporative Cooling step	145
4.8	BEC signatures	147
4.8.1	Anisotropic expansion	148
4.8.2	Bimodal density distribution across the phase transition	150
4.8.3	Phase space density	151
4.8.4	BEC properties	151
5	Atom chip multi-state interferometer	153
5.1	Introduction	153
5.2	The multi-state interferometer idea	154
5.3	Rabi oscillations and Ramsey spectroscopy	155
5.4	Multi-state interferometer set-up	157
5.5	Theoretical model	162
5.6	Results	164
6	Conclusions	171
7	Conclusiones	175
	References	177

1

Introduction

Ultracold neutral atoms in magnetic microtraps on a chip are a new and exciting system for quantum engineering [1, 2, 3]. Because of their electric neutrality, these atoms are very well decoupled from the environment. With the achievement of Bose-Einstein condensation (BEC) in a gas of neutral atoms [4, 5], it has become possible to prepare a large number of atoms in a well defined quantum state. In 1999, the first experiment was reported in which atoms were trapped in magnetic fields generated by microfabricated wires on a substrate [6]. Soon thereafter, these "atom chips" were used to prepare BECs, with a much simpler experimental setup and in much shorter time than in traditional experiments [7, 8]. The versatility of this technique was further demonstrated in experiments in which atoms were guided, transported, splitted and merged with the help of suitably designed microfabricated wire patterns (see [1, 2, 3] and Chapter 1 of this thesis for a review of atom chips). Inspired by the enormous success of microfabrication technology in miniaturizing, figure out the idea of a "quantum laboratory on a chip", where a large number of ultracold atoms can be manipulated on the quantum level, with the help of tiny wires, magnets, and optical elements.

BEC experiments are complicated, relying on many different techniques from a variety of areas in experimental physics. In fact, it was not until 70 years after Einstein first predicted the phenomenon of BEC in 1925, that techniques were developed to reach the extremely low temperatures necessary for the experimental realization of BEC in a dilute atomic vapor. A main objective of the present thesis, combined with the help of several other group members,

1. INTRODUCTION

was to produce the first atom chip in Italy. A comprehensive description of the details of our machine is included in this thesis, along with an evaluation of the design relative to the latest breakthroughs in BEC technology, and a prospective on future machine designs.

Coherent superpositions of quantum states, quantum interference, and entanglement are the main resources which distinguish such a quantum laboratory from its classical counterpart. The capability to manipulate these resources and to preserve the coherence of the created quantum states for a long time are thus essential prerequisites for applications of atom chips in quantum engineering. Current research in this area is aimed at creating an atom interferometer on a chip. Our group at Florence has proposed an atom chip multi-state interferometer based on the coherence between five states. This interferometer operates in the time domain. Such an interferometer can be extremely sensitive, as the constructive interference of multiple states increments the slope of the fringes. A similar trapped atom interferometer was also proposed in [9]. Another design uses multi-mode interferometry, with atoms being split and recombined as they propagate above the chip [2].

Organization of the present work

- Chapter 2: I review basic concepts of atom chips from laser cooling to the condensation process, including wire structures for magnetic trapping and properties of Bose-Einstein condensates in chip traps. In this chapter I give all the theoretical tools used to build the experiment.
- Chapter 3: I describe in detail our apparatus and some techniques used during the experiment. This chapter is fundamental to the understanding of the complexity of a BEC apparatus and the diversity of skills and knowledge (programming, engineering, design, electronics, optics, atomic physics, vacuum technology) needed to construct it.
- Chapter 4: This part is dedicated to a full description of our experimental sequence for Bose-Einstein condensation on the chip, starting with the MOT loading step and finishing with the condensation on the chip. Reporting all the problems and giving some smart solutions, it can serve as a useful guide to achieving a condensate on chip.

-
- Chapter 5: A description of our experiments on coherent internal-state manipulation of atoms in chip traps are described. Here I describe the working principle and realization of a multi-state interferometer with the sensitivity better than that of an ideal two-state interferometer, and discuss its properties and possible applications.

1. INTRODUCTION

2

Atom–Chip background theory

2.1 Overview

The physics principles involved in laser cooling and trapping, which have been well developed since the 1980s, are essential for understanding atom-chip experiments. The theoretical analysis can be found in numerous textbooks and publications [10, 11, 12]. However, most of those books and review articles are written from the experimentalist perspective or from a broad theoretical approach, and from one side hence no formal derivations are given, in theoretical texts one can not find the specific physics of my field. From my experience as a graduate student. I often find myself in darkness, not precisely understanding the physics even though. I am able to run the experiments. I attempt to clarify here some of the most important derivations step by step, while still siding on the experimentalist side.

Bose-Einstein condensation experiments are complicated, and they draw on many different techniques from a variety of areas in experimental physics to reach the extreme conditions required. In this chapter one would try to give the necessary notions about the physics of the BEC apparatus. Not on the associate condensate physics, but of the necessary techniques to arrive to the degenerate state, that are an important section of the atomic physics and they are necessary to be able to understand the apparatus.

The phenomenon of the condensation of Bose–Einstein takes place with such increase of the density in the phase space, so that the associate wave functions of the atoms overlap to arrive to quantum degeneration. Arriving to

2. ATOM-CHIP BACKGROUND THEORY

this extreme condition it has been a problem that was only resolved 50 years after the theoretical prediction. To arrive at the goal it has been necessary the development of new theories in the interaction of atom and light as well as new technologies, e. g. the laser is an indispensable element as we will see.

In principle we can think that spatial compression of a gas is the like more direct road. This way is not correct, since it takes us to a condensation in the classic sense of the word. That is to say a high space density implies a bigger probability of 3 body collisions that it would provoke the formation of molecules and later of bigger aggregates. This path tend to localize the atoms, that is to say to return them distinguishable some of other, destroying any possibility to arrive to condensation.

The followed road consists on lowering the temperature of the atoms until you reach the phase transition. Making a simplification, if we think of each atom like a wave packet whose extension is of the order of the thermal longitude of de Broglie wave associated to a particle, $\Lambda_{dB} = \sqrt{2\pi\hbar^2/(M\kappa_B T)}$, where T is the temperature and M is the mass of the atom, if we cool the atoms until Λ_{dB} , is of the order of the interatomic distance, the wave functions overlap and arrives to the quantum degeneration and, therefore to condensation. The source of atoms is a room temperature gas at vapor pressure. The first enormous gain in phase space density occurs when the vapor is transferred into a magneto-optical trap (MOT) in a UHV environment. Further **laser cooling**, either polarization gradient cooling or molasses, gains another order of magnitude in phase space density. There often follows a stage of adiabatic compression with the atoms confined in a purely **magnetic trap**. This stage does not increase the phase space density, but it does provide optimum conditions for the final evaporation stage. **Evaporative cooling** takes the gas the final six-seven orders of magnitude in phase space density to reach the conditions for **BEC**.

This chapter reviews cooling and trapping mechanisms on to an atom-chip, from **laser cooling** and then explains the fundamentals of **magnetic traps** and in particular **micro-traps**, **evaporative cooling**, to the Bose-Einstein condensation (**BEC**).

2.2 Laser Cooling

The laser cooling stages of the path to BEC allow us to capture atoms from the vapour of rubidium from our dispenser ~ 500 K and cool them to a temperature of $10 \mu\text{K}$. The addition of a confining force in the MOT allows the atoms to be trapped at densities of over 10^{17} m^{-3} . This represents an extraordinary gain in phase space density. The theory of laser cooling is extensively reviewed in [13] and [12]. This section describes the principles of cooling and trapping in a magneto-optical trap, commonly called by the acronym MOT.

2.2.1 Slowing atoms with light

The principle underlying the deflection and slowing of atoms with laser light is the conservation of momentum in the scattering process. Although the idea of radiation pressure emerges from Maxwell's equations, the most intuitive description for momentum transfer in light scattering comes from quantum mechanics. In 1917, Einstein proposed that light is quantized, with each quantum, or photon carrying energy, $E = h\omega$ and momentum $\mathbf{p} = \hbar\mathbf{k}$, where ω is the frequency and \mathbf{k} the wave-vector of the light. When an atom absorbs a photon (from a laser beam, for example), the energy goes into the internal state of the atom as the atom is promoted to an excited state. The momentum is transferred to the center of mass motion, as the conservation of momentum requires the atom to recoil in the opposite direction to the laser beam. Some time later, the excited atom will spontaneously decay to the ground state, emitting a photon and recoiling again. Spontaneous emission is a random process, with the probability of emission in any particular direction given by the symmetric dipole radiation pattern. Averaged over many absorption and emission cycles, the spontaneous emission results therefore in zero net change in the momentum of the atom. The result of shining a laser beam on an atom is therefore to change the momentum of the atom in the direction of the laser beam. The momentum carried by each photon is extremely small, but because on resonance an atom can scatter many photons the forces can be huge. With a laser beam it is easy to drive a strong atomic transition into saturation, so that the atom spends half its time in the excited state. In this case, each absorption-emission cycle takes twice the excited-state lifetime τ and transfers $\hbar\mathbf{k}$ of momentum.

2. ATOM-CHIP BACKGROUND THEORY

The maximum force on the atom is then given by

$$\mathbf{F}_{Rad.} = \frac{\Delta p}{\Delta t} = \frac{\hbar k}{2\tau_0}. \quad (2.1)$$

For the Rb D_2 line $\tau_0 = 27$ ns, and this force corresponds to a maximum acceleration of 1.1×10^5 ms⁻², or above 10^4 g.

2.2.2 Optical Molasses

To move from slowing to cooling, it is necessary to find a way of narrowing the velocity distribution of the atoms. This requires a dissipative, velocity-dependent force. Doppler cooling was first suggested in 1975 by Hänsch and Schawlow [14]. Three counter-propagating pairs of beams, one along each of the Cartesian axes, are used to illuminate the atoms from all directions. The light is red-detuned slightly from resonance. As an atom moves through the light, the Doppler shift means that it sees the light it is moving towards as closer to resonance, and the light it moves away from as further from resonance. Therefore the atom scatters more photons from the light that propagates in the opposite direction to its motion, and is slowed down, regardless of which direction it is moving in. The Doppler effect for a moving atom makes the scattering force velocity dependent, and spontaneous emission provides the dissipation.

To get a more quantitative idea of how this works as a cooling mechanism, it is useful to consider a one-dimensional model with a single pair of counter-propagating laser beams and a two-level atom, see [12]. If each beam has an intensity sI , the total force on the atom is

$$F = \hbar k \frac{\Gamma}{2} \left[\frac{s}{1 + 2s + 4(\Delta - kv)^2/\Gamma^2} - \frac{s}{1 + 2s + 4(\Delta + kv)^2/\Gamma^2} \right], \quad (2.2)$$

where $s = I/I_{sat}$, Γ is the natural linewidth, and Δ is the detuning from resonance.

For red detuning and close to $v = 0$ the force varies linearly with velocity, and we have a damping force

$$F = -\alpha v. \quad (2.3)$$

The damping coefficient is given by

$$\alpha = -4\hbar k^2 s \frac{2\Delta/\Gamma}{(4\Delta^2/\Gamma^2 + 2s + 1)^2}. \quad (2.4)$$

Equation 2.3 therefore describes motion in a viscous medium, and this cooling scheme is known as *optical molasses*.

The solution of the equation of motion 2.3 is exponential damping towards zero velocity. However, the damping force discussed above is only the average force. The absorption and spontaneous emission process is a stochastic one, and so the force has fluctuations which produce heating. This situation, with a force term and a diffusion term can be analyzed using the Fokker-Planck equation to yield the velocity distribution of the atoms, see [13]. From this it can be shown that the lowest temperature is obtained when $\Delta = \Gamma/2$ and is given by

$$T_D = \frac{\hbar\Gamma}{2\kappa_B}. \quad (2.5)$$

This is known as the Doppler temperature, and for rubidium $T_D = 144 \mu\text{K}$.

2.2.3 Sub-Doppler Mechanisms

Historically, the observation of sub-Doppler temperatures in optical molasses came as a complete surprise. The theoretical explanation was subsequently developed independently by two groups [15, 16], who showed that sub-Doppler cooling depends upon two features that were left out of the Doppler theory of optical molasses described above. The first is the multi-level nature of the atom. In practice, we do not have a two-level system, but the ground and first excited states are split into a number of sublevels. The second is the polarization of the light field. Consider a multi-level atom at rest, illuminated with light of a particular polarization. Optical pumping will occur between the ground state sublevels. This results in an equilibrium distribution of the ground state population between the sublevels that reflects the local light field. Classically, this corresponds to orientation of the atomic dipole relative to the polarization of the light field. When the atom moves through a spatially varying polarization pattern, optical pumping will redistribute the population so that the dipole follows the field. However, optical pumping between the sublevels takes a finite time, and so the orientation of the moving atom always

2. ATOM-CHIP BACKGROUND THEORY

lags behind the polarization state of the light. It is this non-adiabatic following that gives rise to the sub-Doppler cooling effects. This is known as polarization gradient cooling.

Polarization gradient cooling can be understood using simple one-dimensional models first presented in [15], and well reviewed in [13] and [12]. This treatment applies to a $\Delta J = +1$ transition (such as the $J = 1/2 \rightarrow J' = 3/2$ *trapping* transition in ^{87}Rb), with the light red-detuned from resonance as is the case in optical molasses. In one dimension, there are two basic types of polarization gradient, as shown in figure ???. In the π^x/π^y configuration the two counter-propagating beams have orthogonal linear polarizations. In this case the polarization of the light field varies from linear to circular to orthogonal linear and back again over a distance of $\lambda/2$. In the (σ^+/σ^-) configuration the laser beams have opposite circular polarizations. In this case, the polarization is linear everywhere, but the polarization vector rotates around the beam axis with a pitch of $\lambda/2$. In the complex light field of three-dimensional molasses, both are present. To show how the non-adiabatic following gives rise to cooling we consider the two cases separately.

Case π^x/π^y

The simplest atom susceptible to π^x/π^y polarization gradient cooling has a $J = 1/2$ ground state and a $J = 3/2$ excited state. As the atom moves through the light field, the AC Stark shift of each of the two ground state levels varies, as shown 2.2. Consider an atom in the $m_F = +1/2$ sublevel at the origin. As it moves from left to right, kinetic energy is converted to potential energy as it climbs a potential hill. At the top of the hill, the light is σ^+ and there is a strong probability that the atom will be optically pumped into the $m_F = -1/2$ state, and find itself at the bottom of a hill again. The potential energy is radiated away during the optical pumping process, as the spontaneous emission is at a higher frequency than the absorption, the difference being the difference in light-shift between the two states (see figure 2.2). As with Doppler cooling, it is spontaneous emission that provides the dissipation. The cooling is most effective for atoms moving with a velocity such that they travel a distance $\lambda/4$ in the optical pumping time, as shown in figure 2.2.

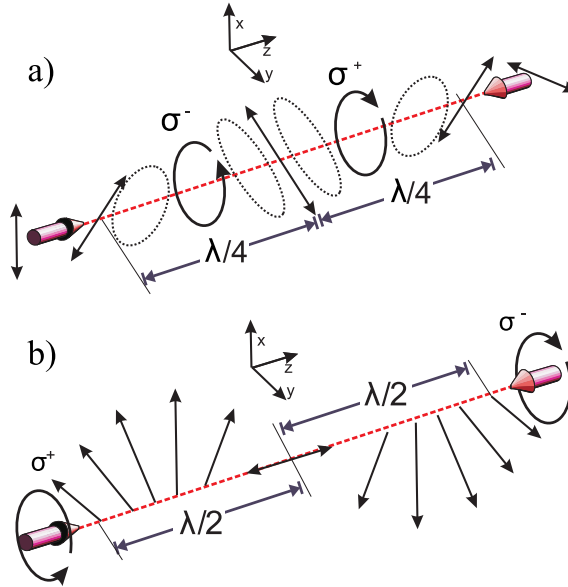


Figure 2.1: The two field configurations considered in polarization gradient cooling: (a) (π^x/π^y) . The polarization varies from linear through circular, to the opposite linear, and back again, over a distance of $\lambda/2$. b) The electric field is linearly polarized everywhere, but the direction of polarization rotates around the beam axis with a pitch of $\lambda/2$.

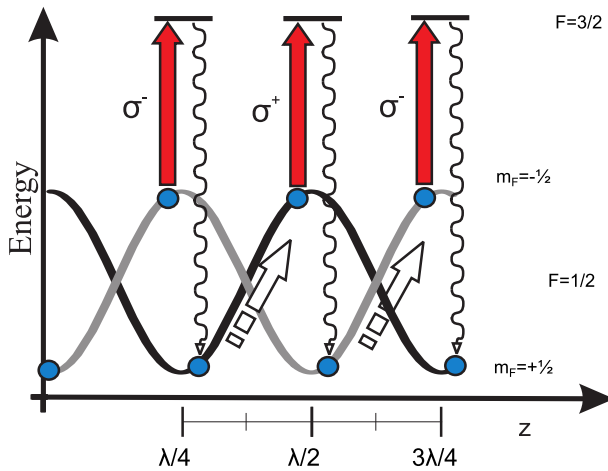


Figure 2.2: π^x/π^y polarization gradient cooling. An atom starting in the $m_F = -1/2$ state at the origin climbs a potential hill as it moves from left to right. As it reaches the top of the hill at $\lambda/4$, it is optically pumped into the other state, and starts climbing again. The kinetic energy of the atom is transferred to potential energy and radiated away during the optical pumping cycle.

2. ATOM-CHIP BACKGROUND THEORY

Case σ^+/σ^-

In the case of σ^+/σ^- counter-propagating beams, the polarization is linear everywhere, and the light-shift of each sublevel does not vary with position. The origin of the cooling in this case is more subtle. The simplest case here is a $F = 1 \rightarrow F' = 2$ transition. For such an atom at rest in a linearly polarized light field, the populations in the $m_F = \pm 1$ sublevels are equal. As the atom moves through the polarization pattern, we can consider it as a dipole trying to follow the polarization vector. As discussed above, due to the finite optical pumping time, the dipole does not follow the polarization exactly, but lags slightly behind. This lag corresponds to an unequal population of the $m_F = \pm 1$ sublevels. The cooling arises because this unequal population causes the atoms to scatter more photons from one of the beams than the other. A more detailed consideration of the theory [15] shows that for red-detuned light, the atom scatters more photons from the beam it is moving toward, and hence is slowed down.

It is important to understand that this is not the same mechanism that occurs in Doppler cooling. In polarization gradient cooling, the preferential absorption from the beam in the opposite direction to the atomic motion is driven by a population imbalance in the atomic sublevels caused by the time scale for optical pumping and the motion of the atoms. Doppler cooling, on the other hand, relies on the difference in Doppler shifts for the preferential absorption from the beam in the opposite direction to the atomic motion.

Despite of that, the resulting properties of these models are almost the same, and yield important corrections to the predictions based on the classical molasses theory. The minimum achievable temperature limit is thus lowered and, in the limit $\Delta \gg \Gamma$, has the following expression

$$T_{min} \approx \frac{\hbar\Gamma^2}{I_s\kappa_B} \frac{I}{|\Delta|}. \quad (2.6)$$

The minimum temperature is now proportional to the laser intensity, and inversely proportional to the detuning. It finally explains what experiments had revealed: for very small intensities and large detuning the temperature can be lowered well below the Doppler temperature. The physical quantity actually limiting the temperature in molasses is the photon recoil momentum

$\hbar k$. For ^{87}Rb it corresponds to a velocity $v_{rec} = 5.8$ mm/s and to an equivalent temperature $T_{rec} = 359$ nK. In normal operational conditions, the temperature achieved in molasses is of the order of a few tens of μK .

As we have seen, the force in molasses is a damping force, but there is not any confinement mechanism. The result is that atoms in molasses randomly diffuse with small velocities (as in a Brownian motion), but can escape from it. Typical lifetimes of atoms in molasses are of the order of hundreds of milliseconds. This time is not long enough to assure the accumulation of big numbers of atoms required for a normal experiment on Bose–Einstein Condensation. From here the need of a new idea that, combined with the strong cooling mechanism of the optical molasses, could assure a big source of cold atoms. The solution has been found in the Magneto–Optical Trap.

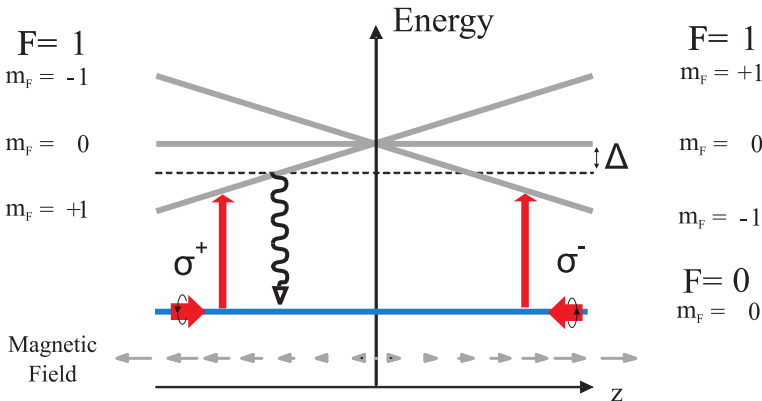


Figure 2.3: Schematic of a MOT in one dimension. The trapping transition shown is an $F = 0 \rightarrow F = 1$ cycling transition.

2.2.4 Magneto–optical trap

The preceding two sections have shown how atoms can be slowed and cooled until their temperature is only a few times the recoil limit. However, the forces involved in both Doppler and sub-Doppler cooling are dissipative, not confining. Eventually, the atoms will diffuse out of the laser beams, and be lost. What is needed is a method to trap the atoms while they are being cooled. This can be achieved by adding the magnetic field produced by a pair of anti-Helmholtz coils to the three intersecting pairs of laser beams used for

2. ATOM-CHIP BACKGROUND THEORY

optical molasses. If the laser beams have the correct polarizations, this adds a confining force to the dissipative cooling forces described above. The result is known as the magneto-optical trap [17].

To see how the confining force arises it is useful to consider a simple one dimensional model. For simplicity we consider an atom that has a $F = 0$ ground state, and a $F' = 1$ excited state. The atom is considered to be at rest, so the Doppler shift can be ignored. The magnetic field is zero at the origin, and increases linearly with z . Its direction is such that it always points away from the origin (this is the one-dimensional analogue of the three-dimensional quadrupole field produced by anti-Helmholtz coils). The atom is illuminated from either side with circularly polarized light that is red-detuned slightly from resonance. To begin with we will consider just the $+z$ side of the origin as shown in figure 2.3. It is important to note that in figure 2.3, the polarization states of the two beams are defined relative to the magnetic field direction. The diagram shows that as we move away from the origin, the Zeeman shift brings the $m_F = -1$ sublevel closer to resonance, and the $m_F = +1$ level further away. This means that $\Delta m_F = +1$ transitions to the $m_F = -1$ sublevel are favored. Hence an atom at the right of the center will scatter more photons from the σ^- polarized beam coming from the right than it will from the σ^+ beam coming from the left. This results in a force pushing it to the left, towards the origin.

Now consider an atom to the left of the center of the trap in the diagram, in the ground $m_F = 0$ state. With red detuned laser beams, the atom will be in resonance with the excited $m_F = 1$ level, and thus will probably absorb light from the σ^+ light which induces $\Delta m_F = 1$ transitions. The atoms will experience a restoring force to the center of the trap, as well as the cooling force from the Doppler shift. This treatment can be extended to any $F \rightarrow F' = F + 1$ transition, and applies along the beam axes in 3D space with the appropriate choice of beam polarizations, see figure 2.4.

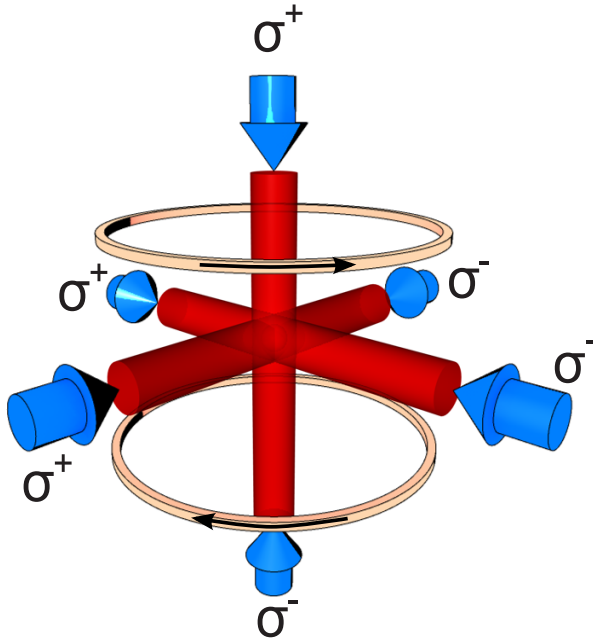


Figure 2.4: The laser beam and coil geometry for the usual 6-beam MOT with a quadrupole configuration.

The magneto-optical trap was first realized in the three-dimensional geometry shown in figure 2.4. It is obvious that the red-detuned laser beams also forms a three dimensional Doppler molasses, and so the atoms collected in the trap should be cooled to the Doppler temperature. It is less obvious whether the sub-Doppler cooling processes described above can still operate. The polarization state of the light field is complex, and the Zeeman shift due to the magnetic field will perturb the pattern of light-shifts that these cooling mechanisms depend upon. In practice, for the heavier alkalis, sub-Doppler temperatures are routinely achieved in the MOT. There is always a small region in the center of the trap where the Zeeman shift is low enough for the light shift to dominate, allowing polarization gradient cooling to take place. This means that large clouds tend to be hotter than smaller ones.

The shifting of atomic line frequencies in the presence of a magnetic field come from the Zeeman anomalous effect [18]. The restoration force can be obtained by adding a position-dependent frequency modulation into the Doppler

2. ATOM-CHIP BACKGROUND THEORY

shift in equations 2.2 in the following way

$$\Delta \rightarrow \Delta \mp kv \mp \frac{g_F m_F \mu_B}{\hbar} z, \quad (2.7)$$

where g_F is the Landé factor and μ_B is the Bohr Magneton. Then the force in equation 2.2 can be corrected to become

$$F = \pm \frac{\hbar k \Gamma}{2} \left(\frac{s}{1 + s + \frac{4}{\Gamma^2} (\Delta \mp kv \mp \frac{g_F m_F \mu_B}{\hbar} bz)^2} \right). \quad (2.8)$$

Where b is the gradient of the magnetic field along z . The net force from the two counter-propagating beams becomes

$$F = -\alpha v - \beta z, \quad (2.9)$$

where

$$\beta = \frac{g_F m_F \mu_B b}{\hbar k} \alpha. \quad (2.10)$$

The force present in a Magneto-Optical Trap is thus a confining and cooling force.

The characterizing equations for a 3-D MOT will be the same presented above, just taking into account that the beam crossing region define a limited trapping volume in which the MOT is effective. It can be approximated by a sphere of radius r , with r the radius of the beams.

The best gradient value is determined by the condition that a steady atom is in resonance at the borders of the trapping volume

$$b = \frac{\hbar |\Delta|}{g_F m_F \mu_B r} \quad (2.11)$$

From here one can find the minimum velocity an atom must have to be trapped, i.e. the capture velocity

$$v_c = \frac{\hbar k^2 r}{|\Delta|} \frac{\Gamma}{2M} \frac{s}{1+s} \quad (2.12)$$

For low intensity v_c grows linear with I (remember $s = I/I_s$), and saturates

with $I/I_s \gg 1$. The maximum value (refer to s) can take is

$$v_c^{max} = \frac{\hbar k^2 r}{|\Delta|} \quad (2.13)$$

For ^{87}Rb , with $\Delta = -3\Gamma$ and $r = 3$ mm we have $v_c^{max} = 31$ m/s. Considering that the MOT loads from a thermal gas of ^{87}Rb atoms, only one atom in a thousand has a velocity $v < v_c$.

2.2.5 Other Cooling Techniques, CMOT

Before the magnetic trapping can be used other techniques to increase the density of the cloud are needed. These methods are not based on collecting more atoms and are not useful for this purpose, they are used to avoid one of the limiting factors of the normal MOT, the radiation pressure. The duration of this technique is shorter than the normal loading MOT stage due to its poor rate to collect atoms, and is used at the end of the MOT stage.

The effect of compressing the MOT by increasing the field gradient has been studied experimentally and theoretically for spherical 6-beam MOTs [19, 20]. The central observation is that merely increasing the magnetic field gradient does not lead to significant compression of the cloud. This is due to radiation pressure. Light scattered out of the trapping laser by one atom can be reabsorbed by another, pushing the atoms apart. This can be thought of as a repulsive force between the atoms. As the density increases, the probability of rescattering increases, and this repulsive force goes up. In the regime where each photon is rescattered only once before leaving the cloud, this force has an inverse square law dependence on the distance r between the atoms [21]

$$\vec{F}_R = \frac{I\sigma_L\sigma_R}{c4\pi r^2} \hat{r}, \quad (2.14)$$

where σ_L is the cross-section for scattering light from the trapping beams, σ_R is the cross-section for absorption of the rescattered light, I is the intensity of the trapping light and c is the speed of light. The density distribution of the cloud is the result of equilibrium between this rescattering force and the trapping force.

The force due to a single rescattering discussed above (equation 2.14) is

2. ATOM-CHIP BACKGROUND THEORY

important in determining the density in the MOT, but it does not give rise to the observed incompressibility. This arises because of multiple scattering. As the density increases, the mean free path of a scattered photon will drop. As soon as there is an appreciable probability for a photon to be rescattered more than once before leaving the cloud, the rescattering force increases dramatically. This sets an upper limit on the density. The rescattering force can be reduced by decreasing the rate for scattering light out of the trapping beams, this is done by reducing the detuning or the intensity. However, this also reduces the restoring force in the MOT, and eventually this strategy reaches a limit.

Two techniques that have been used to increase the phase space density before the magnetic trapping stage are a *dark-spot MOT* or a *compressed MOT*. Both techniques are not cooling mechanism but can increase the space density of the atom cloud.

In a dark-spot MOT a shadow is placed in the centre of the repumping beam [22]. Cold atoms gather in this centre spot and fall into the dark ground state. With no resonant light present, the density is no longer limited by radiation pressure. This was a technique that was used in the earlier experiments [4, 5], but has dropped out of common usage more recently.

On the contrary in a compressed MOT one temporally changes the detuning and intensity of the MOT beams, enhancing the density of the MOT [19]. Using a compressed MOT technique it is possible to increase the MOT density while maintaining the phase space density. The follow procedure it can be diverse but the common element is an increment on the detuning, red detuning, of the cooling light and a decrease on the intensity of the cooling light. One can help the compression increasing the magnetic gradient, or the opposite way decreasing the magnetic gradient, the choice depends of the number of atoms you have in your atom cloud. Another usual trick is; during this phase sometimes decreasing of the repumper beam, this helps in the way that the atoms do not stay to much time in the resonant state ($F = 2$).

The compressed MOT stage plays important roles. The compressed MOT geometry, CMOT processes clean the shape of the atom cloud and reduce the effective volume of the trap. This helps match the cloud shape to the shape of the magnetic trap, in our case microtraps, changing from a millimetric dimension trap to the microscopic dimension. Finally, as dissipative forces are

active in the compressed MOT, the cloud can be cooled as it is compressed, which means that the phase space density can be increased. This should be contrasted with compressing the magnetic trap, where the best one can hope for is to preserve the initial phase space density by compressing adiabatically.

2.2.6 Optical Pumping

After the laser cooling stages, the atoms will be spread across the m_F states. When the atoms are transferred to the magnetic trap, only the low-field seeking states will be confined, $F = 2$, $m_F = +1$ and $m_F = +2$. To maximize the transfer of atoms into the magnetic trap, the atoms are optically pumped into the $m_F = +2$ state. A schematic of optical pumping is shown in Figure 2.5. The pumping light can either be tuned to the $F = 2 \rightarrow F' = 3$ transition shown in (a), or the $F = 2 \rightarrow F' = 2$ transition, shown in (b). In both cases σ^+ light stimulates $\Delta m_F = +1$ transitions.

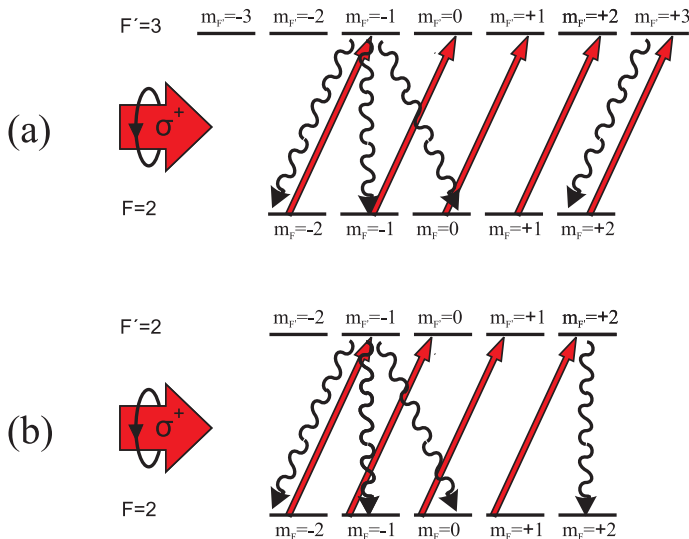


Figure 2.5: The two options for optically pumping ^{87}Rb atoms to the $F = 2$, $m_F = +2$ state.

Atoms in the presence of σ^+ light quickly climb up the magnetic states until they gather in the $m_F = +2$ state. In the case of (b), this state is effectively dark to the light, and the pumping results in minimal heating. The experimental disadvantage of using this transition is that an extra AOM is needed to frequency shift the light. We can expect to gain a factor of 2.5

which corresponds to the ratio of trapped to untrapped states assuming an even distribution across m_F states after optical cooling.

2.3 Magnetic trapping and guiding on an atom chip

Neutral atoms can be manipulated by means of their interaction with magnetic, electric, and optical fields. In this introduction the emphasis is put on the magnetic and the electric interaction. The designing of traps and guides using charged and current-carrying structures and the combination of different types of interaction to form devices for guided matter wave optics are discussed. It is shown how miniaturization of the structures leads to great versatility where a variety of potentials can be tailored at will. We start with some general statements and then focus on the concepts that are important for surface-mounted structures and address issues of miniaturization and its technological implications.

2.3.1 The interaction of an atom with a static magnetic field

We start by considering an atom in a static magnetic field B . We choose the basis where the total electronic angular momentum F and the total nuclear angular momentum I are uncoupled, $|J, m_J; I, m_I\rangle$. The hyperfine interaction Hamiltonian for an atom in the ground state is then

$$\hat{H} = A\mathbf{I} \cdot \mathbf{J} - \boldsymbol{\mu} \cdot \mathbf{B}. \quad (2.15)$$

The first term is the magnetic dipole contribution to the hyperfine interaction, and the second term the interaction with the applied magnetic field. The magnetic moment $\boldsymbol{\mu}$ is given by

$$\boldsymbol{\mu} = -(\mu_B g_J \mathbf{J} + \mu_N g_I \mathbf{I}), \quad (2.16)$$

where g_J and g_I are the electronic and nuclear Landé g-factors. This Hamiltonian 2.15 can be treated by perturbation theory in the case of weak and strong magnetic fields, but for intermediate fields it must be diagonalised exactly. The alkali metals turn out to be a rather fortunate case. As the ground state has $L = 0$ and $S = \frac{1}{2}$, the total electronic angular momentum $J = \frac{1}{2}$. This case

2.3 Magnetic trapping and guiding on an atom chip

case can be diagonalised analytically for all I , giving the Breit-Rabi formula. The result for the ground state of ^{87}Rb , which has $I = \frac{3}{2}$ is plotted in figure 2.6.

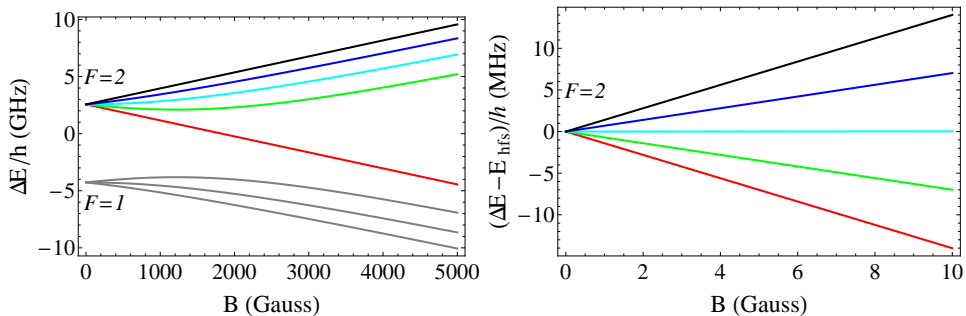


Figure 2.6: The diagrams representing the magnetic field dependence of the sublevel energies is known as a Breit-Rabi diagram, for the $5s^2S^{1/2}$ state of ^{87}Rb , E_{hfs} is the hyperfine splitting for $B = 0$. The color legend for the Zeeman states is: $m_F = 2$ (red), $m_F = 1$ (blue), $m_F = 0$ (light blue), $m_F = -1$ (green) and $m_F = -2$ (black)

This shows that at low magnetic field, the total angular momentum $F = I + J$ is a good quantum number, and we can use the basis $|F, m_F\rangle$. The Zeeman shift in this region is to a very good approximation linear with the applied magnetic field (i.e. the magnetic moment μ is independent of B), and we can write the Zeeman shift as a function of magnetic field as

$$\Delta E = \mu_B g_F m_F B, \quad (2.17)$$

where g_F is

$$g_F = g_I \frac{F(F+1) + J(J+1) - I(I+1)}{2F(F+1)} - \frac{\mu_N}{\mu_B} g_I \frac{F(F+1) - J(J+1) + I(I+1)}{2F(F+1)} \quad (2.18)$$

is useful to separate out two groups of states. States with $g_F m_F > 0$ have lower energy in low magnetic fields and so these states are called weak-field seeking. The opposite is true of states with $g_F m_F < 0$; these are called strong-field seeking. Atoms in weak-field seeking states can be trapped in a local

2. ATOM-CHIP BACKGROUND THEORY

minimum of the magnetic field. For ^{87}Rb these states are shown in table 2.1. As Maxwell's equations do not allow a maximum of the magnetic field in free space [23, 24], only weak field seekers can be trapped. The stretched state $F = 2, m_F = 2$ has the strongest interaction with the magnetic field, and will therefore be the most strongly trapped.

$ F, m_F\rangle$	$g_F m_F$
$ 2, 1\rangle$	1/2
$ 2, 2\rangle$	1/2
$ 1, -1\rangle$	1/2

Table 2.1: Trappable states

2.3.2 Majorana spin flips

A weak field seeing atom trapped in a local minimum of the magnetic field oscillates in the trap. It therefore explores a region where the magnetic field varies in both magnitude and direction. In order to ensure that the atom remains trapped, it must stay in the same magnetic sublevel as it moves through the field. In other words, the projection of the magnetic moment on the local magnetic field must remain constant. We can get an idea of what this means by considering the classical picture of a magnetic moment precessing around the magnetic field at the Larmor frequency $\omega_L = g_F m_F \mu_B B / \hbar$. The precession angle will remain constant so long as any changes we make to the magnetic field are slow compared to the Larmor frequency. The condition is violated in regions of vanishing (or very small) magnetic field strength B . In these regions, transitions between m_F levels occur, taking the atom to untrapped states. This trap loss mechanism is known as Majorana spin flips, [25, 26].

2.3.3 Quadrupole and Ioffe-Pritchard traps

The magnetic traps used in our experiments can be divided into two categories: Quadrupole traps and Ioffe-Pritchard traps.

Quadrupole trap

The first magnetic trap [27] has been realized with a magnetic quadrupole field. It is realized by a pair of Anti-Helmholtz coils, with axis along z and at a position of $z = \pm A$. The radius is R and the current I flows in opposite direction; the field vanishes along the axis of the coils for $z = 0$, and in the proximity of this point it changes linearly. The field around the minimum is of the form

$$\mathbf{B} = B'_x x \mathbf{e}_x + B'_y y \mathbf{e}_y + B'_z z \mathbf{e}_z, \quad (2.19)$$

with the additional requirement on the field gradients $\nabla \cdot \mathbf{B} = 0$ and $\nabla \times \mathbf{B} = 0$ to satisfy Maxwell's equations. Here we have chosen the cartesian coordinate vectors \mathbf{e}_i along the main axes of the quadrupole. The trapping potential given by equations 2.17 and 2.19 is proportional to $B(r) = \sqrt{(B'_x x)^2 + (B'_y y)^2 + (B'_z z)^2}$ and thus provides linear confinement.

For atoms in a quadrupole field, whatever velocity the atom will have, there may be a trajectory passing sufficiently close to the field zero point that the atom will experience an arbitrarily fast change in magnetic field direction. The spin will thus flip from its original state to the opposite one, making the weak-field seeker atom to become a strong-field seeker and to escape from the magnetic trap.

In all experiment involving for the first time a quadrupole trap [10, 27], trap losses due to Majorana transitions near the zero of the magnetic field were encountered. For atoms moving at a velocity v , and the effective size of this *hole* in the trap is $\sqrt{2\hbar v / \pi g_F \mu_B M_F B'}$, which is about $3\mu\text{m}$ for $v = 1\text{m/s}$ and $B' = 100\text{ Gauss/cm}$. As long as the hole is small compared to the diameter of the cloud the loss effect causes only a slow decay of the trapped atoms number (even longer than a minute). As the temperature drops, however, the size of the hole shrinks with the thermal velocity of the atoms, but the diameter of the atom cloud shrinks even faster, leading to a T^{-2} dependence of the loss rate [5, 28]. Quadrupole traps are nevertheless useful for ensembles of relatively hot atoms which spend most of their time far away from the *hole* in the trap center where Majorana losses occur [29]. Furthermore, quadrupole fields are used for magneto-optical traps.

Ioffe-Pritchard trap

A much simpler solution to the problem of Majorana spin-flips was soon found by changing the static magnetic field geometry: the Ioffe-Pritchard trap, first proposed for plasma confinement by *M. Ioffe* [30], and reconverted to cold atoms by *D. Pritchard* [31]. Its evolutions, as the *cloverleaf trap* [32] and the *QUIC trap* [33, 34] are now the most used magnetic traps in cold atoms experiments. The start point of a Ioffe-Pritchard trap is the same quadrupole field but, by adding some more current loops, the zero of the field at the trap center can be eliminated. The trap profile is not yet linear but quadratic, and the trap approximates a harmonic confining potential. A full analysis of the field geometry in the Ioffe-Pritchard trap, in comparison with the quadrupole trap, is done in Ref.[35]. The simplest configuration of IP trap, the QUIC trap, consists in adding a third coil with axis perpendicular to the axis of the quadrupole coils pair.

The Ioffe-Pritchard trap, IP trap, provides quadratic confinement and has a finite magnetic field in the trap center. In the simplest, axially symmetric case, the trapping field is of the form

$$\mathbf{B} = B_{IP} \begin{pmatrix} 1 \\ 0 \\ 0 \end{pmatrix} + B' \begin{pmatrix} 0 \\ -y \\ z \end{pmatrix} + \frac{B''}{2} \begin{pmatrix} x^2 + (y^2 + z^2)/2 \\ -xy \\ -xz \end{pmatrix} \quad (2.20)$$

It arises from the combination of a two-dimensional quadrupole field in the yz -plane with gradient B' and a *bottle-field* with constant term B_{IP} and curvature B'' along x . The magnetic field modulus expanded to second order in the displacement from the trap center has the form

$$B(r) \approx B_{IP} + \frac{B''}{2} x^2 + \frac{1}{2} \left(\frac{B'^2}{B_{IP}} - \frac{B''}{2} \right) (y^2 + z^2). \quad (2.21)$$

This leads to harmonic confinement of atoms of mass m and magnetic

moment $\mu = \mu_B g_F m_F$ with trap frequencies

$$\begin{aligned}\omega_{axial} &= \sqrt{\frac{\mu}{m} B''} \\ \omega_{radial} &= \sqrt{\frac{\mu}{m} \left(\frac{B'^2}{B_{IP}} - \frac{B''}{2} \right)},\end{aligned}\tag{2.22}$$

in the axial ω_{axial} and radial ω_{radial} direction, respectively. Equation 2.22 shows that the trap aspect ratio $\omega_{axial}/\omega_{radial}$ of an ideal Ioffe trap can be tuned from prolate (cigar-shaped) to isotropic and further to oblate (pancake-shaped), depending on the value of B'' compared to B'^2/B_{IP} , as experimentally demonstrated e.g. in [36]. In general, a Ioffe-Pritchard trap need not be axially symmetric, and the field in the trap center may be tilted with respect to the principal axes of the harmonic potential.

The Majorana loss rate in a Ioffe-Pritchard trap has been calculated for $F = 1$ in [37]. For $\omega_{axial} \ll \omega_{radial}$, it is

$$\gamma_M = 4\pi\omega_{radial} \exp(-2\omega_L/\omega_{radial}).\tag{2.23}$$

2.3.4 Trapping fields from planar current distributions

The basic principles of microscopic magnetic traps can be illustrated by looking at the magnetic field created by an infinitely long straight wire, carrying a current, superposed by a homogeneous bias field, see figure 2.7. When a magnetic potential is created by a system of wires with characteristic size r and carrying a current I , the trapping field gradient and curvature respectively scale as I/r^2 and I/r^3 when r is decreased [38]. Therefore, traps that replace the customary field coils by thin wires can provide very tightly confining potentials with much less power dissipation than *traditional* traps using macroscopic coils. Consequently, much stronger traps become realizable with this technique. This section shows how trapping fields are constructed from the fields of coplanar wires, and discusses some simple configuration.

2. ATOM-CHIP BACKGROUND THEORY

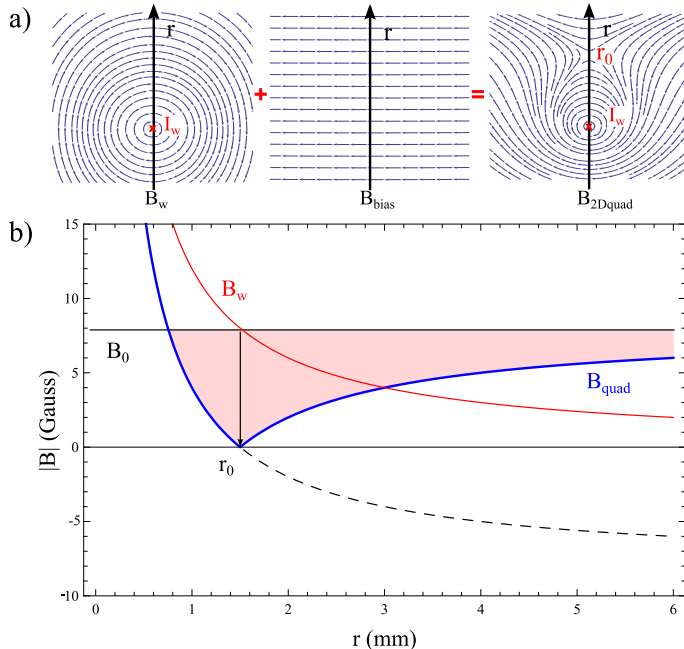


Figure 2.7: (a) Combining the radial field of a straight wire with a homogeneous bias field, a two-dimensional quadrupole field forms in the plane perpendicular to the wire. (b) Magnetic field of the simple wire trap. Red line correspond to the field from the wire and the black line to the bias field B_0 (remember the sign of the field is negative).

The magnetic field modulus, gradient, and curvature at a distance r from an infinitely thin wire carrying a current I are

$$B_w(r) = \frac{\mu_0 I}{2\pi r}, \quad (2.24)$$

$$B'_w(r) = -\frac{\mu_0 I}{2\pi r^2}, \quad (2.25)$$

$$B''_w(r) = \frac{\mu_0 I}{4\pi r^3}, \quad (2.26)$$

Here μ_0 is the vacuum permeability. For a complete overview of cold-atom physics in microtraps see [1] and [2].

Obviously, to achieve strongly confining traps, it is advantageous to locate the trap center as close as possible to the wire, and this was one of the main motivations for constructing traps with microscopic wires. The wire field alone does not provide trapping because it does not possess a minimum, but there are

2.3 Magnetic trapping and guiding on an atom chip

many ways to construct trapping potentials either with multiple wires or with a combination of wire fields and uniform external fields. The strong confinement in these traps results from the large values of the wire field gradient 2.25 and curvature 2.26. A particularly simple and versatile configuration results when a uniform external field B_0 is added perpendicular to the wire axis: a line of zero field forms at a distance r_0 from the wire axis, see figure 2.7,

$$r_0 = \frac{\mu_0}{2\pi} \frac{I}{B_0}. \quad (2.27)$$

On the transverse axis passing through this line of zero field, the wire and external field have the same direction, so that the external field does not affect the field gradient. The transverse field gradient of the total field at r_0 is therefore

$$B'(r_0) = \frac{2\pi}{\mu_0} \frac{B_0^2}{I} \quad (2.28)$$

Thus, the superposition of the wire and external fields creates a two-dimensional quadrupole trap, or atom guide, with a transverse restoring force proportional to $B'(r_0)$. Arrangements of several parallel wires, either with or without external fields, can also be used to create such guides.

At the minimum of such a quadrupole wire guide the field is zero and atoms can be lost due to Majorana transitions. This can be prevented by adding a longitudinal field (B_{IP}) parallel to the wire (effectively rotating the bias field). The trap minimum is then harmonic and it can be characterized by its curvature (equation 2.29) and trap frequency (equation 2.30).

$$\left. \frac{d^2 B}{dr^2} \right|_{r_0} = \left(\frac{2\pi}{\mu_0} \right)^2 \frac{B_0^4}{B_{IP} I^2} = \frac{B_0^2}{B_{IP} r_0^2} \quad (2.29)$$

$$\frac{\omega}{2\pi} = \frac{1}{2\pi} \sqrt{\frac{\mu_B g_F m_F}{M} \left. \frac{d^2 B}{dr^2} \right|_{r_0}} \sim \frac{B_0^2}{r_0} \sqrt{\frac{1}{M B_{IP}}} \quad (2.30)$$

2.3.5 Three-dimensional wire traps.

An easy way to build traps is to start from the guides discussed above, and close the trapping potential with *endcaps*. This can be accomplished by taking advantage of the fact that the magnetic field is a vector field, and the interaction potential is scalar 2.15. By varying the angle between the wire and the

2. ATOM-CHIP BACKGROUND THEORY

bias field, one can change the minimum of the potential and close the trap. Simple geometries are either a straight guide and an inhomogeneous bias field, or a homogeneous bias field in combination with a bent wire.

Three-dimensional traps can be created with a single wire by bending the wire ends at right angles to form a U or Z . In both cases, the central part of the wire in combination with the bias field forms a two-dimensional quadrupole for transverse confinement, while the bent wire parts provide the axial confinement. The trapping potential is qualitatively different for the case of a U and a Z .

Z-trap

In the case of a Z , the components B_x^b point in the same direction, adding up to a finite field along x in the trap center, see figure 2.8 for geometry. The result is a three-dimensional Ioffe-Pritchard trap with trap center located at $x = 0$, $y = 0$, and $z \approx z_0$. The axial confinement is provided by the curvature $\partial^2 B / \partial^2 x$. Since in this configuration B_z^b vanishes at $x = 0$, the trap center is unshifted, however, the trap axis is tilted.

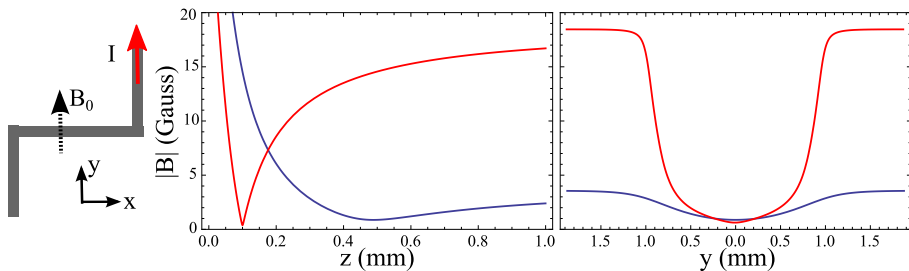


Figure 2.8: Wire layout for a IP, and calculated magnetic fields generated for $I = 1$ A. The bias field along y was set to have the trap at positions; $r_0 = 0.5$ mm (red line) and 0.1 mm (blue line). The fields shown in the figure were obtained by numerical Biot-Savart-type calculations, taking into account a wire width of $125 \mu\text{m}$

The Z-wire trap is harmonic near its minimum, yet it has a strong confinement by a nearly linear gradient further away from the wire (see equation 2.25), allowing efficient evaporative cooling. Additional compression can be achieved by reducing the offset field by adding an external bias field B_{IP} against the direction of the intrinsic offset field.

U-trap

In the case of a U , the field components B_x^b generated by the two bent wires point in opposite directions and cancel at $x = 0$, see figure 2.9 for geometry. The resulting potential is that of a three-dimensional quadrupole trap, with field zero at $x = 0$, $y > 0$, and $z \approx z_0$. The trap is shifted along y due to the field components B_z^b of the bent wires.

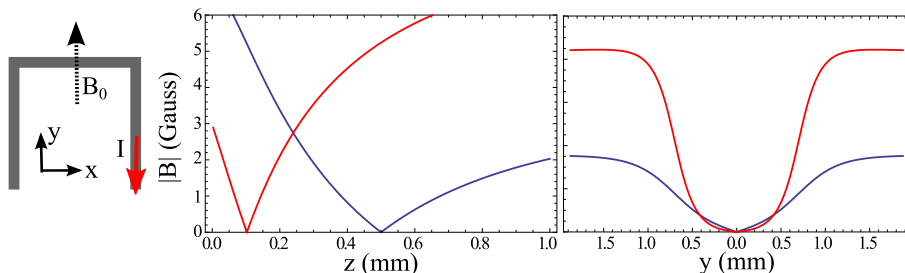


Figure 2.9: Wire layout for a quadrupole, and calculated magnetic fields generated for $I = 1$ A. The bias field along y was set to have the trap at positions; $r_0 = 0.5$ mm (red line) and 0.1 mm (blue line). The potentials shown in the figure were obtained by numerical Biot-Savart-type calculations, taking into account a wire width of $125 \mu\text{m}$

With the correct bias field, the magnetic field produced by the current flowing into a U conductor can approximate a quadrupole configuration around the zero field point, and thus can substitute the standard quadrupole coils pair for the MOT [39]. other great point is that the quadrupole can be *tilted* to get a 45° respect to the surface defined by the planar structure, this feature permits a mirror-MOT configuration for the loading of the chip. Critical parameters are the orientation with respect to the 45° directions and the volume of the region in which the orientation keeps almost constant. See figure ??.

Other traps

The experiments described in this thesis use this basic z -shape potential to manipulate BECs and cold thermal clouds. Numerous experiments have demonstrated more complex wire traps and guides [2]. For example, the bias-field can be generated by wires mounted on the atom chip [40], multi-wire

2. ATOM-CHIP BACKGROUND THEORY

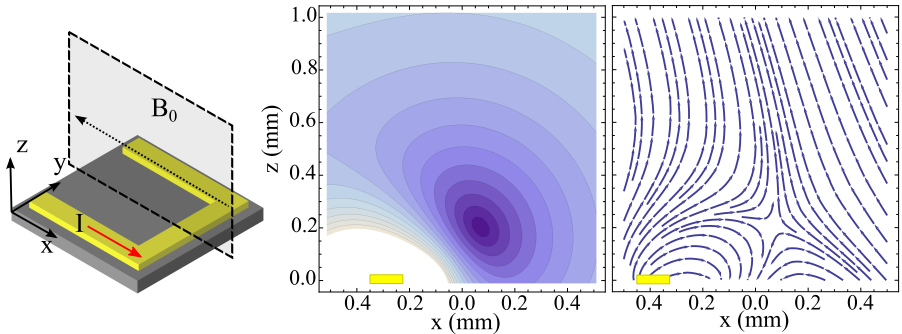


Figure 2.10: Density plot and vector plot of the magnetic potential of a U-shaped structure. The field lines plotted in the left graph show that in proximity of the guide center the field geometry approximates that of a quadrupole field with axis tilted by 45° .

guides [41] and beam splitters [42] have been realized, and conveyor belts [8, 43] have been used to transport thermal atomic clouds and BECs. Two crossing conductors form the basis of the systematic approach given in [1]. Such a conductor crossing, used with an appropriate external field, constitutes a particularly simple Ioffe–Pritchard trap.

2.3.6 Advantages and limits of scale reduction

On-chip micro-conductors can generate confining potentials with exquisite properties. These include traps with extremely strong confinement and correspondingly small ground-state size, strongly anisotropic traps with extreme aspect ratio. The high degree of control over the atomic position in a chip trap may enable surface studies of a new kind.

So part of the motivation for chip traps comes from the exceptionally strong confinement which they provide, and it is interesting to consider how tight the magnetic confinement can be made. To obtain the strongest possible trap with a given wire, the trap center must be located as close as possible to the wire surface or current has to be increase to it maximum. Field gradients are strongest at the wire surface; the thinner the wire, the higher the maximum gradient for a given current. Thus, it might seem at fist that the structure-size limit of available microfabrication techniques. At the same time a practical limit on the current density, smaller wires limits the maximum current.

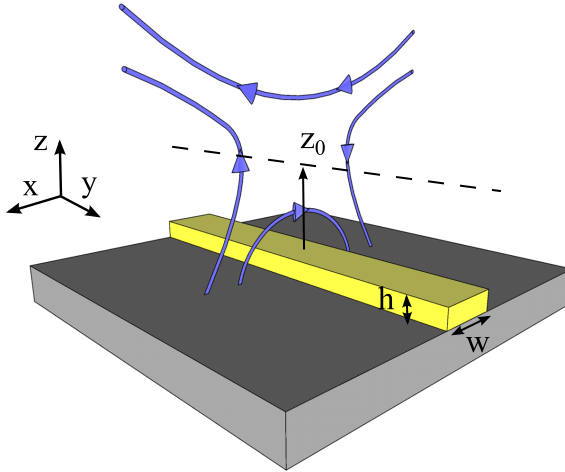


Figure 2.11: . Waveguide for neutral atoms formed at a distance z_0 from a lithographically fabricated wire of finite width w on a chip.

The oscillation frequency and the ground-state extension

The oscillation frequency along the x_i axis of a harmonic potential V is given by

$$\omega = \sqrt{\frac{1}{m} \frac{d^2 V}{dx_i^2}} = \sqrt{\frac{\mu_m}{m} \frac{d^2 B}{dx_i^2}} \quad (2.31)$$

The ground-state extension ($1/e$ radius of $|\Psi|^2$) is given by

$$\delta x_i = \sqrt{\frac{\hbar}{m\omega_i}} = \left(\frac{m\mu_m}{h^2} \frac{d^2 B}{dx_i^2} \right)^{-1/4} \quad (2.32)$$

For example, the gradient produced at a distance $r=100 \mu\text{m}$ by a wire with current $I = 1 \text{ A}$ for ^{87}Rb atoms in the $|F = 2, m_F = 2\rangle$ ground state we get frequencies of the order of 38 kHz and ground-state extension of 54 nm. To get this results a standard IP trap needed a current of the order of 10^4 amps!.

Effects of finite wire width

Till now we consider a cylindrical wire, in this case the field outside the conductor is identical to that of a infinitely thin conductor. This is not valid especially for microfabricated wires, since they typically have a rectangular

2. ATOM-CHIP BACKGROUND THEORY

cross section with an aspect ratio smaller than one ($h \ll w$) see figure 2.11. In this situation, wire height can be neglected, but not wire width. An analytical expression exists for the field generated by an infinitely long wire with width w , along the vertical [1]

$$B_{ww}(z) = -\frac{\mu_0}{\pi} \frac{I}{w} \left(\frac{\pi}{2} - \arctan \frac{2z}{w} \right). \quad (2.33)$$

For $z \lesssim w$, the formula simplifies to

$$B_{ww}(z) \simeq -\frac{\mu_0}{\pi} \frac{I}{w} \left(\frac{\pi}{2} - \frac{2z}{w} \right), \quad (2.34)$$

and it can be used to estimate the finite value of $B(z)$ at the wire surface

$$B_{ww}(0) = -\frac{\mu_0}{\pi} \frac{I}{w}. \quad (2.35)$$

This is exactly the field generated by a ideal wire placed at a distance $z = w/2$, and constitutes an upper limit on both maximum field gradient. By deriving Eq.2.33 we have

$$|B'_{ww}(z)| = \frac{\mu_0}{2\pi} \frac{|I|}{z^2 + (w/2)^2}. \quad (2.36)$$

Instead of the $1/r^2$ dependence of the thin-wire gradient, the broad-wire gradient is of Lorentzian form. The gradient at the surface is

$$|B'_{ww}(0)| = \frac{\mu_0}{\pi} \frac{|I|}{w^2}. \quad (2.37)$$

this is a limit to the microtrap compression, but other limitations due to the trap-surface distance, which result from interactions of the trapped atoms with the surface arise below few micrometer distances.

Surface Effects

Also the material properties of the trap surface set significant limits. Loss and heating mechanisms have been predicted to be relevant for distances below a few micrometer [44]. Temporal fluctuations of the charge density inside the conductor at room temperature generate a time dependent magnetic field

which induces atomic spin flips. The relative orientation between the magnetic moment and the local magnetic field is inverted and the potential well transforms into a potential hill. Consequently, the atoms are radially expelled from the wave guide. These losses have been studied in three recent experiments [45, 46, 47] with the result, that the atomic life time is reduced to below one second if the atoms approach the surface closer than approximately 4 micrometer. The loss being induced by Johnson-noise can significantly be reduced if the conductor is cooled down below the Debye temperature, i.e. to the temperature of liquid Helium. If a metallic conductor operated below the critical temperature for superconductivity, a gap in the excitation spectrum of electrons appears and thermal fluctuations are reduced exponentially. Using superconductors, even resistive heating could be avoided. Eventually, van-der-Waals and Casimir-Polder potentials will limit the nearest trap-surface distance to a few hundred nanometers [47]. Near the surface these attractive potentials increase with the sixths and fourth power, respectively, such that the quadratic power law of the magnetic wave guide potential is not strong enough to prevent the atoms from falling onto the surface.

An experimental surprise was found when a fragmentation of atomic clouds was observed already at trap-surface distances on the order of hundred micrometers, [48, 49, 50]. In [51] shows that the potential is of magnetic origin and that it depends on the sign of the current in the conductor. These findings can be explained by assuming a locally varying magnetic field component which is oriented parallel to the conductor. In a careful study, [52], the spatial fragmentation of the atomic cloud was mapped to the thickness fluctuations of the conductor and a clear relation between those has been found. Due to the thickness fluctuations, the mean current averaged over the cross-section of the conductor deviates from a straight line which results in a radial current component responsible for the unwanted axial magnetic field. In some case this fragmentation of the potential helps, in [48] the potential dimples that fragment a thermal cloud are sufficiently deep to trap a condensate.

Power limit

All the limits above mentioned are refers to the distance from the cloud to a surface, important when ones want to manipulate the atoms with on-chip

2. ATOM-CHIP BACKGROUND THEORY

device, but a more practical limit comes from the maximum current that we can run on to the wires. The maximum current is important because sets a limit on the trap depth and oscillation frequency of the magnetic trap, see section 4.6. In microelectronics, conventional current-carrying wires are known to fail due to electromigration, which is the thermally assisted motion of ions under the influence of an electric field.

The maximum viable current was measured in various experiments: For short ($\sim 1 \mu\text{m}$) gold *nanowires* of 20 nm height and widths between 60 and 850 nm on silicon substrates, a maximum current density of typically 10^{12} A/m^2 has been measured, which was essentially independent of the wire width [53]. In the context of chip traps, the maximum current density has been measured by several groups [54, 55]. Although the results scatter considerably, and depend on parameters such as substrate thickness and thermal coupling to the environment, a current density of between 10^{10} and 10^{11} A/m^2 for a wire cross section of $\sim 100 \mu\text{m}^2$, seems to be an upper limit for micron-sized gold conductors at room temperature, and can be increased by roughly an order of magnitude at liquid-nitrogen temperature [54]. Interestingly, superconductors do not offer higher current densities [38].

The high values of j given above are only reached for relatively thin ($w \sim 100 \mu\text{m}$) wires on a substrate. Indeed, in a macroscopic gold wire, with a quadratic $0.5 \times 0.5 \text{ mm}^2$ cross section for example, the current density of 10^{11} A/m^2 corresponds to a current of $25 \times 10^3 \text{ A}$.

In [55] it has been shown that wires with smaller cross-section can tolerate higher current densities. This reveals that miniaturizing the current carrying structures not only offers higher spatial resolution for structuring the magnetic potential but also provides higher trap gradients.

2.3.7 Simulations

For the modeling of the magnetic field we used the Mathematica software (Wolfram©) with the Radia add-on that was written at the European Synchrotron Radiation Facility in Grenoble. Radia is a fast multi-platform software dedicated to 3D magnetostatics computation. It is optimized for the design of undulators and wigglers made with permanent magnets, coils and linear/nonlinear soft magnetic materials. The method used in Radia belongs

to the category of boundary Integral Methods and differs strongly from the Finite Element Methods (FEM). The core part of Radia is written in object-oriented C++. The application is interfaced to Mathematica via MathLink. Pre and post processing of the field data is done in the Mathematica Language. 1D and 2D field Plots are performed using the Graphics facilities built in Mathematica. Geometries can be exported into 3D Mathematica objects for display and rendering in the Mathematica Front-End.

In cases where the approximation of constant current density inside the conductors is not valid, e.g. in the conductors of complex shape, the current density is determined by solving the Laplace equation for the electrostatic potential inside the conductor, using the finite elements methods provided by COMSOL©. The current density is subsequently extracted on a grid, the Biot-Savart calculation is done by Radia.

The simulations also include gravity. To analyze the potential, various functions have been written which find potential minima, trace minima along given directions, find trap frequencies, or isopotential surfaces. The visualization is based on the plotting routines of Mathematica.

2.4 The thermodynamics of cold atoms

This section briefly considers the thermodynamics of a gas of cold atoms far from quantum degeneracy. We begin by justifying the use of Maxwell-Boltzmann statistics to describe laser-cooled and magnetically trapped atoms. This distribution is then used to derive the density distribution of atoms in the magnetic trap. The expansion of a thermal cloud after release from the magnetic trap is also discussed.

2.4.1 The thermodynamics of cold atoms

In the precedent discussion laser cooling were discussed in terms of a temperature. The underlying assumption in both cases is that the velocity distribution of the atoms is described by a Maxwell-Boltzmann distribution. Each compo-

2. ATOM-CHIP BACKGROUND THEORY

ment of the velocity v_j follows a Gaussian distribution

$$P(v_j) = \frac{1}{\bar{v}_j \sqrt{2\pi}} e^{-v_j^2/\bar{v}_j^2}, \quad (2.38)$$

where $\bar{v}_j = \sqrt{\langle v_j^2 \rangle}$. The temperature T is defined by its relation to the mean square velocity

$$T = \frac{m\bar{v}_j^2}{\kappa_B}. \quad (2.39)$$

The Maxwell-Boltzmann distribution is usually derived by considering a classical gas of non-interacting particles in thermal equilibrium with a heat bath at temperature T . This is quite different from the case of laser cooled or magnetically trapped atoms, where the atoms are isolated from their room temperature surroundings.

In the magneto-optical trap, the atoms interact strongly with the light field, which certainly cannot be described as a heat bath with a well-defined temperature. The justification for the use of the Maxwell-Boltzmann distribution in this case follows from a consideration of the forces acting on the atoms [12]. The force can be described in terms of two components: an average force arising from the radiation pressure of the light beams, and a fluctuating force due to spontaneous emission. The statistical mechanics of this situation are described by the Fokker-Planck equation. If the average force is proportional to the velocity (i.e. a damping force), and the fluctuations are independent of velocity (which is the case for spontaneous emission), then the steady state solution of the Fokker-Planck equation is the Maxwell-Boltzmann distribution. It is therefore reasonable to define a temperature according to the equation 2.39, even though the concept of thermal equilibrium does not apply.

In the magnetic trap, the atoms are completely isolated from the environment. In this case, the concept of a temperature only applies in the presence of collisions, which allow the system to reach an equilibrium state. The temperature of the ensemble is again defined using equation 2.39. As the collision rate in the magnetic trap can be very low, the system can take several seconds to reach equilibrium, and non-equilibrium states can easily be produced. This is the case during the compression of the magnetic trap, as discussed in Section 4.6.

2.4.2 Thermal clouds in a harmonic trap

For a particle in a one-dimensional harmonic potential, the time averaged kinetic and potential energies are equal, i.e

$$\frac{1}{2}m\langle v_j(t) \rangle^2 = \frac{1}{2}m\omega^2\langle x_j(t) \rangle^2. \quad (2.40)$$

This means that the Gaussian Maxwell-Boltzmann velocity distribution of the atoms in a thermal cloud gives rise to a Gaussian spatial distribution,

$$n_{th}(x, y, z) = n_0 e^{\left(-\frac{x^2}{2\sigma_x^2} - \frac{y^2}{2\sigma_y^2} - \frac{z^2}{2\sigma_z^2}\right)}, \quad (2.41)$$

where the peak density n_0 is

$$n_0(x, y, z) = \frac{N}{(2\pi)^{3/2}\sigma_x\sigma_y\sigma_z}. \quad (2.42)$$

The rms width σ_j in each direction is given by

$$\sigma_j = \sqrt{\frac{\kappa_B T}{m\omega_j^2}} \quad (2.43)$$

2.4.3 Expansion of thermal clouds

The rms velocity of the atoms in each direction can be expressed in terms of the cloud size and the trap frequencies by combining equations 2.39 and 2.43

$$\bar{v}_j = \sqrt{\frac{\kappa_B T}{m}} = \sigma_j \omega_j. \quad (2.44)$$

If the thermal cloud is suddenly released from the trap, its initial velocity distribution is *frozen in*. This means that after an expansion time t its size in each direction becomes

$$\sigma_j(t) = \sqrt{\sigma_j^2(0) + \bar{v}_j^2 t^2}. \quad (2.45)$$

It is also useful to write the above results in a different way. Equation ?? can also be written as

$$\sigma_j^2(t) = \sigma_j^2(0) + \frac{\kappa_B T}{m} t^2. \quad (2.46)$$

2. ATOM-CHIP BACKGROUND THEORY

Thus the temperature of a thermal cloud can be measured by allowing it to expand and measuring its width as a function of time. This applies to the cloud released from the MOT as well as from the magnetic trap.

2.5 Bose-Einstein condensate in a harmonic trap

Bose-Einstein condensation is a macroscopic occupation of the ground state of the system as the temperature is lowered below a critical temperature T_c . The statistical mechanics for the case of a uniform gas of non-interacting bosons is most easily treated in the grand-canonical ensemble. This is a text book problem and yields simple results for thermodynamic quantities such as the critical temperature and the fraction of atoms in the ground state. In this section I will discuss the extension of this treatment to the case of non-interacting bosons in a harmonic external potential [56, 57]

In a 3D homogeneous gas of bosons the average occupation number N_i of states with energy ε_j obeys Bose statistics.

$$N_i = \frac{1}{e^{\beta(\varepsilon_i - \mu)} - 1} = \frac{ze^{\beta\varepsilon_i}}{1 - ze^{\beta\varepsilon_i}}, \quad (2.47)$$

where $\beta = 1/\kappa_B T$. The fugacity z and the chemical potential μ are related by $z = e^{\beta\mu}$. The total atom number N is found by summing over all quantum states i .

$$N = \sum_i^{\infty} N_i. \quad (2.48)$$

This sum diverges for $z \rightarrow 1$ because the term $N_0 = z/(1 - z)$ diverges in the thermodynamic limit (we take $\varepsilon = 0$ from here on). Splitting off the diverging term N_0 replacing the rest of the sum by an integral (one state per phase space element $\Delta\mathbf{r}\Delta\mathbf{p} = h^3$) the equation of state for N atoms occupying a volume V becomes

$$\frac{N}{V} = \frac{4\pi}{h^3} \int_0^{\infty} \frac{1}{z^{-1}e^{\beta p^2/2m} - 1} + \frac{1}{V} \frac{z}{1 - z} \quad (2.49)$$

This can be written in the form [58]

$$n(z, T) = \frac{N_0}{V} + \frac{1}{\Lambda^3} g_{3/2}(z), \quad (2.50)$$

where $n = N/V$ is the particle density,

$$\Lambda = \sqrt{2\pi\hbar^2/m\kappa_B T} \quad (2.51)$$

is the thermal de Broglie wavelength and $g_{3/2}$ is the Bose or Polylog function defined by

$$g_\alpha = \sum_{i=1}^{\infty} \frac{z^i}{i^\alpha}. \quad (2.52)$$

For the ground-state particle density we have

$$\frac{N_0}{V} = n_0 = \frac{1}{V} \frac{z}{1-z}, \quad (2.53)$$

and for the density in the excited states

$$n_e = \frac{1}{\Lambda^3} g_{3/2}(z). \quad (2.54)$$

Note that $g_{3/2}$ is finite for $z \rightarrow 1$ ($g_{3/2}(1) = 2.612\dots$), and thus n_e is limited, $n_e \leq g_{3/2}(1)/\Lambda^3$. At a given density, for low enough temperature, μ tends to zero from below and we have $z \rightarrow 1$; the Bose gas is saturated. All extra particles added at constant temperature will be accommodated in the ground state. The ground state becomes macroscopically occupied giving rise to the phenomenon of Bose-Einstein condensation.

A phase space density can be defined as the number of particles occupying a volume equal to the de Broglie wavelength cubed

$$\Phi = n\Lambda^3. \quad (2.55)$$

It follows from the above definition that when the phase space density is of the order of one and greater, then the de Broglie wavelengths of the individual bosons have significant overlap. The indistinguishability of the particles becomes significant, and the full Bose-Einstein distribution must be used. It is indeed in this regime that condensation occurs, as from the above

2. ATOM-CHIP BACKGROUND THEORY

equations the transition to BEC begins at a phase space density of

$$\Phi = g_{3/2}(1) = 2.612... \quad (2.56)$$

We can calculate the critical density and temperature in specific case of our potential. Our traps can be approximated to a harmonic oscillator, in this case the potential takes the form

$$U(\mathbf{r}) = \frac{1}{2} \sum_{j=x,y,z} m\omega_j^2 r_j^2. \quad (2.57)$$

And the energy of the i_{th} state is given in terms of the quantum numbers of the energy levels n_x, n_y, n_z by

$$\varepsilon_i = (n_x + \frac{1}{2})\hbar\omega_x + (n_y + \frac{1}{2})\hbar\omega_y + (n_z + \frac{1}{2})\hbar\omega_z. \quad (2.58)$$

We are interested in the occupation number of the ground state N_0 . From equation 2.57 it follows that this will become large when the chemical potential approaches the energy of the lowest state

$$\mu \rightarrow \frac{1}{2}(\omega_x + \omega_y + \omega_z). \quad (2.59)$$

The total number of atoms N can be written as the sum of the number of atoms in the ground state N_0 and the number of atoms in all the excited states, $\sum_{i \neq 0} N_i$ Taking the limit 2.59, this gives

$$N = N_0 + \sum_{n_x, n_y, n_z \neq} \frac{1}{\exp[\beta\hbar(n_x\omega_x + n_y\omega_y + n_z\omega_z)] - 1}. \quad (2.60)$$

As before to obtain N_0 in terms of N , we must evaluate the sum. By making a *semiclassical* approximation, this sum can be replaced by an integral. This requires two assumptions. The first is that the available energy is large compared to the spacing of the harmonic oscillator energy levels. This means that instead of summing over the discrete energy levels, we can integrate over a smooth density of states $\rho(\varepsilon)$. The second assumption is that we can take the thermodynamic limit $N \rightarrow \infty$, which sets the upper bound on the integral.

Equation 2.60 becomes

$$N = N_0 + \int_0^\infty \frac{\rho(\varepsilon)d\varepsilon}{e^{\beta\varepsilon} - 1}. \quad (2.61)$$

The density of states for the harmonic oscillator potential is

$$\rho(\varepsilon) = \frac{1}{2} \frac{\varepsilon^2}{(\hbar\bar{\omega})^3}, \quad (2.62)$$

where $\bar{\omega}$ is the geometric mean trapping frequency $\bar{\omega} = (\omega_x\omega_y\omega_z)^{1/3}$. On integrating, we obtain

$$\frac{N_0}{N} = 1 - \frac{\zeta(3)}{N} \left(\frac{\kappa_B T}{\hbar\bar{\omega}} \right)^3, \quad (2.63)$$

where $\zeta(n)$ is the Riemann Zeta-function. This can be written as

$$\frac{N_0}{N} = 1 - \left(\frac{T}{T_C} \right)^3, \quad (2.64)$$

where T_C the critical temperature for Bose-Einstein condensation is defined by

$$T_C = \frac{\hbar\bar{\omega}}{\kappa_B} \left(\frac{N}{\zeta(3)} \right)^{1/3} = 0.94 \frac{\hbar\bar{\omega}}{\kappa_B} N^{1/3}. \quad (2.65)$$

The results obtained above are a very good approximation, both to more detailed theoretical results and to experimental data [59]. The main weakness of this treatment is the semiclassical approximation; and the taking of the limit $N \rightarrow \infty$ in particular. It is also approximate in a different sense, as we have completely neglected interatomic interactions. The rigorous treatment of the statistical mechanics of a finite number of trapped, interacting bosons is complicated theoretical problem (see [57] and references therein).

2.5.1 Density distribution of a BEC in the Thomas Fermi limit

An interacting condensate in equilibrium at zero temperature can be described by the time independent Gross-Pitaevskii (GP) equation [60].

$$\left(\frac{-\hbar^2}{2m} \nabla^2 + U(\mathbf{r}) + g|\psi(\mathbf{r})|^2 \right) \psi(\mathbf{r}) = \mu\psi(\mathbf{r}) \quad (2.66)$$

2. ATOM-CHIP BACKGROUND THEORY

At zero temperature, all the bosons are in the ground state, described by the wave function $\psi(\mathbf{r})$. The first term in the GP equation corresponds to the kinetic energy, the second term corresponds to the potential due to the external trapping potential, and the third term is an interaction term due to the mean field produced by the other bosons. In the s-wave scattering limit, the mean field interaction can be described by

$$g = \frac{4\pi\hbar^2 a}{m}, \quad (2.67)$$

where a is the scattering length of the atom.

The GP equation can be simplified in the limit of strong interactions, when $\hbar\omega \ll gn(\mathbf{r})_{BEC}$. In this limit, the kinetic energy term in the GP equation can be neglected. This is known as the Thomas-Fermi approximation. With this approximation, it is trivial to find the density of the condensate from the GP equation

$$n(\mathbf{r})_{TF} = \frac{\mu - U(\mathbf{r})}{g}. \quad (2.68)$$

This description is only valid when the external trapping potential is equal to or less than the chemical potential. In a harmonic trap, the density has a parabolic profile when the distance in the x , y or z direction is $\leq \sqrt{\frac{2\mu}{m(\omega_{x,y,z})^2}}$, and is zero elsewhere. The chemical potential is found by normalizing the integral of the density over all space to the total number of atoms. To perform the integral, each spatial coordinate is scaled as $X, Y, Z \sqrt{\frac{2\mu}{m(\omega_{x,y,z})^2}} = x, y, z$, and the integration is over the space bounded by $R = X^2 + Y^2 + Z^2 \leq 1$. Converting to spherical coordinates, the total number of atoms is

$$N = \int_0^\pi \int_0^{2\pi} \int_0^1 \frac{\mu}{2g} \left(\frac{2\mu}{m\bar{\omega}^2} \right)^{3/2} (1-R)\sqrt{R} \sin(\theta) dR d\theta d\phi, \quad (2.69)$$

thus,

$$N = \frac{2(\mu)^{5/2}}{15a\sqrt{m\hbar^2\bar{\omega}^3}}. \quad (2.70)$$

2.6 Forced evaporative cooling

Magneto-optical traps work extremely well. However, as discussed in section 2.2.2, the temperature that can be achieved is limited by the recoil momentum. The density is also limited by radiation pressure inside the cloud. Taken together, these limits combine to set a limit of $\sim 10^{-5}$ on the phase space density that can be achieved five orders of magnitude away from the BEC transition.

The only technique that has been developed so far to cross the gap is evaporative cooling. Evaporative cooling is a well-known and widely observed phenomenon. For a system of particles with a finite binding energy, such as molecules at the surface of a liquid, or in our case, atoms in a magnetic trap that has a finite depth, the hottest particles are the most likely to escape. When they leave, they take away more than their share of the energy. After the remaining energy has been redistributed, the average energy of the remaining particles decreases, and the system cools.

In these experiments, evaporative cooling is implemented in the magnetic trap, using forced RF evaporation. The hottest atoms are coupled out of the trap in an energy-selective way by using RF radiation to drive transitions between the magnetic sublevels. The transition rate is only significant when the atoms are in resonance, which occurs when the Zeeman splitting of the magnetic sublevels is equal to the RF frequency

$$g_f \mu_B B = \hbar \omega_{RF}. \quad (2.71)$$

The atoms are driven into untrapped spin states and lost from the trap. Only atoms with sufficiently high energy can climb the trapping potential to a point where they are Zeeman-shifted into resonance. In three dimensions, this resonance condition forms a three-dimensional *evaporation surface* around the atoms.

For this to be a cooling process rather than simply a loss rate, the energy must be redistributed amongst the atoms that remain. In the magnetic trap, the energy is redistributed by elastic collisions between the atoms. To continue the cooling, the trap depth is reduced continuously by ramping down the frequency of the RF radiation. As the atoms cool down, they occupy a smaller and smaller volume at the bottom of the trap. Hence, if the cooling is working

2. ATOM-CHIP BACKGROUND THEORY

well, the density increases, even though atoms are being lost. As the atom cloud is getting both colder and denser, its phase space density increases.

2.6.1 A simple model for evaporative cooling.

The theory of evaporative cooling is an interesting application of classical kinetic theory. A detailed treatment can be found in [61]. I will use a simpler model that treats the evaporation process as a series of steps [5]. Each step starts with N atoms in the trap at a temperature T . The RF cut then removes all the atoms with an energy greater than $\eta\kappa_B T$ from the trap, where η is known as the truncation parameter. The atoms are then allowed to rethermalize, and at the end of each step, new values for N and T are calculated.

The equilibrium energy distribution of the atoms in the trap is given by the Boltzmann distribution (see section 2.4), which can be written as

$$P(\varepsilon) = A\rho(\varepsilon)e^{-\varepsilon}, \quad (2.72)$$

where $\varepsilon = E/\kappa_B T$, $\rho(\varepsilon)$ is the density of states, and A is a normalization constant.

Here I will treat the case of a 3D harmonic trap where $\rho(\varepsilon) \propto \varepsilon^2$; the theory can also be applied to other power-law potentials.

After truncation, the most energetic atoms are lost and the energy distribution is well approximated by a truncated Boltzmann distribution [61], i.e.

$$u(x) = \begin{cases} A\rho(\varepsilon)e^{-\varepsilon} & \varepsilon \leq \eta \\ 0 & \varepsilon > \eta. \end{cases} \quad (2.73)$$

After the rethermalisation time τ_{th} , the truncated distribution rethermalises. The fraction of atoms lost by the truncation at is

$$\frac{\Delta N}{N} = \frac{\int_{\infty}^{\eta} \rho(\varepsilon)d\varepsilon}{\int_0^{\eta} \rho(\varepsilon)d\varepsilon} = \frac{\Gamma(3, \eta)}{2!}, \quad (2.74)$$

where $\Gamma(n, x) = \int_x^{\infty} t^{n-1}e^{-t}dt$ is the incomplete gamma function, and $\Gamma(n) \equiv \Gamma(n, 0)$.

This allows us to write down a rate equation for the number of atoms.

$$\frac{\dot{N}(t)}{N} = -\frac{\Gamma(3, \eta)}{2!} \frac{1}{\tau_{th}} - \frac{1}{\tau_{loss}}. \quad (2.75)$$

Where τ_{th} is the rethermalization and τ_{loss} the lifetime of the magnetic trap, its includes the effect of undesirable losses from the trap, that are not due to the truncation process. It includes the effect of collisions with background gas, as well as losses due to inelastic collisions in the trap. Here, this loss rate is assumed to be constant; this assumption is justified in section 2.6.1.1.

The precedent equation shows the essential feature of evaporative cooling; it is an exponential process. By considering the energy lost from the cloud, a similar rate equation for the energy of the trapped cloud can be derived

$$\frac{\dot{E}(t)}{E} = -\frac{\Gamma(4, \eta)}{3!} \frac{1}{\tau_{th}} - \frac{1}{\tau_{loss}}. \quad (2.76)$$

To make progress, it is necessary to look at what determines the characteristic time for rethermalization τ_{th} . Energy is redistributed within the cloud by elastic collisions. The rethermalization rate is therefore the rate of elastic collisions divided by the mean number of collisions per atom needed for rethermalization to take place, which I will take to be four, following the theoretical estimate in [62]. The elastic collision rate γ_{el} is given by

$$\gamma_{el} = n_0 \sigma_{el} \bar{v} \sqrt{2}, \quad (2.77)$$

where n_0 is the peak density, σ_{el} is the cross-section for elastic collisions (see section 2.6.1.1) and \bar{v} is the average relative velocity between two atoms. Using the results in section 2.6.1.1 for a thermal cloud at equilibrium in a harmonic potential, the elastic collision rate can be written in terms of the geometric mean trap frequency $\bar{\omega}$, the number of atoms N and the temperature T

$$\gamma_{el}(t) = \sigma_{el} \bar{\omega}^3 \frac{\sqrt{6} m}{(2\pi)^{3/2} \kappa_B} \frac{N(t)}{T(t)}. \quad (2.78)$$

The rate of change of the elastic collision rate $\dot{\sigma}_{el}(t)$ during evaporation is of critical importance. By combining equations 2.75 and 2.76 and writing

2. ATOM-CHIP BACKGROUND THEORY

$\tau_{th} = 4/\sigma_{el}$, a rate equation for the collision rate can be derived

$$\frac{\dot{\gamma}_{el}(t)}{\gamma_{el}(t)} = -\frac{\gamma_{el}(t)}{4} \left(\Gamma(3, \eta) - \frac{\Gamma(4, \eta)}{3!} + \frac{4}{\gamma_{el}(t)\tau_{loss}} \right). \quad (2.79)$$

If $\dot{\gamma}_{el}(t) < 0$, the collision rate decays rapidly with time, the renormalization time $\tau_{th} = 4/\dot{\gamma}_{el} \rightarrow \infty$ and the evaporation process grinds to a halt. In contrast, exponential growth of the collision rate (i.e. $\dot{\gamma}_{el}(t) > 0$) allows a faster than exponential growth in the phase space density. This is known as *runaway evaporation*.

Equation 2.79 sets the requirements on the initial conditions for the evaporation. In order to have runaway evaporation and a sustainable increase in the phase space density, we must have $\dot{\gamma}_{el}(0) > 0$. The threshold for runaway evaporation as a function of η and $\gamma_{el}\tau_{loss}$ is shown in figure 2.12 This shows that to cool effectively and reach BEC we must have

$$\gamma_{el}\tau_{loss} \geq 150 \quad \text{at } t = 0 \quad (\text{at the beginning of the process}). \quad (2.80)$$

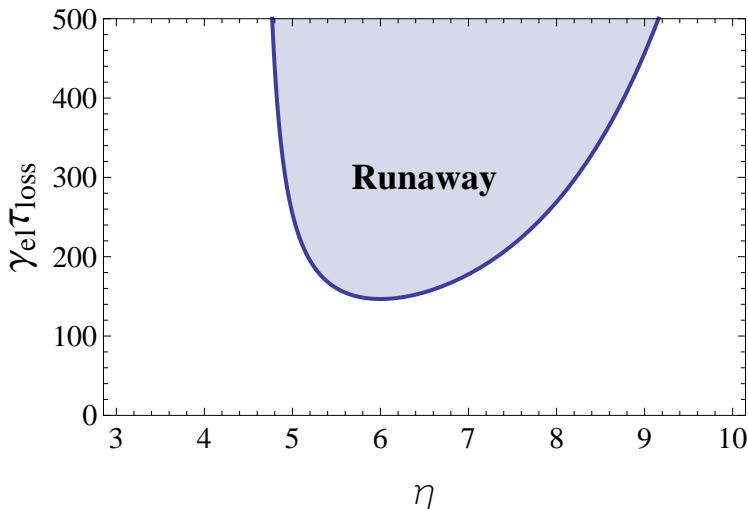


Figure 2.12: Threshold for runaway evaporation. The solid line shows the threshold $\dot{\gamma}_{el}(t) = 0$ as a function of the truncation parameter η and the product $\gamma_{el}\tau_{loss}$. Runaway can only occur if $\dot{\gamma}_{el}(t) > 0$, i.e. in the region shown

2.6.1.1 Collisional properties of rubidium

To see exactly what this condition means in terms of the experimental parameters, the collisional properties of rubidium must be considered. The collisional properties of rubidium are examined in detail in [63]. They show that in the temperature range 0 to 1 mK, the elastic cross-section for two body collisions in the $|2, 2\rangle$ state of ^{87}Rb is roughly constant at $\sim 10^{-11} \text{ cm}^2$. At low temperatures ($< 30 \mu\text{K}$) the scattering is dominated by the s-wave contribution and the elastic cross-section can be written in terms of the s-wave scattering length a

$$\sigma_{el} = 8\pi^2 a^2. \quad (2.81)$$

The s-wave scattering length is determined in [64] to be $(+98.7 \pm 2.5)a_0$ where a_0 is the Bohr radius. The positive value for the scattering length means that the interactions are repulsive.

The cross-section for inelastic processes is important in determining τ_{loss} . From the same paper, the inelastic rate constant for collisions between ^{87}Rb atoms in the $|2, 2\rangle$ state is $2 \times 10^{-16} \text{ cm}^3 \text{ s}^{-1}$. Typically, the decay rate due to collisions with background gas is $\sim 0.1 \text{ s}^{-1}$, and so inelastic collisions are not important until the density reaches $\sim 5 \times 10^{-14} \text{ cm}^3$. In our trap, densities close to this size are only reached in the condensate itself. Background gas collisions dominate during the evaporation, and the assumption made above of a constant τ_{loss} during the evaporation is justified.

2. ATOM-CHIP BACKGROUND THEORY

3

Apparatus and methods

3.1 Overview

The experimental requirements for BEC were discussed in section 2. To recap, we need a laser system that produces light for cooling, imaging and optical pumping, a very good vacuum and a tight, stable magnetic trap. This chapter describes in detail the apparatus that was constructed to meet these requirements. Details of general experimental techniques such as imaging and laser locking are also presented.

The business end of the experiment is shown in figure 3.1. The vacuum chamber containing the atom chip is at the center of the picture. The vacuum system is described in Section 3.2 and the atom chip in Section 3.3. In the photograph they are obscured by coils that generate various magnetic fields used in the experiment. For example, the magnetic trap is formed from the fields produced by the wires on the atom chip plus the bias coils. Production and control of the magnetic fields by the external coils is the subject of section 3.4. Also shown in figure 3.1 are the paths of some of the laser beams as they enter the vacuum chamber. A new laser system was designed and constructed as part of the work for this thesis, hence it is described in detail in Section 3.6. This is followed by Section 3.7 which describes the imaging system and the analysis of absorption images.



Figure 3.1: A photograph of the heart of the experiment.

3.2 Vacuum system

Experiments with ultracold atoms require an UHV, ultrahigh-vacuum, chamber to isolate the atoms from the environment. The magnetic trap lifetime is ultimately limited by collisions of the trapped atoms with atoms from the residual gas. Already the first atom chip BEC experiments [7, 8] showed that the tight confinement provided by magnetic chip traps reduces the cycle time of a BEC experiment from about one minute in standard non-chip setups to a few seconds in chip setup. To achieve trap lifetimes of the same order of the cycle times, atom chip experiments could use a single-chamber vacuum system with a background pressure in the 10^{-10} mbar range. I will divide the description of the system into two parts, one for vacuum chamber in itself and the other part for description of vacuum procedure 3.2.2. The vacuum wiring and assembly will be described together with the atom-chip system in section 3.3.

3.2.1 Vacuum chamber

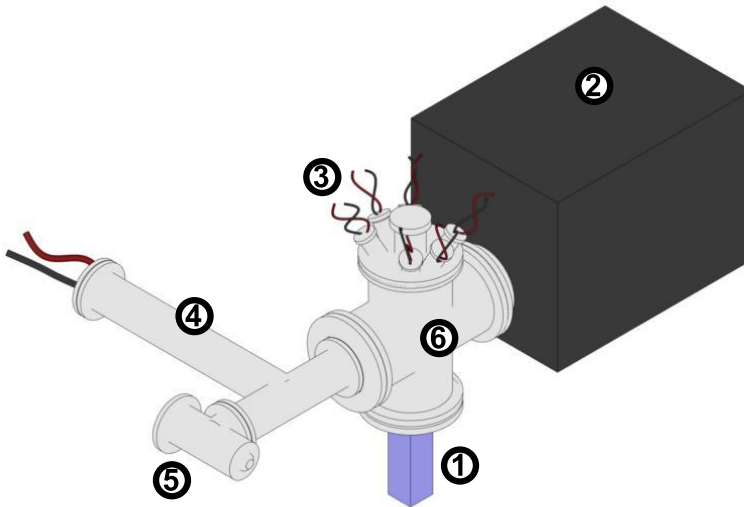


Figure 3.2: The vacuum chamber is composed of these elements: (1) Science cell (2) ionic pump. (3) electrical feedthroughs, (4) Ti-sublimation pump, (5) UHV valve, (6) four cross way.

Our vacuum setup is shown in figure 3.2. Like most of the atom chip experiments it consists of a pumping system, electrical feedthroughs and a transparent cell, the science cell, where the atom chip is and where the experiment is performed.

A four-way cross from Caburn (CX4-100), with DN100CF flanges in each way is the central part of the chamber used to connect the parts of the system. The cross is placed vertically with respect to the optical table, with the pumping system connected to both sides.

The pumping system is composed of one Ion pump and a Ti-sublimation pump. The Ion pump is a Varian VacIon Plus StarCell 150 model (125 l/s), designed for an ultimate pressure of 10^{-11} mbar and controlled by a Varian Dual controller. The current monitor output signal gives information on the actual pressure value inside of the cell. Joined with the ion pump, the Varian filament type TSP provides a very effective pumping of getterable gases and Rb vapour in the UHV regime. It is controlled by a Varian TSP controller and it can be arbitrarily switched on and off during the experiment.

An important consideration in Ti-sublimation pump placement is where the

3. APPARATUS AND METHODS

titanium will deposit. The Ti-sublimation pump's filaments should be placed so that there is not a direct line of sight to any valve or pump. The titanium will coat any surfaces with a direct line of sight to the filaments, and this can cause a valve sealing or pumping problem. See figure 3.2 for positioning of the filaments in our system.

A UHV valve is used to connect with a turbo-molecular pump during the pre-pumping stages before the UHV. The valve seals after this stage is finish.

All the system is suspended by the ionic pump, a solid structure (not shown) attached by bolts to the ionic pump, the pump is clamped to the optical table, the rest of the system is supported by the attachment to the flange of the pump. The structure was designed to have the chip surface 18 cm above the optical table.

At the top of the four way cross a cluster Caburn flange (MAF600-6-133), with six angled clearance hole mini flanges, DN16CF, equally spaced around a DN40CF port, see figure 3.3. From this cluster all the electrical connections were wired, to do this 6 electrical feedtroughs were used. The central port allows a feedtroughs with any connection, from it a rod of steel of 420 cm gives the support to the chip holder. One of the mini flange was used for a thermocouple feedtrough (262-TNC-1-C16), to connect a in vacuum N-type thermocouple to monitor the temperature of the chip. Two ports were used with a low current 10-pin feedtroughs (264-010-MO3K-10-C16). These connections were used for chip wires, dispenser and heaters. The last three ports were used with high currents 2-pin feedtroughs (264-030CU5K-2-C16), to send the currents to the Z wire, and the two copper U's. In the section 3.3 I will do a more accurately description of the in-vacuum wiring and the elements of the the atom-chip. All the feedtroughs were purchased to Allectra.

Finally at the bottom part of the four way cross the cell is attached. The science chamber, figure 3.4, is a rectangular parallelepiped glass cell (Hellma) made of Vycor, and it has inner edges lengths of 40×40 mm and 100 mm for the length. It is anti-reflection coated for 780 nm on the outside, see figure 3.4. The cell is positioned with the longer part vertical, and the top face was substituted with a glass-to-metal adapter. This adapter is home made, the design is complex it is not necessary to get into in details. It is basically composed by glass flange attach to the cell, special O-ring, and a home made steel flange. How to press the flanges to get the UHV isolation without any

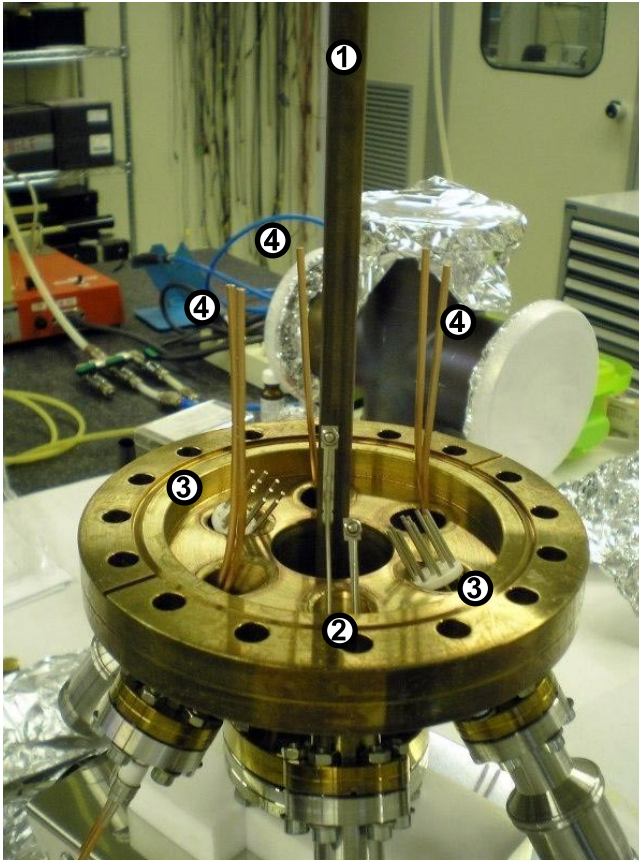


Figure 3.3: The multiport cluster with the feedthroughs inserted before the wiring. The central multiport (1) is used only to support the chip, (2) this feedthrough is for the vacuum termocouple, (3) two multi-pin feedthroughs for low currents < 10 , (4) three bipolar feedthroughs for low high currents > 10 A.

damages to the glass was the main problem, to do this the usual copper O-ring of UHV had to be substituted. In a first attempt a ring of Indium was used, the leaking problems persisted and the baking temperature was limited. It was replaced by a special O-ring, HELICOFLEX, purchased from Garlock, with which excellent results were obtained.

Trough this flange the atom-chip, the electrical wires to connect it and the dispenser atom sources enter, see figure 3.4. The chip is situated in the middle of the cell, with the gold side facing down, so that the lower part of the cell is free for laser beams. The upper part of the cell is occupied by the chip package, electrical connections and dispensers.

3. APPARATUS AND METHODS

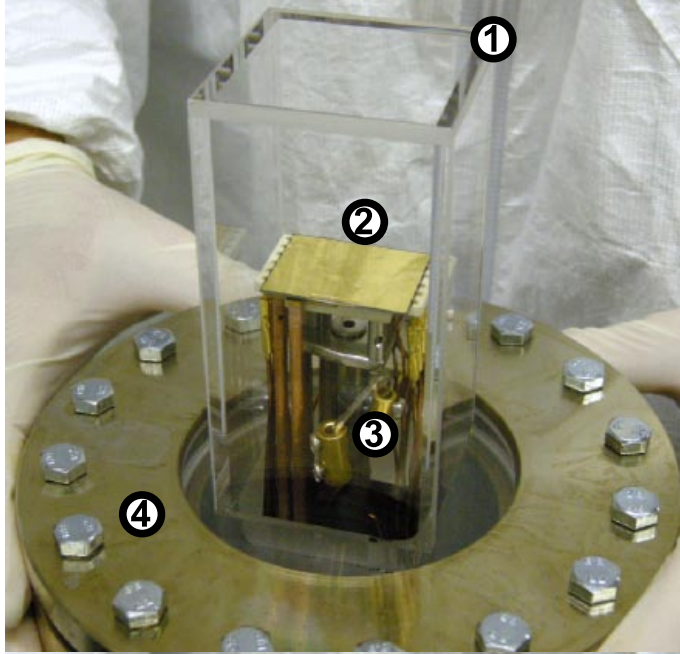


Figure 3.4: The science cell with the atom-chip and dispenser source inside. (1) Hellma glass cell, (2) chip, (3) dispenser atom source, another one is placed symmetrical behind the chip (4) home made flange for the glass metal adapter.

Two Rb dispensers are placed behind the chip, see figure 3.4, each one at the longer side of the chip. The dispenser are placed behind the chip and angled respect with the chip surface for two reasons: first, not to expose the gold surface of the chip directly to the dispenser, since rubidium and gold have good affinity; second, not to hit the walls of the cell before reaching the MOT cooling region. From the dispenser the atoms are very hot if we compare with the lab temperature, we can lower the temperature if the atoms hits the wall a couple of times before they arrive to the trapping region. Using the same flange to enter the chip and pump the vacuum is not the best configuration. The pumping speed is reduced due to the small area of cell free side (16 cm^2), compared with the DN100CF flange (157 cm^2 area), that allows for the maximum pumping speed of the ionic pump. Moreover, the chip with a surface of 6 cm^2 reduce subsequently the effective pumping area. However the pumping volume is really small and most of the outgassing surfaces are directly connected to the ionic pump with a DN100CF flange.

3.2.2 Vacuum procedure

Obtaining UHV pressures requires careful assembly of the vacuum components. The most important thing is to make sure that all components are clean. We start the cleaning process by placing the submersible parts (no valves, pumps, or cells) in an ultrasonic cleaner with strong soap for 1 hour. If the valves are cleaned in the ultrasonic cleaner they must be re-greased before they are used. The long cleaning time allows the strong soap to remove residual oil from the factory. Typically, when a stainless steel vacuum part is baked in air it will become a golden color, which we assume is residual burnt factory oil. A one hour bath in a strong basic soap will remove this coating, and it will not return with subsequent air bakes. The long bath is not absolutely necessary and may be reduced to a few minutes to just remove any particles from the parts. After the ultrasonic bath the parts are rinsed first with deionized water, then acetone, and finally spectroscopic-grade methanol. Next, the parts are baked in air for 4 hours at 400 °C to drive off any residual solvents. Once the parts have cooled they are wrapped in oil-free aluminum foil until assembly.

It is important to avoid contamination of the vacuum system during assembly. We always wear powder-free latex gloves and change them often. All copper gaskets are wiped with ultra-pure methanol before installation to remove any factory residue.

After the entire vacuum system has been assembled it is pumped out and checked for leaks. We use a small turbo pump backed by a dry, diaphragm pump to initially pump out the system. We use a diaphragm pump rather than a standard oil-filled roughing pump, because the diaphragm pump does not contain any oil, which could backflow into the system. Once the turbo pump has spun up to full speed we spray a small amount of spectroscopic-grade methanol on all the flanges and cells. If there is a large leak, the pressure in the tubing connecting the turbo pump to the diaphragm pump, read by a thermocouple gauge, will change when methanol is applied. The system is pumped on overnight before the bake out is started. A carefully cleaned, leak-free system should pump out overnight with the pressure reaching around several 10^{-9} mbar, read from the ion pump current. We turn on the ion pump briefly to determine the pressure in the system. The ion pump will not be turned on to pump for extended periods of time until the bake is underway.

3. APPARATUS AND METHODS

The vacuum system must be baked at high temperatures under vacuum to remove contaminants to obtain UHV pressures. We bake most of the vacuum system at 300 °C for several days. Before the bake-out, we run about 6 A through each getter for 30 seconds to verify the presence of Rb, which can be seen by either laser absorption or fluorescence. The high current also degasses the getters. We mount the system loosely to the optical table such that, when the system expands, there is minimal stress on the system's joints. The thermal expansion may cause enough torque to cause the flanges to leak.

The system can now be prepared for the bake. The first step in the bake out process is to wrap the glass cells with clean aluminum cloth. The cloth will protect the cells from anything that may melt onto the cells during the bake. Next we place thermocouples on the vacuum system at critical places such as the cells, glass-to-metal seals, and pumps. We then wrap the system with resistive heater tape. The aim in wrapping the heater tape is not to cover the entire surface of the vacuum system with tape, but rather to have a constant tape-to-chamber surface area ratio. Heater tape is applied to different objects proportional to their surface area and not the mass of the object. The mass only defines the time constant for thermal equilibration, whereas the ultimate temperature is determined by the heat flow in and out of the region, which is proportional to the surface area. The tape should never overlap with itself, or the intense heat will cause the tape to burn. Several short tapes are used to wrap the system so each section may be controlled independently. We do however bake the entire ion pump. The maximum temperature that we can use during bake-out is limited by the glue used in the assembly of the chip to about 125 °C . After the tapes are in place, the system is wrapped loosely with strips of fiberglass tape and then aluminium foil to provide thermal insulation.

The system is slowly brought up to the final temperature over 6 to 8 hours. The ion pump is off during the warm up. There is a large amount of material driven off the walls of the vacuum system during the initial several hours of the bake. We prefer to have the turbo pump remove the bulk of the material rather than the finite-lifetime ion pump. Each heater tape is powered by a variable AC transformer (Variac) to adjust the temperature of the corresponding section of the system. Generally we increase the temperature by at most 50 °C per hour. Temperature gradients can apply significant stress to the system. We prefer to keep the temperature gradients to under 30 °C across the glass cells

and glass-to-metal seals, which are the components most susceptible to failure. Caution must be taken as the system approaches its final bake temperature because some parts of the system could overshoot in temperature due to long thermal time constants.

Once the system is at the desired temperature we bake with just the turbo pump on for 12 hours. At this point we degas the getters and Ti-sublimation filaments. To degas the getters, we increase the current in each getter for 30 seconds to 5 A to drive off any surface contaminants. After the degassing we turn on the ion pump and valve off the still-running turbo pump. When the valve is above room temperature we close it only finger tight. Therefore, we do not allow the turbo pump to spin down until the system is back to room temperature and the valve has been properly closed with a torque wrench. We allow the system to bake with the ion pump on until the pressure on the ion pump reads in the low 10^{-9} mbar . We cool the system down slowly over 4 to 6 hours. At this point the ion pump should read the lowest possible pressure, which is 10^{-11} mbar for most pumps, if there is no leakage current. In our experiment, including a separate ion gauge in the system is more likely to do harm than good. The ultimate test of the vacuum pressure will be the lifetime of the atoms in a magnetic trap. A snapshot of making the vacuum is show in picture 3.5.

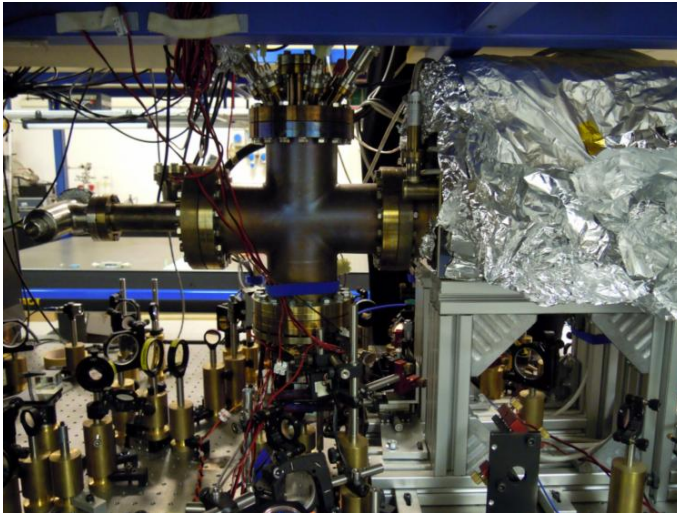


Figure 3.5: Photo of the vacuum chamber mounted on to the optical table.

3.3 Atom-Chip

This section is dedicated to the core of the apparatus, the atom chip. This part is important because it is where the experiment is preformed and a great part of the time spent on the design and building of the experiment is invested. The atom-chip is composed by: the chip, where the condensate is made; a millimetric wire z-shaped behind the chip, to magnetically trap the atoms; two U-shaped conductors behind it; thermocouple and a heater to have a control over the temperature of the chip.

3.3.1 Chip

The chip used in the experiments presented in this thesis consists of an evaporated gold layer on top of a silicon surface. The gold layer has been structured by photolithography whereby the wires of several widths (50, 125, 300 μm) have a height of 2 μm and are defined by 10 μm -wide gaps. The chip was produced by the Quantum optics group of the University of Vienna, that has a long experience developing atom-chips.

A layout of this atom chip can be seen in figure 3.7. The asymmetric dimensions compensate the beam diameter during the mirror MOT phase, since the beams hit the chip at 45° a factor $\sqrt{2}$ on the diameter of the incident beam has to be compensated to use all the chip surface without changing the beam diameter. A z-shaped wire is in the center of the chip. This z will generate the potentials for the final IP trap, where the condensate is produced. The z has a length of 2 mm and its arms are 6 mm long, the width of this wire was set to 125 μm . The resulting resistance is 1.63 Ω . In choosing the width w and length d of the central section of the z-wire we have to make a compromise between attainable trap frequencies (small w) and a large trapping volume (large d and large I) on one hand the acceptable ohmic heating within bounds (small d , small I , large w) on the other hand.

This chip was fabricated by standard microfabrication technology. A very flat silicon substrate, thickness 525 μm , isolated on the top by a thin (smaller than 100 nm) layer of SiO_2 is covered with photoresist which is structured by photolithography. After evaporating an adhesion layer (30 nm of Ti) and the final gold layer (1–5 μm) the remaining resist is removed in a lift-off process. In this way 10 μm -wide gaps defining the wires have been produced (Fig. 3.8

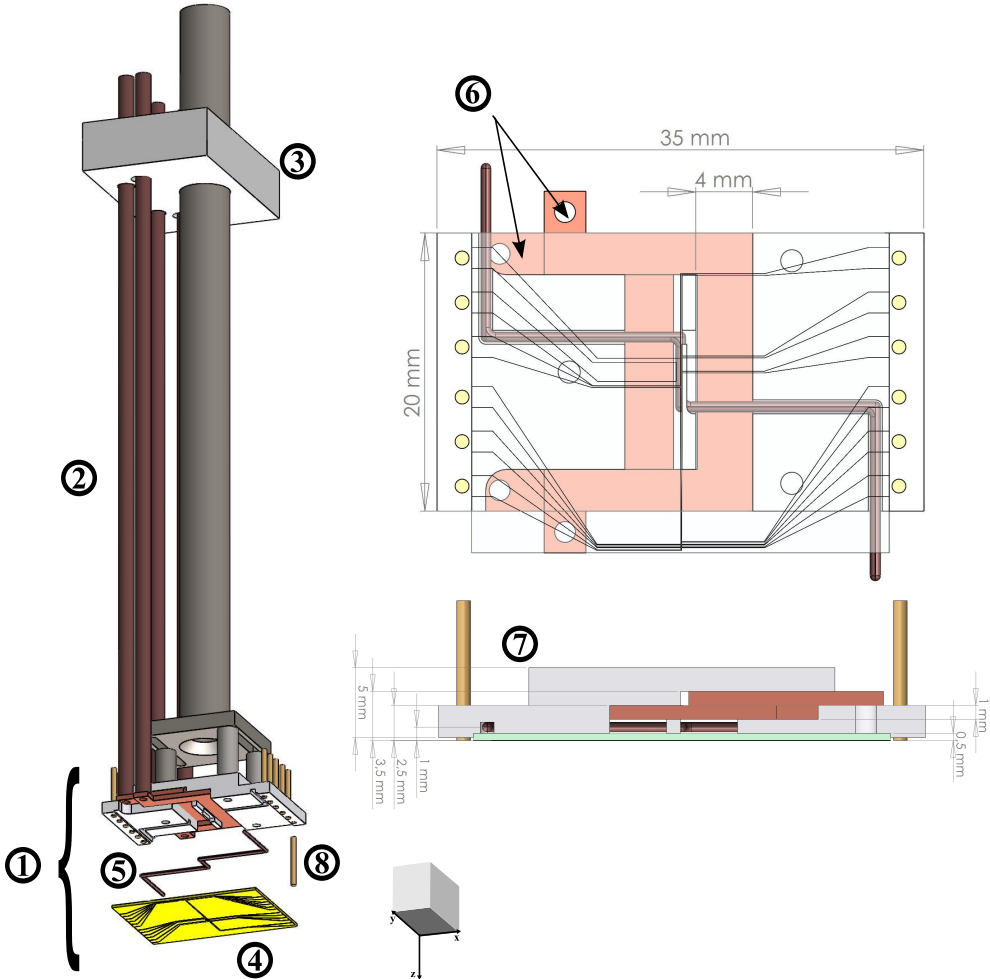


Figure 3.6: Exploded view of chip mount. (1) atom-chip, (2) cooper rods, (3) Feedtrough. (4) chip, (5) Z-shaped kapton wire, (6) U-shaped conductors, (7) shapal holder, (8) gold pins.

(b)). The whole chip is covered by a high-quality gold layer serving as a mirror for the integrated mirror-MOT.

The resulting gold surfaces (figure 3.8 (a)) are smooth (grain sizes < 50 nm), and the wire edges are clearly defined, see figure 3.8 (b). The surface quality depends on adhesion properties and the substrate smoothness. Exceptionally high-quality wires are essential because smallest inhomogeneities in the bulk of the wire and on the edges can lead to uncontrolled deviations of the current-

3. APPARATUS AND METHODS

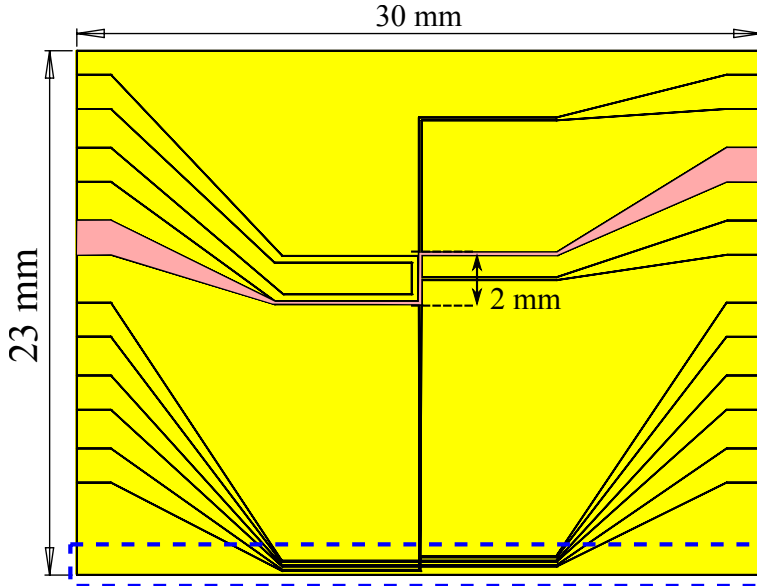


Figure 3.7: Layout of the chip wires, the z-shaped on-chip wire used in these experiment is highlighted in red. It is in the center if we do not take into account the small portion on the chip enclosed by the dashed rectangle, which is planned for the experiment with the photonic crystal.

flow and therefore to disorder potentials in the trapping potential see [65, 66].

Directional deviation in the trapping wire current influences the trap minimum see [51, 52], and the variable conductor thickness yields a spatial fragmentation of the atomic cloud. Fig. 3.9 shows the result of a sample wire measurement by the surface electron microscope (SEM). The measured 4 nm roughness was small enough not to introduce noise in the magnetic potential.

3.3.2 Under-chip

Below the chip we have different components which add some interesting features to the system. To pack and give some solidity is used a ceramic block, excavated to fit the various objects. We machine our ceramic disc from shapal because: It is not conductive, necessary to isolate different conductors and it is as easily machinable as Macor but has a thermal conductivity that is 100 times higher. The block is connected to one feedthrough consisting in one rod of steel, 60 cm long, fixed to the vacuum chamber.

On the backside of the shapal block a mini-heater and a thermocouple were

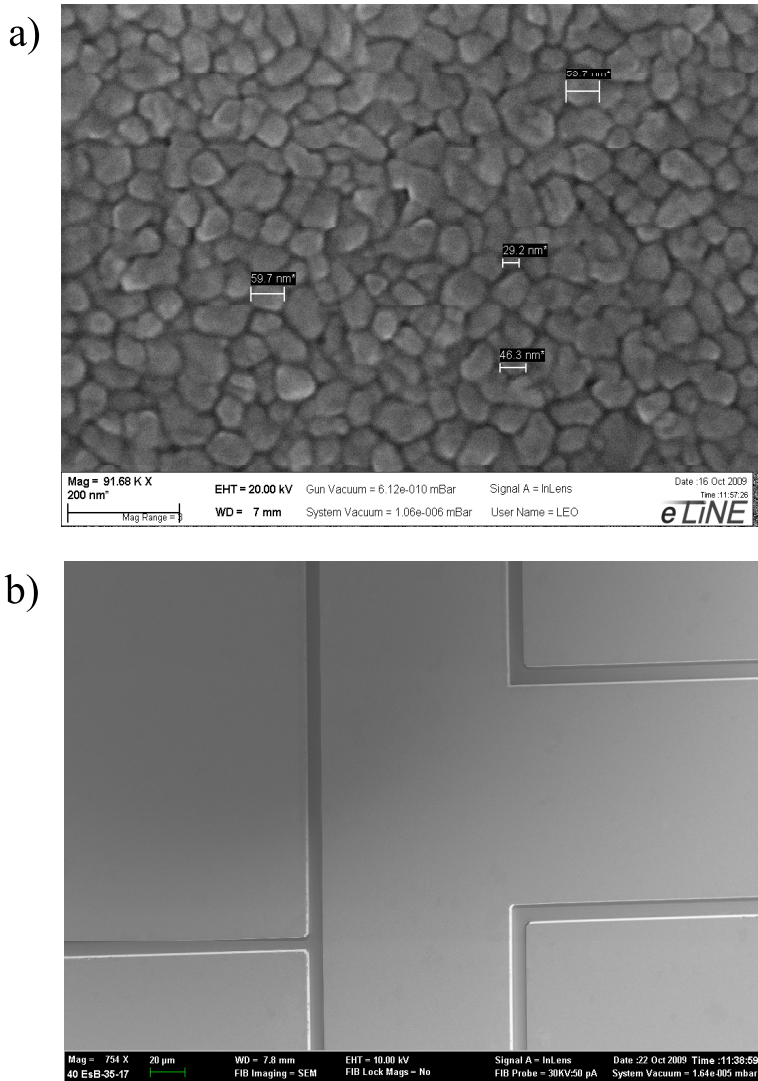


Figure 3.8: a) Scanning-electron microscope (SEM) picture of a top of a microwire fabricated by evaporation. A typical grain size was estimated to be 50 nm. b) Picture of a section of the whole atom chip. The gold wires are defined by 10 μm -wide gaps where no gold has been evaporated.

glued. In initial experiments we had noticed that Rb atoms that had stuck to the microtrap assembly would desorb from the microtrap during the magnetic trapping stage at the moment the assembly heats up. These desorbed Rb atoms had a detrimental effect on the magnetic trapping lifetime. The problem of the decreased trap lifetime due to desorbed rubidium was solved in the most

3. APPARATUS AND METHODS

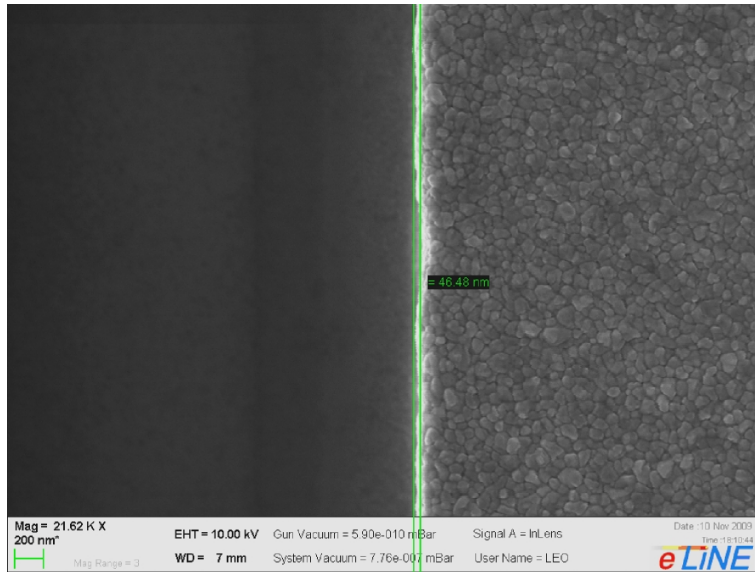


Figure 3.9: SEM picture of a side of a microwire of the chip. Peak to peak edge roughness amounts to ~ 47 nm

recent setup where the Rb beam was directed away from the chip and the chip mount was heated to 40 °C while the experiment is not running to clean the chip mount. This heating is done by a mini heater UHV compatible (343-HEATER- 2×10), of 27 W, and controlled by external regulator and a UHV thermocouple placed near to the heater.

The top of the shapal block was dug to place a macroscopic Z-shaped and two U-shaped conductors, see figure 3.6. With the correct bias field, the magnetic field produced by the current flowing into a U-shaped conductor of millimetric dimensions can approximate a quadrupole configuration around the zero field point, and thus can substitute the standard quadrupole coils pair. The problem of matching the quadrupole magnetic field with the 45° directions necessary for the MOT beams was resolved by the group of Schmiedmayer, [39]. They have used a deformed U-shape conductor, with its central bar much wider and thinner than its sides. This leads to a more slowly space-varying field and the matching region volume grows.

Adding new free parameters to the system allows to get further useful degrees of freedom. In this experiment we wanted to test the following configuration: The deformed U-shape conductor have been substituted with two

independent U-shaped wires. The conductors are made of copper, and have the following dimensions: the section is 1.5 mm high and 2 mm wide, and the width of the whole U is 16 mm. They are placed in two different planes. The upper structure has a length of 9 mm and is just below the mirror, the lower one has a length of 11 mm and lays just below the upper one, see figure 3.6 (6). We can independently drive them with two remotely controlled power supplies and they are electrically isolated by a 0.125 mm thick kapton foil (KAP10).

Macroscopic Z-shape conductor, large IP trap

After mirror MOT stage a large number of atoms can be cooled to $\sim 20 \mu\text{K}$ in the close vicinity of the chip surface. To transfer these atoms into the pure chip traps, it is advantageous to use a large volume Ioffe trap as an intermediate step. This trap is provided by a macroscopic copper wire insulated with kapton (cross-section 0.61 mm and 0.87 mm with jacket, KAP2) which allows to trap more than 10^8 atoms and even cool them to a BEC [67, 68].

The problem of capture the atoms from the molasses into the magnetic trap of the chip, is caused by the small capturing volume of the microscopic on-chip trap compared to the typical size of the molasses of $x \times y \times z = 1.5 \times 1.5 \times 3 \text{ mm}^3$. To enable a better transfer the Z-shape provides a large volume Ioffe trap: a broad kapton wire (compare with the microstructure of the chip) can be used as a Z-shaped wire. This allows to push higher wire currents and thus to form the minimum of the trap further away from the chip surface. Additionally the slope of the magnetic trapping potential for distances close to the chip surface gets more shallow. The calculated potential shown in Figure 3.10 (red curves) corresponds to a wire current of $I_{wire} = 25 \text{ A}$, at 0.2 mm the trap bottom to 1 G, we can see that the problem is the chip surface limiting the potential depth. This trap can be used to load the atoms more efficiently from the molasses and successively compress them to the final z-trap formed by the small z on-chip in the center of the chip. An additional benefit of such small-scale circuits is that their low inductance enables rapid changing and switching of the potentials.

3. APPARATUS AND METHODS

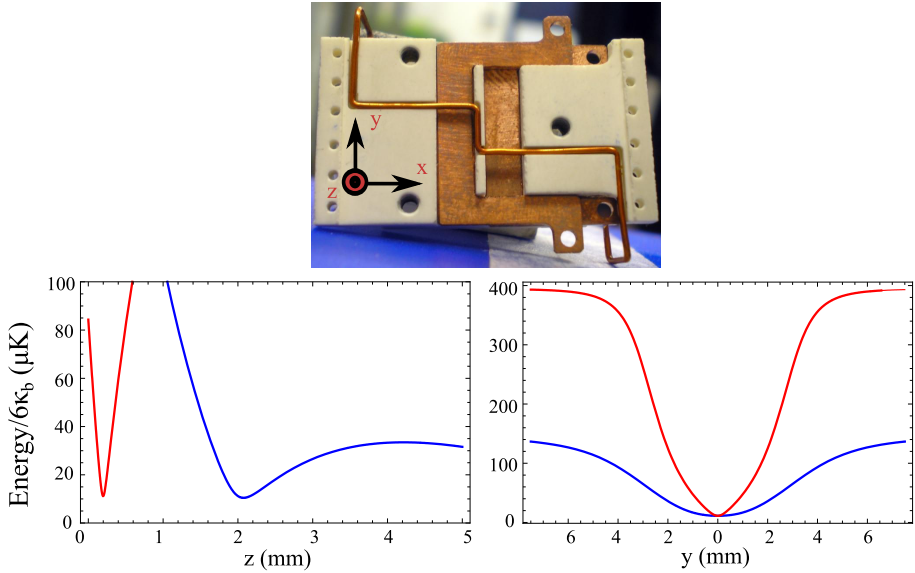


Figure 3.10: Calculated modulus of the magnetic field of 25 A running through the Z-shaped kapton wire, with minimum at 2 mm (blue curve) and at 0.2 mm (red curve) distances from the chip surface. The trap depth should be large compared to the mean atomic energy, the ratio between the two of 6 and more ensures that there are no losses of thermal atoms. Up: a photograph of the Z kapton wire structure embedded in a shapal block. Middle left: Modulus of the magnetic field versus distance from the chip (mirror surface is at $z = 0$). Middle right: Modulus of the magnetic field in the axial direction parallel to the Z-shape wire. The red and blue line are referred to the two minimums in a).

3.3.3 Assembly

In the assembly process special care is taken to create optimal epoxy adhesion layers. The two epoxy components were carefully weighted on a precision balance and mixed. We heat the mix to $\sim 40^\circ\text{C}$ to decrease the viscosity. This mixture is degassed in a desiccator for one minute. Keeping the epoxy in vacuum for longer harms the mixture because essential chemical components get extracted. The epoxy was cured in air at 150°C for 1 hour. During the warm up the epoxy becomes very fluid and tends to creep onto the mirror surface. To prevent this from happening the chip edges were designed to extend 1 mm over the supporting shapal layer. In figure 3.11 we show some pictures taken during the construction process of the microtrap.

The assembly process is performed in several curing stages. In the first curing stage the heater and the thermocouple are glued onto ceramic disc and

the connector gold pins for the chip wires are glued in place, the heater is electrically connected by an electrically conductive silver epoxy (UHV Glue-H27D) to two kapton wires (KAP2). In the subsequent curing stage the Z-shaped kapton wire for the large IP and the U-shaped conductors are glued into the groves in the ceramic disc. Kapton foil was placed between the conductors to isolate them. After removing the excess epoxy with a mill and careful cleaning we place a drop of Epo-tek 377 in the middle of the ceramic disc and glue the microchip on it in the last curing stage. The twelve on-chip wires are connected to the contact pins with 20 μm -diameter aluminum wires with a wire bonding technique, each contact pad being bonded with 10 wires. The rectangular crystal wafer containing the PC structure is delicately placed and glued onto the chip, in the zone enclosed by the dashed rectangle on figure 3.7. The packed chip is mounted onto the feedthrough and all the electric connections are made. The two U-shaped conductors are connected to high power feedthrough by four cooper rods, the gold pins are crimped to kapton wires (KAP2), two dispensers are placed at both large sides of the chip and all the wires are then connected to a set of vacuum feedthroughs. Finally, we insert into the vacuum chamber and start the baking process.

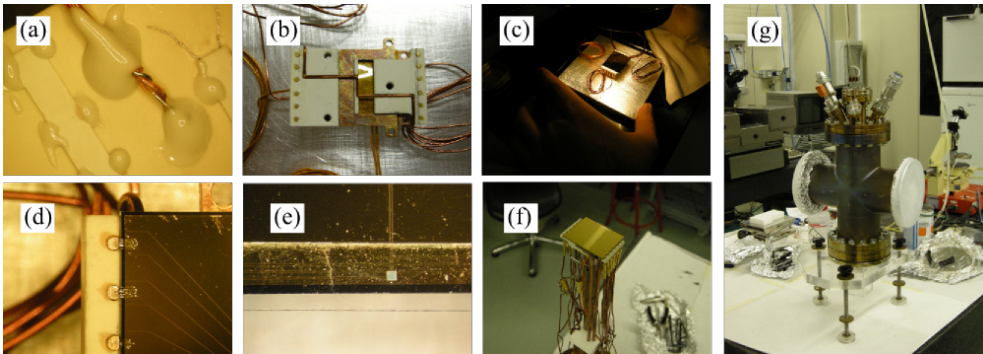


Figure 3.11: Snapshots in sequence of the assembly of the atom-chip: (a) 1st. Gluing and curing of the thermocouple and heater on the backside of the shapal basis, including the wire connections; (b) 2nd. Gluing and curing of the macroscopic Z-shaped kapton wire and U-shaped conductors and the pins to connect the chip on the top of the shapal basis; (c) 3rd. Gluing and curing of the chip onto the shapal; (d) 4th. Gluing and curing of the crystal substrate with the PC onto the chip; (e) 5th. Bonding wires to connect the chip terminals to the pins; (f) 6th. Plug the packed chip onto a central feedthrough and connect all the atom chip electrical terminals to the feedthrough of the cluster and place the dispensers; (g) 9th. close the vacuum chamber.

3.4 Magnetic coils suit

The loading of the cold atoms into the mirror-MOT requires atom chip mirror and external 45° tilted anti-Helmholtz coils pair. During the different stages of the cooling cycle, one applies external bias fields generated by the magnetic coils. The external magnetic bias fields are also used to manipulate the cold atoms. Therefore, the coils play one of the most important roles in the entire atom-chip system.

We have built two different versions of coil suit: one with circular coils and a one with rectangular coils. A circular coil hat, see picture 3.12, was built for a set-up with the quadrupole field generated from two big U-shaped conductors below the chip, hence the space requirements were more relaxed. In last set-up the quadrupole field is generated from anti-Helmholtz coils and to fit all the coils whole system had to be redesigned. To fit all the coils a second version of the coils suit was built with rectangular coils. In this case the whole the system is more compact and faster, low inductance, than the previous version. All the experimental results and measurements that do not specify the coils in this thesis are done with the rectangular coil suit.

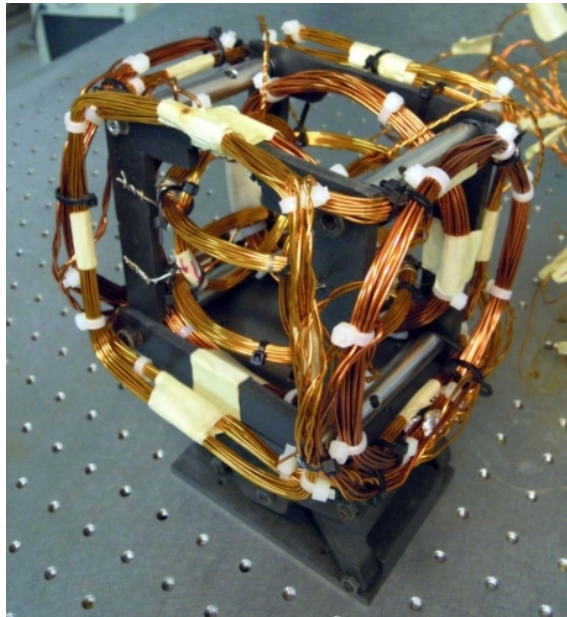


Figure 3.12: Pictures of the old circular coil suit.

The current sources play an important role in the manipulation of the magnetic field. Low current noise is essential and at the same time fast switching of the field is needed. The current source driver is home-made, allowing us to have all the control of the characteristic of the drivers which is usually not possible with their commercial analogues.

3.4.1 Coils suit

To design the magnetic coils five points have to be taken into account:

- The limited space of the system. All the coils have to share the space with the laser beams and the vacuum connection to the cell.
- The intensity of the field, the minimum gradient from the MOT coils is set around 9 Gauss/cm and a maximum bias field of 60 Gauss, in the x direction, needed for high compressions in the magnetic microtrap.
- Minimizing the heating of the coils during the cooling cycle is essential to make the system stable, for this the resistance of the coils has to be as low as possible.
- Homogeneity of the fields in space is required. To prevent the atomic cloud from moving away during the different phases of the experiment, it is essential minimize the gradients for the bias coils. And the quadrupole should not suffer deformations from the loading point to the loading of the magnetic trap. To do this one needs bigger and rounded coils, and to try to maintain the Helmholtz condition for the distance between them, or the anti-Helmholtz condition in the case of the quadrupole coils.
- Minimizing the inductances of the coils is another important point, low inductances allow for a fast switching of the magnetic field. To improve this point one has to reduce the numbers of turns per coil and reduce the diameter of the coils.

Design and simulation were aided by the program Radia due to its capacity to simulate magnetic fields and at the same time graph a 3D representation of the objects. Figures 3.13 and 3.14 are 3D image from Radia and show pre-design of the coils and the main space constraints, glass cell, beams and the flange to connect with the vacuum system. From these images one can check the space availability for the coils.

3. APPARATUS AND METHODS

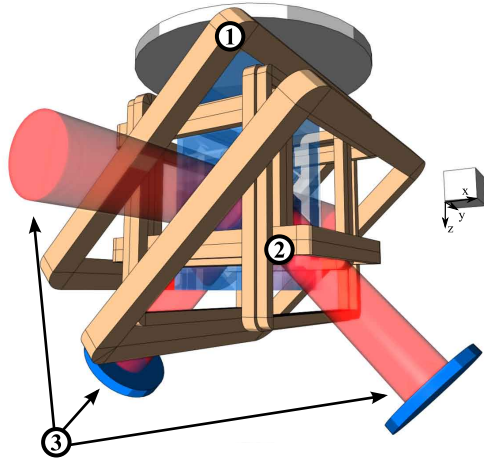


Figure 3.13: Atom-chip mirror MOT configuration with the coil suit. (1) MOT coils, (2) bias field coils, (3) MOT beams.

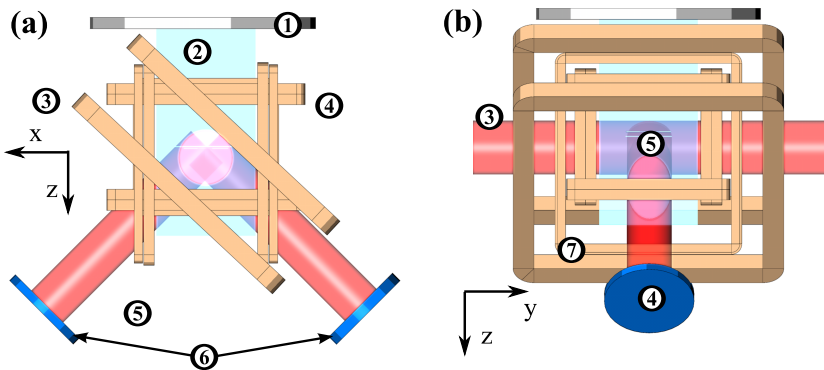


Figure 3.14: Lateral (a) and front (b) view of the magnetic coil suit: (1) Top flange, (2) glass cell, (3) MOT coils, (4) bias z coils, (5) bias x coils, (6) MOT beams and (7) bias y coils.

The rectangular coils are much easier to integrate into one hat unit because they have more contact area, so the first choice was to change from circular coils to rectangular. The main problem with the rectangular coils is the homogeneity of fields with respect to the circular coils, the simulations of the fields demonstrate that the fields are homogeneous enough for our purpose, see field simulations in table 3.16, in a region where the different traps will be applied.

The Helmholtz condition for the bias coils and the anti-Helmholtz for the quadrupole coils are known:

$$d_H = \frac{1}{2}R \quad \text{Helmholtz condition,} \quad (3.1a)$$

$$d_{aH} = \frac{\sqrt{3}}{2}R \quad \text{anti-Helmholtz condition} \quad (3.1b)$$

where R is the radius of the coils and d is the distance from the center of symmetry of the fields to one coil, these conditions were perfectly accomplished. Since space restrictions and the different position of the cloud make these conditions impossible to achieve, they were taken as a starting point to set the coils. As before the simulations of the field were used to verify that we are still within the acceptable limits, see field simulations on table 3.16.

The bias-field coils were made as small as possible to have the smallest inductance, but letting some free optical access for future experiments. In this sense the number of turns per coil was selected as low as possible and in order to get sufficient fields it is preferred to increase the current through the coil.

The system of reference was set as in the 3D pictures 3.13 and 3.14, and is used in the simulations and in the description of the experiment in this thesis. To have the control of the magnetic field in all directions six orthogonal pairs of coils, two for each direction, were built.

To maintain the structure of the coil a normal epoxy was used, instead for the MOT coils a heating conductive epoxy was used to increase the heat dissipation. The six pairs of bias coils are glued together by normal epoxy, the use of the glue permits a more compact set. Finally, we assemble the bias coil set and MOT coils with the aluminum mount structure to form our coil hat, as shown in figure 3.15.

The specifications of the coils are given in table 3.16 and a picture of the

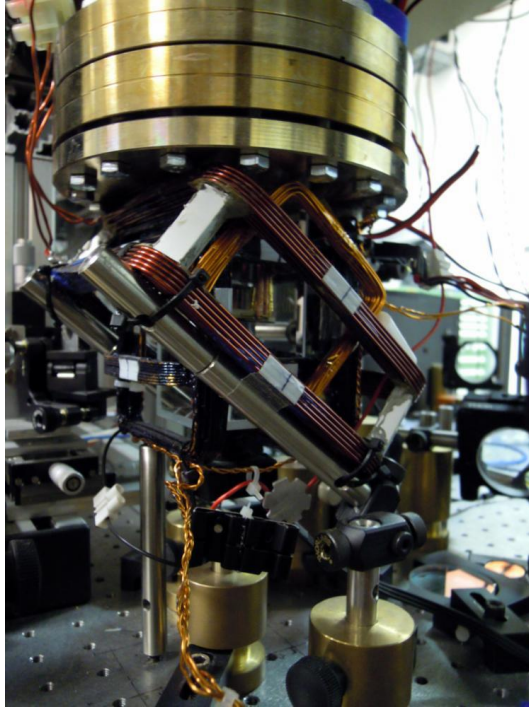


Figure 3.15: Picture of the new rectangular coil suit mounted.

new coil suit is shown in figure 3.15. There are two sets for each bias direction which allow to work with both direction of the field. The coil suit has a clear aperture size of $40\text{ mm} \times 30\text{ mm}$ for laser beams on each side and complete free window at the bottom of the cell.

3.4.2 Current power supplies

To control the magnetic fields during the experiment, currents through the various coils and the wires of the atom chip have to be switched and/or ramped. The current control circuit that we use is shown in figure 3.18 and is based on a feedback propriety of operational amplifier, OP, see figure 3.17. Six of these circuits were built for the experiment.

The switching element is a field effect transistor (MOSFET). In the steady state, the circuit provides a current that is proportional to an analogue control voltage. The switching characteristics are determined by the characteristics of the load and the time constant of the integrator. The circuits are built on

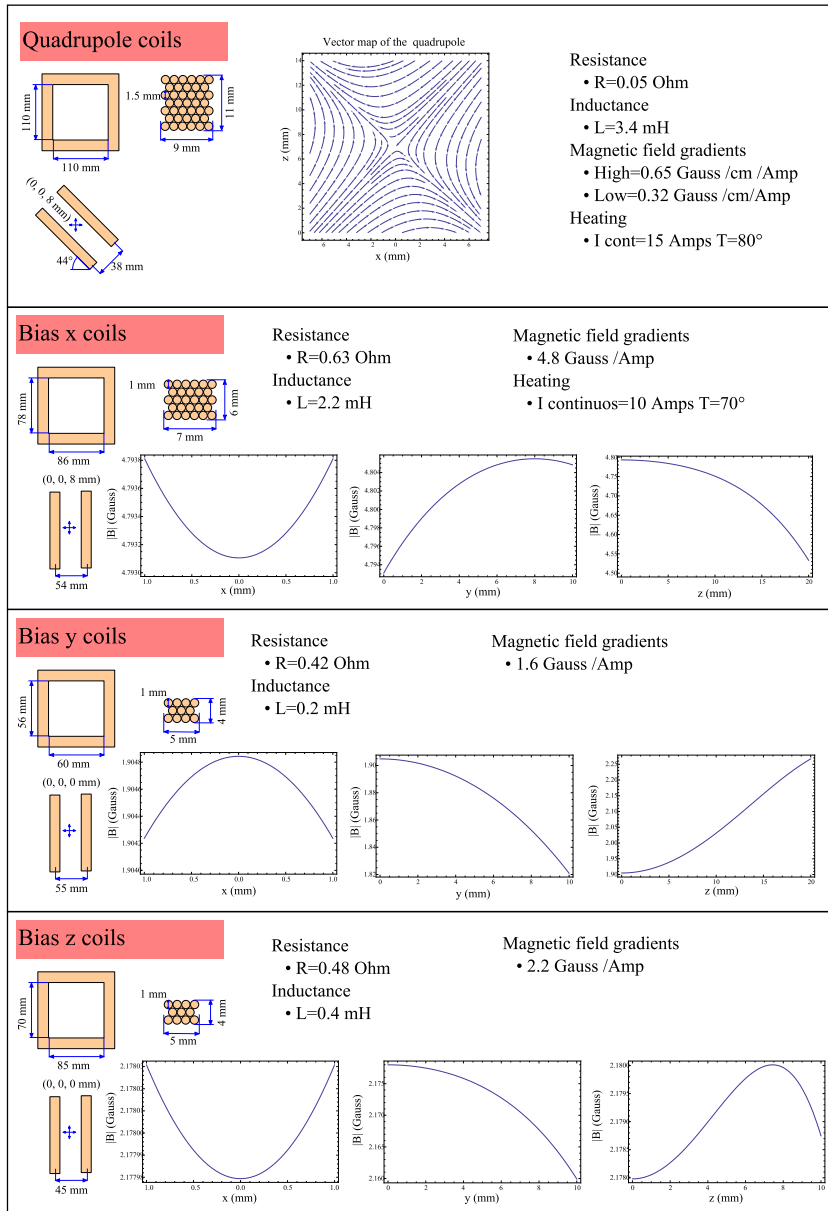


Figure 3.16: Report with physical and magnetic characteristics of the coil suit.

aluminium heat sinks to dissipate the heat produced by the MOSFET and the sense resistor. In its original form with purely integral gain, this circuit works well when driving resistive loads such as the guide and end wires. The current through these wires can be switched on and off in $100 \mu\text{s}$. The voltage

3. APPARATUS AND METHODS

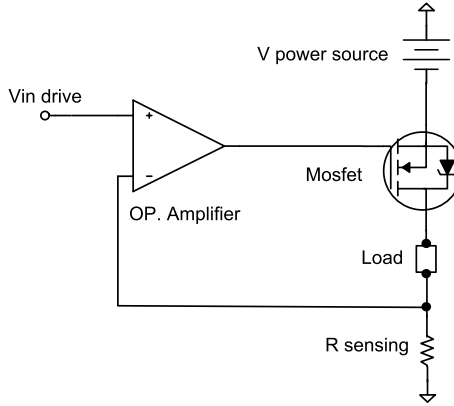


Figure 3.17: the current driver schematic circuit. The $I(V_{in})$ transfer function is set by R sensing.

of the power supply that drives the load must be carefully adjusted so that it is just sufficient to drive the required current. Any additional voltage is dropped across the MOSFET, which may then have to dissipate excessive power. Operating for long in this regime is not the optimal for the MOSFET, which could be get burst. In the case of coils and wires that are inside the vacuum, this is disastrous, as the MOSFETs blow to a short circuit. A relay-based protection circuit was developed that trips on sensing the over-current that occurs when the MOSFET fails. However, this is not fault-proof either, and so extreme vigilance is currently used to protect the wires in the vacuum.

Driving inductive loads such as coils is more difficult. Here the load has an inherent time-constant which depends on the inductance. Trying to drive the load faster than this with the circuit as shown in figure 3.17 results in substantial overshoot. Increasing the voltage on the power supply helps by allowing a higher short-term current which speeds up the response of the load. However, this strategy is limited by the power that the MOSFET can dissipate, as once the circuit had reached its steady state, the additional voltage is dropped across the MOSFET. One gets around this by adding some proportional gain to the circuit using a resistor. This allows much higher switching speeds at short times, while the integrator ensures the correct, stable value of the current at longer times. An inductive load also makes the circuit much more likely to oscillate as stray capacitance can cause the circuit to behave as an LCR resonant circuit. For example, the bias coils have a resonance at about tens of kHz.

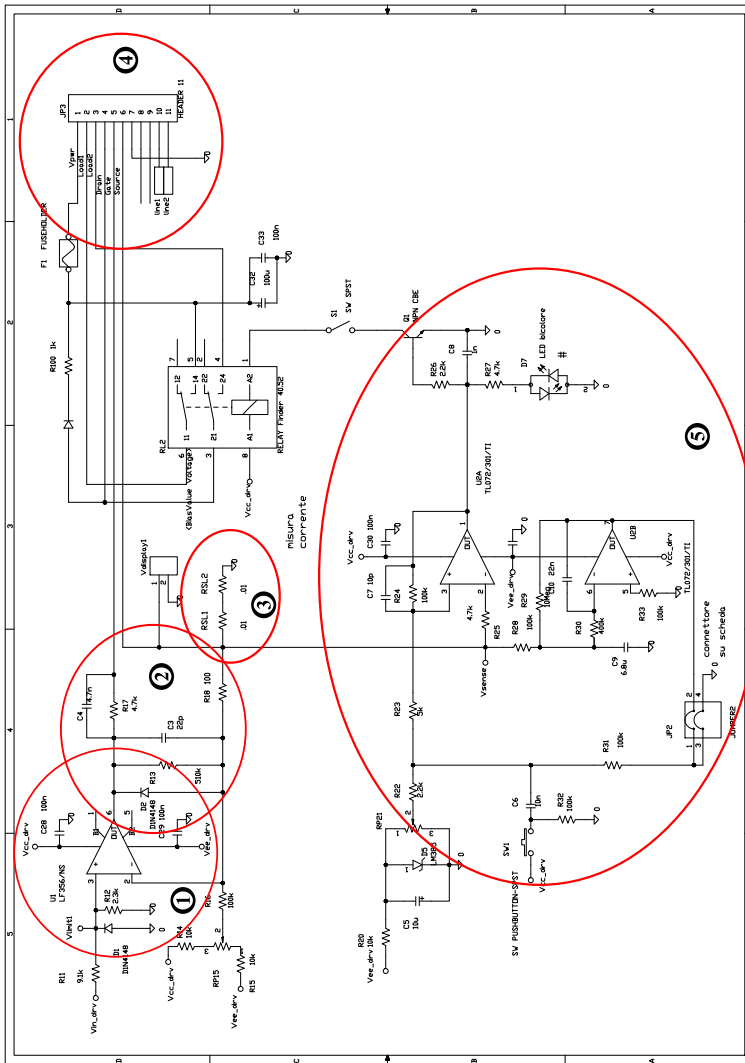


Figure 3.18: The current driver circuit. Different parts of the driver circuit are shown by red circles. (1) OP Amplifier for the feedback, (2) compensation circuit network, (3) the sense resistor for measuring the current, (4) power source, MOSFET and output for the load are outside, (5) protection circuit.

A compensation network was added to lower the feedback response of the OP amplifier and the gain at high frequencies to reduce this problem. With these modifications, the current in the coils can be switched in less than $300 \mu\text{s}$, exact time depending of the coil set used. The figure 3.19 shows the current through the bias x coils with the compensation network disabled and the re-

3. APPARATUS AND METHODS

sultant inductance of the paired coils greater than the inductance of each coil separately. Matching the correct values on the compensation network one can cancel the oscillations in a short time as is shown in figure 3.20.

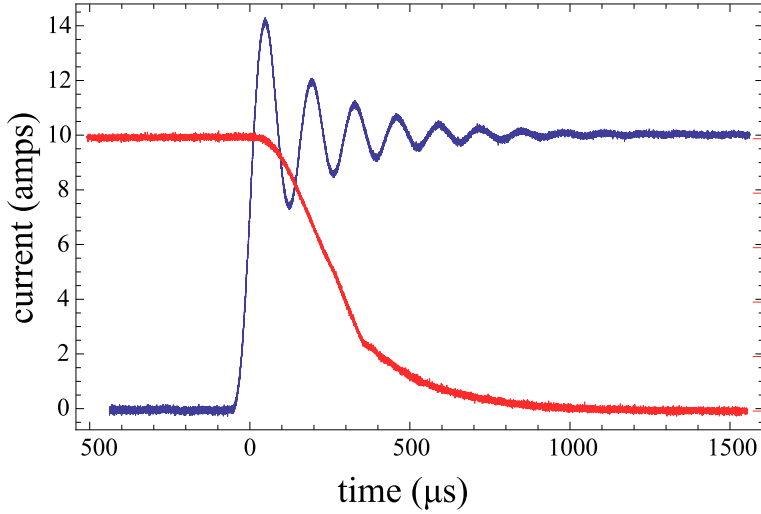


Figure 3.19: The switching on (blue) and off (red) of the current in the bias coils with the compensation network not working.

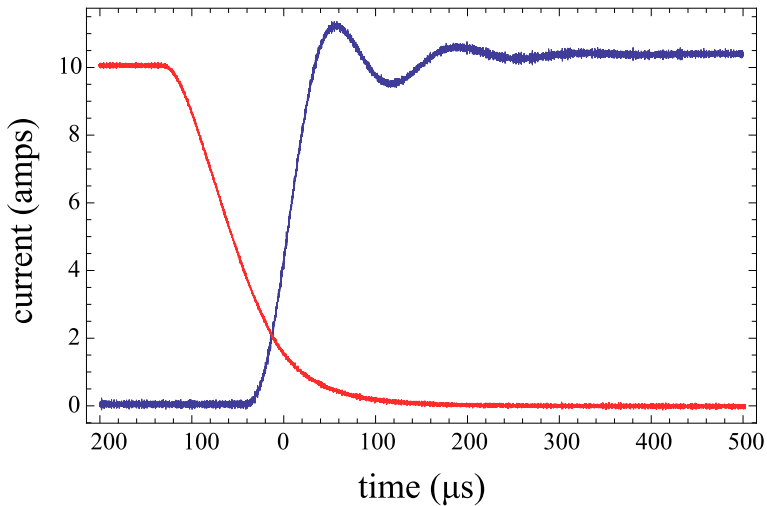


Figure 3.20: The switching on (blue) and off (red) of the current in the bias coils with compensation network working.

Low current noise is essential for reaching BEC since noise in the magnetic field can lead to heating of the trapped cloud, especially if it is at a frequency

close to the trap frequencies. When the MOSFET circuit is operating correctly, the noise level is limited to the noise in the control voltage signal. The RMS level of current noise is less than $\Delta I/I_{max} = 1 \times 10^{-4}$ over the bandwidth from 20 Hz to 300 kHz in all cases and the spectrum shows a noise level below -110 dB V_{RMS} , see figure 3.21.

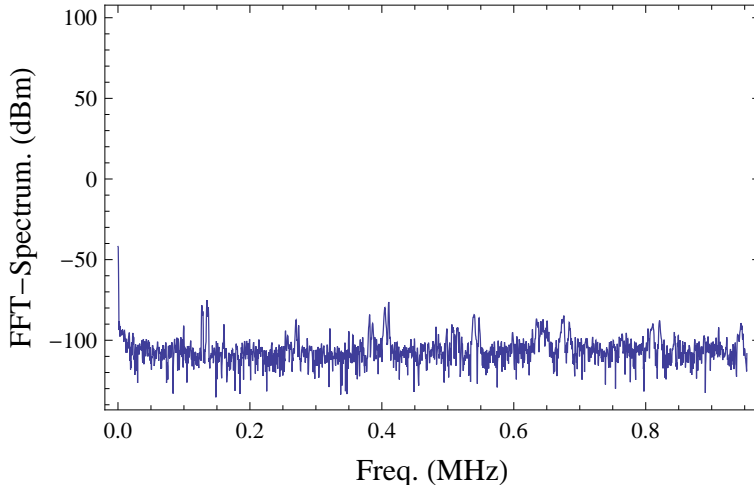


Figure 3.21: The diagram shows the FFT-spectrum of the home-made current source between 0 and 1 MHz. The measurement was taken at 3 A and an ohmic load of 2Ω Trigger: AC line.

3.5 Radio-Frequency Evaporative Cooling

Evaporative cooling is neither a new idea nor a physics patent, but part of our daily life. For thousands of years, people have used this technology to cool boiled water. Just as high-temperature molecules escape from hot water so that the remaining water is cooled down, evaporation continuously removes atoms in the high-energy tail of the thermal distribution from the trap.

A straightforward way to realize forced evaporative cooling for trapped neutral atoms is simply to reduce the trap depth and keep its tightness untouched. This method keeps a high enough collision rate to maintain a continuous cooling process. However in an atom chip the trap frequencies become smaller when the trap depth goes down because the variables to control the depth,

3. APPARATUS AND METHODS

bias or current on the chip, are related as well to the trap frequencies of the wire trap, see 2.3.5.

Pritchard [69] and Walraven [70] suggested using RF-induced spin flip to effectively reduce the trap depth and get forced evaporation. The first RF-forced evaporative cooling was demonstrated by Ketterle's group [71]. Another more direct way, surface evaporation, is to use the flat solid surface of the chip, as a knife in the energy space, to cut the trap depth from top to bottom [45]. In this section, we will also propose a direct evaporation without any external components.

To understand physics of RF-forced evaporation, we assume the atoms are trapped in $m_F = 2$ state, as shown in figure 3.22. If we apply a rotating magnetic field that can drive transitions with $\Delta m_F = \pm 1$, the on-resonance trapped atoms will be transferred to untrapped states. Forced evaporative cooling can be achieved by changing the RF frequency to lower the effective trap depth. In practice, a rotating magnetic field may be difficult to produce experimentally. Fortunately, a vertically (respect to the quantum axis) oscillating magnetic field, for instance, in the x-direction, can be decomposed into positive and negative circular polarizations.

To calculate the frequency needed it must be remembered that for weak magnetic fields, the levels are split linearly according to

$$\Delta E_{|F, m_F\rangle} = \mu_B g_F m_F B \quad (3.2)$$

For $F = 2$ of ^{87}Rb

$$\nu_{RF} = 0.7(\text{MHz/G})B \quad (3.3)$$

We use an Agilent 33250A to supply the RF radiation for evaporative cooling. Optionally we can add an RF amplifier (Mini-Circuits ZHL-3A). However we have found it unnecessary for our final experimental procedure. The RF generator is FM-modulated with an analog input signal setting the frequency in each point of the ramp. The amplitude, as well as the on/off triggering, are set by a RF switch (Mini-Circuits ZYSW-2-50DR). The GPIB channel was discarded because of its response time which is not short and constant (on the order of 70-100 ms), so that using it introduces some instabilities, which are important in the timing of the RF signal. In other experiments where the evaporation cooling stage is longer, lasts minutes, this response time is

less important and the GPIB channel is used. On the atom chips setups this evaporation time is shorter, seconds, and the GPIB is less suitable. On the other hand the analog input cause some noise on the signal, this problem can be avoided by application of a home-made Direct Digital Synthesizer, DDS, adapted to the requirements of the set-up.

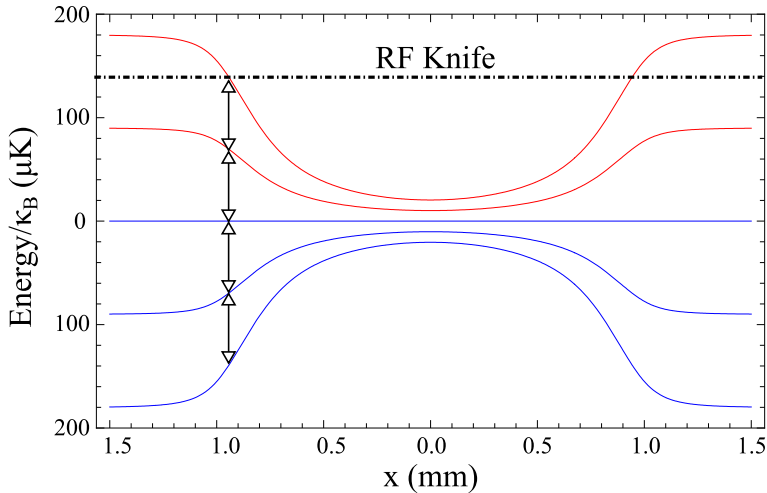


Figure 3.22: The potential for all m_F states of $F = 2$, in red the trapping potentials and in blue the untrapping potentials.

The first RF antenna used on the experiment was a 5 cm diameter coil made from 3 turns of copper wire, and was taped to the outside of the bottom of the glass cell, see figure 3.4. This puts the antenna as close as possible to the atoms while keeping it outside the vacuum. The glass reduces the effect of RF shielding by the steel chamber. In this orientation, the magnetic field produced by the antenna is perpendicular to the trap axis, so that the required $\Delta m_F = \pm 1$ transitions can be driven. The antenna is connected to the RF generator by a coaxial cable. A 5Ω resistor in series with the coil improves the coupling of the radio frequency to the antenna. In the most recent set-up the RF signal is connected to one U-shaped conductor behind the chip which serves as the antenna, about 4 mm from the atoms. In this case no amplifier is necessary.

3.6 Laser System

3.6.1 Overview

Laser light at several different frequencies is required during the BEC experiment. These are illustrated in figure 3.23 along with the hyperfine structure of the ground $5s\ ^2S_{1/2}$ and excited $5p\ ^2S_{3/2}$ states of the D2 transition in ^{87}Rb .

The process starts with the magneto-optical trap. This requires light at two frequencies, for cooling and repumping. The cooling light must be red detuned by a few linewidths from resonance with the $F = 2 \rightarrow F' = 3$ transition. To collect a large number of atoms, one would like as much light as possible 2.2.4. With the high intensity and the mixed polarization of the MOT beams there is a high probability of an off-resonant excitation of the $F = 2 \rightarrow F' = 2$ transition. The $F' = 2$ state can decay by spontaneous emission into the lower ground state ($F = 1$), which is dark. A **repump** laser is required to prevent all the atoms being rapidly pumped into this state and lost from the trap. This is tuned to the $F = 1 \rightarrow F' = 2$ transition as shown in figure 3.23.

During the CMOT phase, the detuning of the **cooling** light must be increased to allow the cloud to compress. After the CMOT, the atoms must be prepared in the $F = 2, mF = 2$ state for magnetic trapping. This is done by **optical pumping**, using $\sigma+$ light on the $F = 2 \rightarrow F' = 2$ transition. The $F = 2, mF = 2$ final state is dark, to minimize the heating of the atom cloud during optical pumping.

Finally, to extract the properties of the atom cloud it must be imaged. This is done using two methods as described in section 3.7. Clouds in the magneto-optical trap are imaged using the fluorescence due to the MOT light itself. Clouds in free expansion and in the magnetic trap are imaged using the shadow that they cast in a **imaging** beam. To get the highest signal, this imaging beam is resonant with the $F = 2 \rightarrow F' = 3$ transition.

There are many ways to get these frequencies, in the different atomic experiments around the world we can find a full variety of schemes. In the next sections it will be explained how we obtain these frequencies in this experiment fulfilling the aims of: wide frequency tuning, strong locking point, high output power and stability of the system.

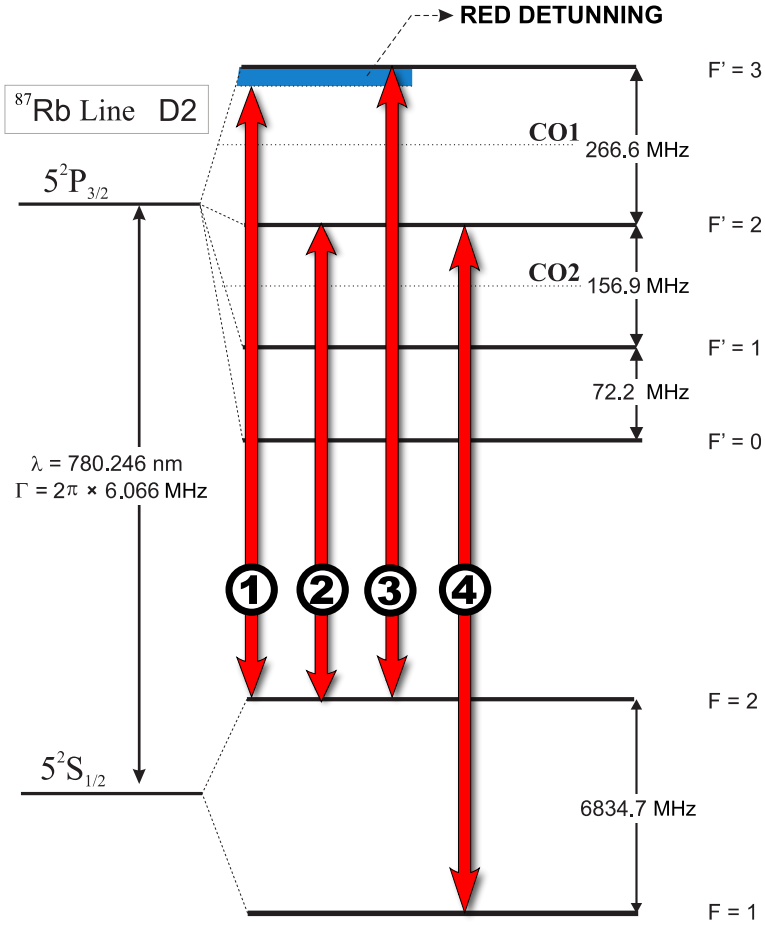


Figure 3.23: The hyperfine structure of the $5s^2S_{1/2}$ and $5p^2P_{3/2}$ states of ^{87}Rb D2 line, from [72], showing the laser frequencies required for the experiment, and the intervals (in MHz) between the hyperfine levels. 1) MOT/molasses cooling, 2) optical pump, 3) imaging, 4) repumper.

The starting point is select the laser sources, during the years the laser sources have changed, but in the final situation we used two DFB laser systems from TOPTICA company (DL DFB model) and one laser amplifier also from TOPTICA company (BoosTA model). All the lasers and devices are placed in a black closed box, see figure 3.24, and connected to the optical table where the science cell is by optical fibers (with the exception of the optical pumping beam). Blocking any scattered light is essential for the condensate lifetime, resonant or near resonant lights destroy the condensate.

3. APPARATUS AND METHODS

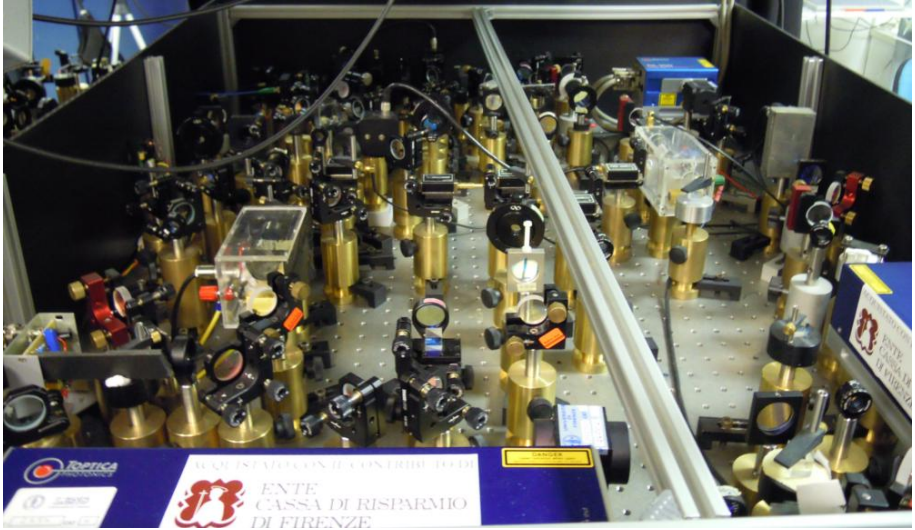


Figure 3.24: Photo of the laser-system box described in this chapter

3.6.2 DFB

Distributed Feedback (DFB) laser diodes feature a grating structure incorporated in the semiconductor chip. The grating restricts the laser emission to a single longitudinal mode and thus determines the lasing wavelength. In a DFB laser, the grating is integrated into the active region (gain section) of the diode.

Frequency tuning is accomplished by thermally or electrically varying the grating pitch. Thermal tuning offers extremely large mode-hop free scans of hundreds of GHz. Electric modulation, on the other hand, can be employed for fast frequency modulation over a smaller frequencies range.

The main advantage of a DFB laser is its extremely large continuous mode-hop free tuning range. Mode-hop free scans of several nanometers are routinely attained. Under some conditions, semiconductor lasers can discontinuously switch wavelengths in a back-and-forth manner. This is called mode-hopping, this featured could become a problem in the searching and locking of atomic line. Typical DFB laser applications are in gas sensing, phase shifting interferometry, the generation of tunable CW Terahertz radiation and in telecommunications more than anywhere else. The mechanical design of a DFB laser comprises no alignment-sensitive optical components, making these lasers par-

ticularly attractive for our applications. The main problem in DFB laser is the small coarse tuning range, some nm, and the linewidth, few of MHz. An ECDL, diode laser systems with an external grating,(External Cavity Diode Laser), is the preferred choice for applications that require a broad coarse tuning range, or an ultra-narrow linewidth, assuming the coarse tuning as not mode-hop free tuning. For our BEC DFB system is good enough and the most important characteristic it provides is a very solid lock, indeed the lasers do not need to be relocked during a typical working day.

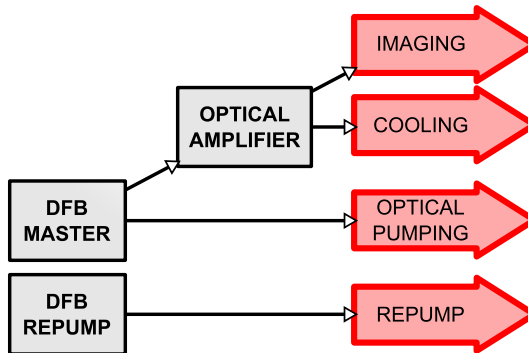


Figure 3.25: Small map of the laser sources and the final needed lights beams.

Two DFB complete laser systems are used, diodes and electronics are manufacturing by TOPTICA, and provide upto 120 mW of laser power each. The system consists of a DBF master laser and a DFB repumper laser. The former generates light with a frequency close to the $F = 2 \rightarrow F' = 3$ transition. Cooling beams come from this laser. The power of the cooling beam is boosted by a tapered amplifier. The later laser is only used for the repump beam.

3.6.3 DFB master laser

DFB master laser provides light for the MOT cooling, optical pumping and imaging, lights near to the $F = 2 \rightarrow F' = 3$ transition. The scheme for this laser is complicated due to the different frequencies that one wants to obtain as well as high cooling power and large detuning necessary for MOT/molasses stages. To understand the laser sources scheme without mistaken, the figures 3.27 and 3.26 shows the different frequencies and power derivations.

Following the figure 3.26, the first element in the beam path is an optical isolator. Optical isolators are placed at the output of all the DFB lasers (DFB repump also) to reduce optical feedback, which can cause frequency noise on the sensitive feedback diode lasers. An optical isolator is also placed at the input and at the output of the BoosTA. The main drawback of the optical isolator is the power losses in the beam. After the optical isolator the loss is of 10 % at least, but in most of the cases is more.

A second important element is a pair of anamorphic prisms. The laser beam from a diode laser is very asymmetric, elliptical, which can reduce the efficiency of many devices, AOM, BoosTA and fiber couplers. An anamorphic prism pair are used to expand a laser beam in one dimension, converting the elliptical beam shape of laser diodes into a nearly circular one. Anamorphic prism pair in the proper orientation will provide magnification ratios from 2:1 to 6:1. With insignificant losses the use of this prisms allows for a sensible improvement of the performance of devices further down the optical path.

This beam is divided into two parts, one going to the the optical amplifier and the other to the AOM 1. To divide the beams a lambda half-waveplate with a polarizing beam splitter cube is used. The same configuration is used to divide any beam in the optical setup, allowing to have the control of the power divisions. Only in the repumper spectroscopy a plastic beam splitter is used since the power is not important.

Acousto-optic modulator

To drive an AOM a RF signal was generated by a Voltage Controlled Oscillator (VCO) and amplified. The working principle of an Acousto-Optic Modulator is the coupling between the photons of the laser beam that passes through the acousto-optic crystal and the phonons of the crystal excited by the RF input signal. The output consist of the unperturbed component (the zero order) and several diffraction components, with optical frequencies differing by multiples of the induced acoustic frequency.

Usually only the first order is used, negative or positive depending of the sign of the detuning require but other orders, second or third can also be used only if the required power is really low. The frequency range of all our AOM models (3080-122) is centered at 80 MHz with ± 20 MHz of bandwidth. In a

3. APPARATUS AND METHODS

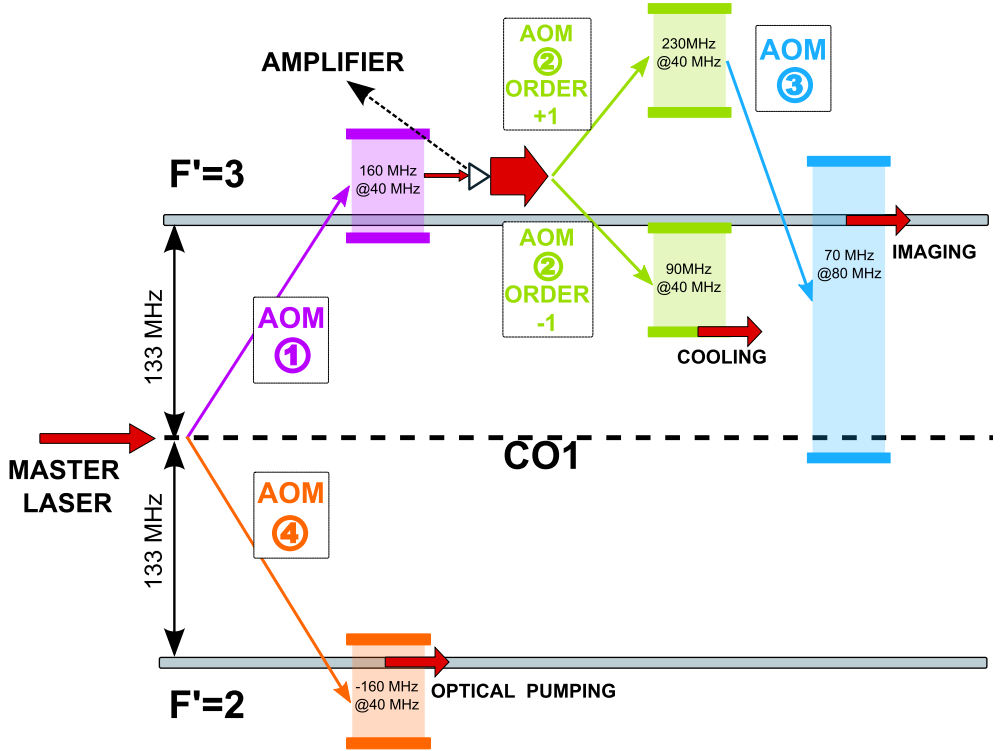


Figure 3.27: Frequency picture of the beams generated from the master laser, the frequencies are relative to the crossover CO1. The bandwidth and center frequency of each AOM its show.

typical double-pass configuration (shown by red, blue and grey areas in Fig. 3.26), the first order diffracted beam is reflected back down the same path through the AOM, thereby experiencing a double frequency shift. Double-pass through a quarter-waveplate rotates its polarization by $\pi/2$, enabling the separation of the output from the input beam by a polarization beam splitter. The double-pass scheme also ensures a constant alignment of the beam for any frequency of the RF signal. By controlling the DC control signal of the VCO, it is possible to continuously tune the frequency in a range of several MHz. This is an important feature since, as we will see, the MOT works for a specific detuning, while the detuning required by Optical Molasses is different.

Furthermore, by controlling the amplitude of the VCO output signal, it is even possible to change the resulting beam intensity, thus allowing for the mod-

ulation of the beam intensity during the CMOT/molasses regime and obtaining a very fast optical switch, about tens of nanoseconds. The AOM efficiency is not very high (in theory 70-80 %) and in a double-pass configuration it is not uncommon to loose even 50% of the total available power.

AOM 1, see figure 3.26, is used in a negative-order double pass configuration, this AOM is used to change by several linewidths the cooling light. A part of the output of this AOM is sent to a frequency modulation (FM) spectroscopy setup to stabilize the laser and the rest to the AOM 4, see figure 3.26, to derive imaging and cooling beams. The AOM 1 is used for a dynamic offset of the frequency of the cooling and imaging lights during the experiment respect to the light sent to the FM spectroscopy. The negative first-order diffracted beam is used in the FM spectroscopy.

This scheme allows us to lock the laser to the peak of the ($F = 2 \rightarrow F' = 2$, $F = 2 \rightarrow F' = 3$) crossover saturation line, CO1 in figure 3.27, and have the cooling light, by the addition of another AOM, red detuned by several natural linewidths from the $F = 2 \rightarrow F' = 3$ cooling transition.

From the output of the AOM 1 ~ 1 mW of light is used for the FM spectroscopy, and ~ 4 mW for another double pass AOM scheme to get the **optical pumping** light. The AOM 4 is set in a double-pass negative configuration that shifts the light to the $F = 2 \rightarrow F' = 2$ transition. This light is mixed in a PBS with some light from repump, resonant with $F = 1 \rightarrow F' = 2$ transition. A single repump beam overlapped with the optical pump beam improved the pumping efficiency in a manner similar to the MOT repumper. Since, no improvement was observed when the MOT repumper, that hits the atoms from all directions, was used, the mixing of the two beams was essential. No optical fiber is used for these beams since their spatial quality is not required for the pumping. At the output of the lasers box we have ~ 2 mW. in the optical pumping beam.

Frequency modulation spectroscopy

To lock the laser a frequency-modulation (FM) scheme is used. Frequency side-bands were generated by an electro-optic modulator (EOM) from QUBIG GmbH (EO-F8L). The EOM's electrical driving circuit is made resonant with the 8 MHz driving signal obtained from a lock-in amplifier (home made). The

3. APPARATUS AND METHODS

low-voltage sine wave (2 V peak-to-peak) yields 4 % modulation depth of the laser intensity. Subsequently the spectroscopy signal is recorded on a fast photodiode (PD in figure 3.26, homemade) and fed in the lock-in where it is phase-shifted and mixed with the 8 MHz oscillator to obtain a dispersive lock signal, see figure 3.29. The lock signal finally enters a PID controller (homemade), that stabilizes the laser frequency by a fast feedback achieved by direct modulation of the laser current. The cheaper option of generating sidebands by direct modulation of the laser diode current was abandoned because the sidebands, however small, ended up in the light needed for the MOT. The presence of the sidebands appeared to be detrimental in the compressed MOT optical cooling stage probably because the red sidebands gave rise to scattering and therefore heating.

Frequency Jump Lock

The use of a double pass AOM before the spectroscopy gives us advantages: no losses in a double pass configuration after the BoosTA, no problems with alignment or power changes during the frequency changes during the CMOT/molasses stage. The common configuration is a double pass AOM be-

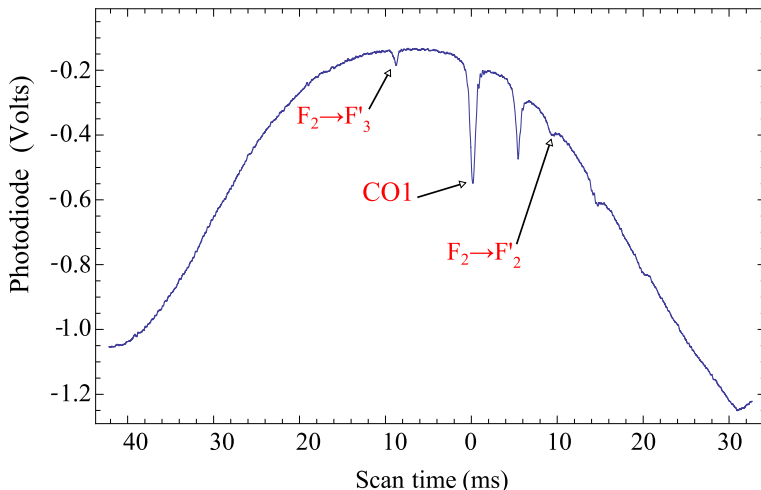


Figure 3.28: The saturated absorption spectroscopy signal for the transition $F = 2 \rightarrow F'$. The signal is taken from the same photodiode used for the FM spectroscopy, but neglecting the fast component.

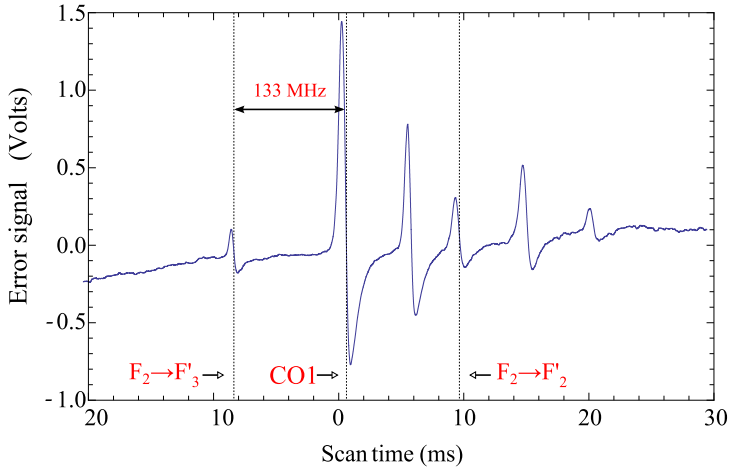


Figure 3.29: FM spectroscopy for the transition $F = 2 \rightarrow F' = 3'$. The signal is taken at the output of the proportional integrator locking system, PI, and is used like error signal for the lock of the laser.

fore the fiber of the cooling light to achieve large detunings, in this case a single pass AOM before the fiber is enough. The drawback of this jump in the spectroscopy is the difficult to relock faster enough the laser after the frequency jump.

A good alignment of the double pass AOM is necessary to maintain a stable signal, it is not sufficient. The lock of the laser is made through a fast modulation input of the laser, trough a fast FET before the diode. A FET and a Bias-T are build by TOPTICA company and are included in the laser module. The FET is DC coupled with the electrical full-width half maximum (FWHM) of (-3 dB) of 20 MHz. This is very fast input to feedback with the error signal of the lock-in. However, slow response from the system, PI + laser, continue to give problems in maintain the lock during rapid changes of the laser frequency. To get around this problem, we use a feed-forward on the laser current avoiding the PI circuit. A special pulse is applied to the external lock input to jump the laser frequency, simultaneously and proportional to the VCO signal, who control the AOM of the spectroscopy. If the change in the laser frequency is matched to the change in the VCO frequency, the laser will remain on the correct fringe and relock at the new frequency. Using the correct pulse, the jump in the laser frequency can be made faster (<4 ms, see figure 3.30 or figure 3.31 when the jump is in the other direction).

3. APPARATUS AND METHODS

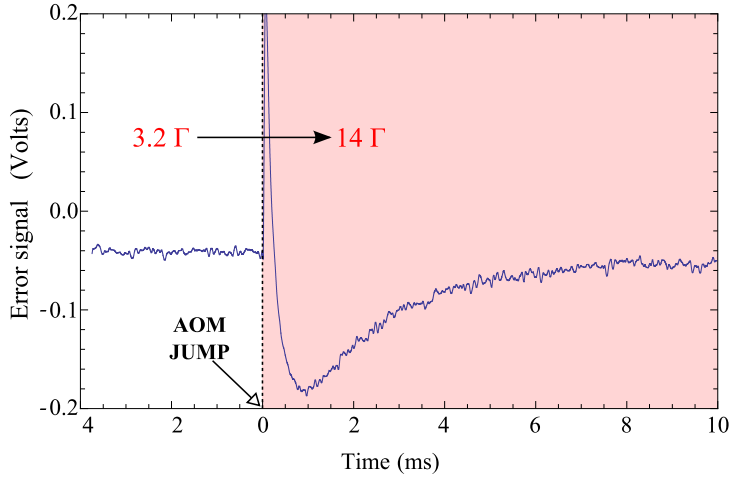


Figure 3.30: The error signal of the PID during a frequency jump for the CMOT stage. The arrow mark shows when the AOM jumps in frequency. From the figure 3.29 we can estimate the fringe of the CO1 locking point dimensions as Volts of the error signal, about 2.5 Volts. The error signal during the frequency jump have a maximum peak of 0.2 Volt. Hence, the laser remains on the same fringe during the jump. The jump is made from 3.2Γ to 14Γ linewidths.

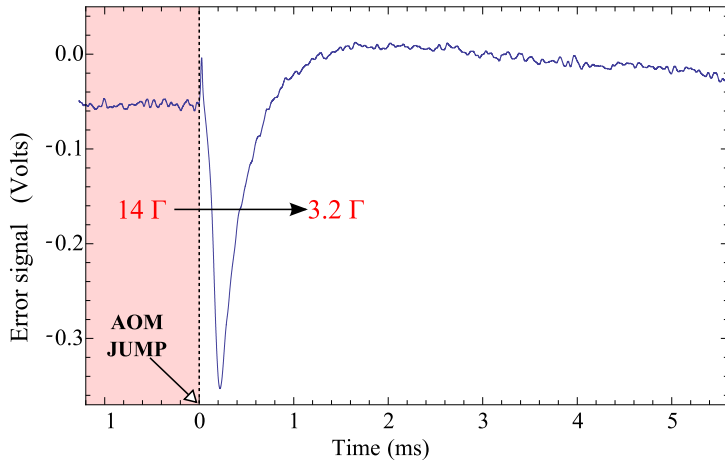


Figure 3.31: The error signal of the PID during a frequency jump for imaging after CMOT/molasses stage. After this stage the light of imaging beam is to detuned and is not possible compensate with the AOM 3 so another frequency jump on the spectroscopy is necessary. The jump is from 14Γ to 3.2Γ linewidths. The arrow mark shows when the AOM jumps in frequency, as in the case 3.30 the laser remains on the same fringe.

From the first cube about ~ 40 mW of light is sent to the optical amplifier, BoosTA, the use of an optical isolator before the amplifier is absolutely necessary, although it decreases the light power for seeding. Pushing the DFB master laser to work at the upper limits of temperature and current we can nearly arrive to the saturation for seeding of the BoosTA. From the output of the optical amplifier we get 850 mW, just 10% less power than is given in the technical specifications.

After the optical amplifier the light is sent to the AOM 2, see figure 3.26. The AOM is aligned to get the maximum efficiency on the negative diffracted order, and the frequency is fixed at 70 MHz. The negative first diffracted order is sent to a PBS cube to clean the polarization and coupled to an optical fiber to be used as **cooling** light.

Due to the great power from the optical amplifier the positive diffracted order has enough power to use, ~ 15 mW. This light passes through the AOM 3, see figure 3.26, in a double-pass scheme. With the negative diffracted order this light can be resonant with the $F = 2 \rightarrow F' = 3$ transition. Finally an optical fiber cleans the spatial profile of the beam to get the **imaging** beam.

Amplifier

Amplification of the cooling light is necessary to capture a large number of atoms. The light from a single diode after passing through a large number of optical devices is not strong enough to capture and cool the atoms. This problem is solved by using an amplifier module from TOPTICA (BoosTA). The BoosTA is an economic amplifier that increases the power of single mode polarized laser light without changing the spectral characteristic.

The BoosTA laser amplifies a 40 mW diode laser to more than 850 mW. The BoosTA works in the same way as a diode laser: the power supply creates a population inversion and as laser light is pumped through, it creates stimulated emission. The drawbacks of this device are the *dirty* spatial profile, so that a spatial filter is needed after it, the seeding instability, so that one needs to realign it 1-2 times a day and low power output if one compares with other optical amplifiers.

3.6.4 DFB repump

The second DFB provides light for the MOT repumping $F = 1 \rightarrow F' = 2$. It is stabilized using the polarization spectroscopy and locked to $F = 1 \rightarrow F' = (1, 2)$ crossover resonance, CO2 in figure 3.23. This technique will be described in more details in the next section. A small part of the light is sent to the spectroscopy and the other part is sent through a single pass AOM, shifting the frequency for +78.45 MHz to be resonant with the required transition. Mechanical shutter in front of the optical fiber are used to fast-switch the light before it is guided to the experiment by a polarization maintaining optical fiber.

Polarization Spectroscopy Lock

The most common technique for sub-Doppler resolution spectroscopy is saturated absorption spectroscopy [73]. Here, the change in absorption of a weak probe beam is monitored as the laser frequency is scanned across the Doppler-broadened transition. A stronger counter-propagating pump beam depletes the population in the lower state, causing a dip in the absorption of the probe beam. The counter-propagating beam geometry ensures that only the atoms in a narrow velocity class near $v = 0$ interact resonantly with both beams at the same time, allowing sub-Doppler resolution. A dispersion signal can be obtained by modulating the laser frequency over a transition peak, and using the lock-in detection. Polarization spectroscopy is a related technique that offers a higher inherent signal-to-noise ratio [74]. Instead of monitoring the change in absorption of the probe beam, we look for a change in its polarization. It allows a dispersion curve to be obtained directly, without the need for modulation of the laser frequency [75]. This has been used elsewhere to stabilize the frequency of diode lasers in ^{87}Rb trapping experiments [76]. The polarization spectrometer setup used is shown in figure 3.32.

The incoming laser light is split into a weak probe beam and a stronger pump beam. A quarter-wave plate circularly polarizes the pump beam, while the probe beam is linearly polarized. The beams overlap in the rubidium cell. The probe polarization is adjusted so that far from the atomic transition, the signal on each of the photodiodes after a cube is equal. When the laser frequency is tuned to an atomic transition, the circularly polarized pump beam

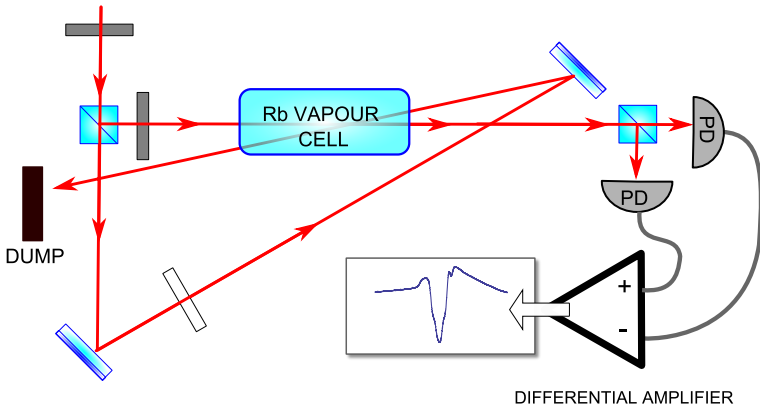


Figure 3.32: Layout of the polarisation spectrometer

causes optical pumping, leading to a non-uniform population of the magnetic sublevels. This anisotropy makes the sample birefringent and dichroic for the incoming probe light. After passing through the cell, the plane of polarization of the probe light is rotated slightly, and its ellipticity is changed. These changes in the polarization state of the probe light are detected as changes in the intensity on each photodiode, taking the difference of the two photodiode signals yields a dispersion curve as the laser is scanned across an atomic transition. No modulation of the laser frequency is required. The counter-propagating beam geometry allows sub-Doppler resolution in the same way as for standard saturated absorption spectroscopy. In the case of the reference laser spectrometer, the rubidium cell is placed in a mu-metal shield to reduce the effects of Faraday rotation on the observed signal.

The performance of this lock is excellent. Despite the somewhat messy error signal, the repumper laser will remain locked for a day. Even severe shocks to the optical table do not cause the laser to jump out of lock. The technique is simple to implement and offers an error signal with an excellent signal to noise ratio without the need for modulation of the laser frequency. The only drawback is that the zero-crossing of the dispersion signal is not fixed, it depends on the orientation of the linear polarizer. Rotating this polarizer introduces an offset, which shifts the whole difference signal up or down.

By comparing the signal with a standard saturated absorption signal from the trap spectrometer, the reference laser frequency can be set with an uncertainty of around 1 MHz. This is adequate for the experiments described

3. APPARATUS AND METHODS

in this thesis. However, for experiments that require the absolute frequency to be known more accurately, this offset would have to be addressed, or an alternative technique used.

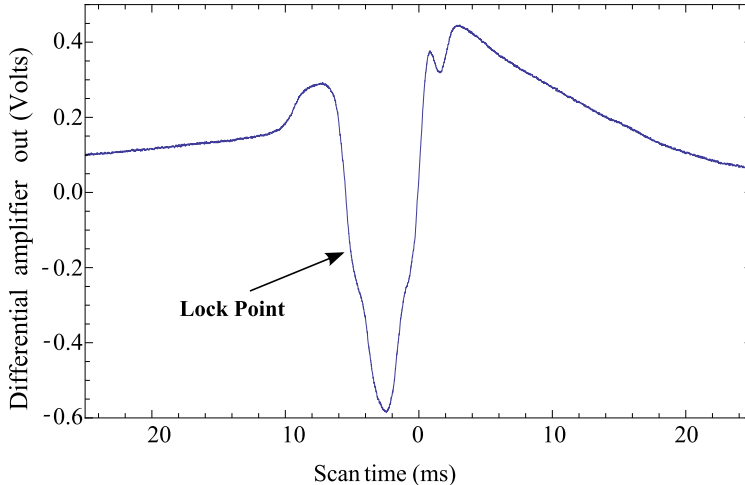


Figure 3.33: The output of the repump laser polarisation spectrometer in a single scan across the ^{87}Rb $F = 1 \rightarrow F'$ transitions.

3.6.5 Shutters

In the experiment, both mechanical shutters and AOMs are used to control the timing of the laser light. The mechanical shutters provide an excellent extinction ratio but have slow response times, on the order of 1 ms and can have timing jitter of a few milliseconds. AOMs are fast, with response times on the order of a 1 μs , but their extinction ratio is less impressive. For critical light pulses such as the imaging pulse, an AOM and a mechanical shutter in series are used. Vibrations associated with the opening or the closing of a mechanical shutter can induce transient noise on the lasers. Two kinds of shutters are used: one is from Thorlabs (SHO5) and is used to block the high power light, is relatively slow (1-2 ms) and noisy. For the other beams we use Sunex (SHT93), a silent and fast shutter, with a home made driver that can open-close in less than 500 μs . It is particularly useful for shutting the light of the optical pumping beam or the imaging beam.

3.6.6 Spatial filtering

The spatial beam profile from diode lasers is not Gaussian and may contain high contrast stripes, that must be smoothed before the light is used in the experiment. Depending on the quality of its amplifier chip, the output of a BoosTA system can be even less uniform than the direct output from the diode laser. While a MOT does not require perfectly uniform beams, high-contrast spatial structure will lower the trapping efficiency. The spatial quality of a beam can be determined by translating a pinhole across the beam and measuring the intensity at each point on a photodiode.

The trapping light is spatially filtered by sending it through a single mode optical fiber, which reduces the power by about 50 %. In the first experiment the trapping beam was focused through a large pinhole (100-50 μm), thus eliminating the higher-frequency spatial modes while retaining most of the laser power ($\gg 75$). By using the pinhole to filter the light, the number of MOT atoms was halved. However, the use of an optical fiber to filter spatially the trapping beam can reduce our shot-to-shot condensate number variation and reduce the need to adjust the trapping beam alignment from once a day to once every other month. The MOT is largely insensitive to the spatial profile of the repumper beam, hence no spatial filtering is necessary for this light.

The imaging beam, on the other hand, must have a very uniform intensity profile. As the case before we used a single-mode angle-polished polarization-preserving optical fiber to spatially filter the imaging beam. It is critical to use both angle-polished and polarization-preserving fiber to reduce temporal intensity fluctuations of the beam. The input and output facets of a flat-polished optical fiber can form an etalon, which will produce high-frequency intensity fluctuations on the output. A non-polarization-preserving optical fiber will scramble the input polarization depending on the stress (thermal or mechanical) applied to the fiber. These polarization fluctuations will be converted into intensity fluctuations when the light passes through a polarizer. One good method to align the input light polarization with the axis of the optical fiber is to first adjust the angle of the input linear polarization until pure linear light is emitted from the optical fiber. This procedure may be too coarse to accurately align the axis, so the next step is to tap on the center of the optical fiber, weakly enough not to change the coupling at the ends or

3. APPARATUS AND METHODS

warm it with one's hand, and to watch the transmitted intensity fluctuations on the output after a polarizer. One can now more finely adjust the input polarization until a minimum of polarization fluctuations is observed at the output.

3.6.7 MOT optical setup

From the lasers black box the light beams go to the science cell on the optical table. Figure 3.34 shows the optical setup of this part. A PBS cleans the polarization at the output of the cooling light op. fiber, that is then split into the four beams required for the mirror MOT. Two pair of lenses in a telescope configuration enlarge the beams to use all the chip surface. Finally the beams are circularly polarized by a $\lambda/4$ waveplate. Each beam has an e^{-2} beam diameter of 30 mm and a power of about ~ 70 mW or 10 mW/cm² intensity.

The MOT repumping beam, with the total power of 7 mW after the fiber, is mixed with the cooling light in the first of the splitting PBS cubes. The beam for optical pumping is mixed on a secondary splitting PBS cube, doing like this ones is sure of the direction and polarization of the beam during the optical pumping stage, this it will explained more accurately on the section 2.2.6. The imaging beam path is explained in the section 3.7.

3.7 Extracting the Information from Atoms Clouds

All the information about the atom clouds displayed on this thesis is obtained using the optical properties of the atoms. We use two different techniques to probe the atoms, fluorescence and absorption imaging and two kinds of sensors, the photo-diode and the charged coupled device, CCD.

In fluorescence imaging, the atoms are illuminated by laser light (usually from the MOT beams), and some of the light scattered by the atoms is collected to form an image or directly focused on a photo-diode or CCD. This technique is particularly useful for imaging atoms in the magneto-optical trap, where the atoms are scattering light continuously. Imaging this scattered light provides a non-destructive measurement of the MOT. By pulsing on some light, fluorescence imaging can also be used to image atoms in a magnetic trap or

3.7 Extracting the Information from Atoms Clouds

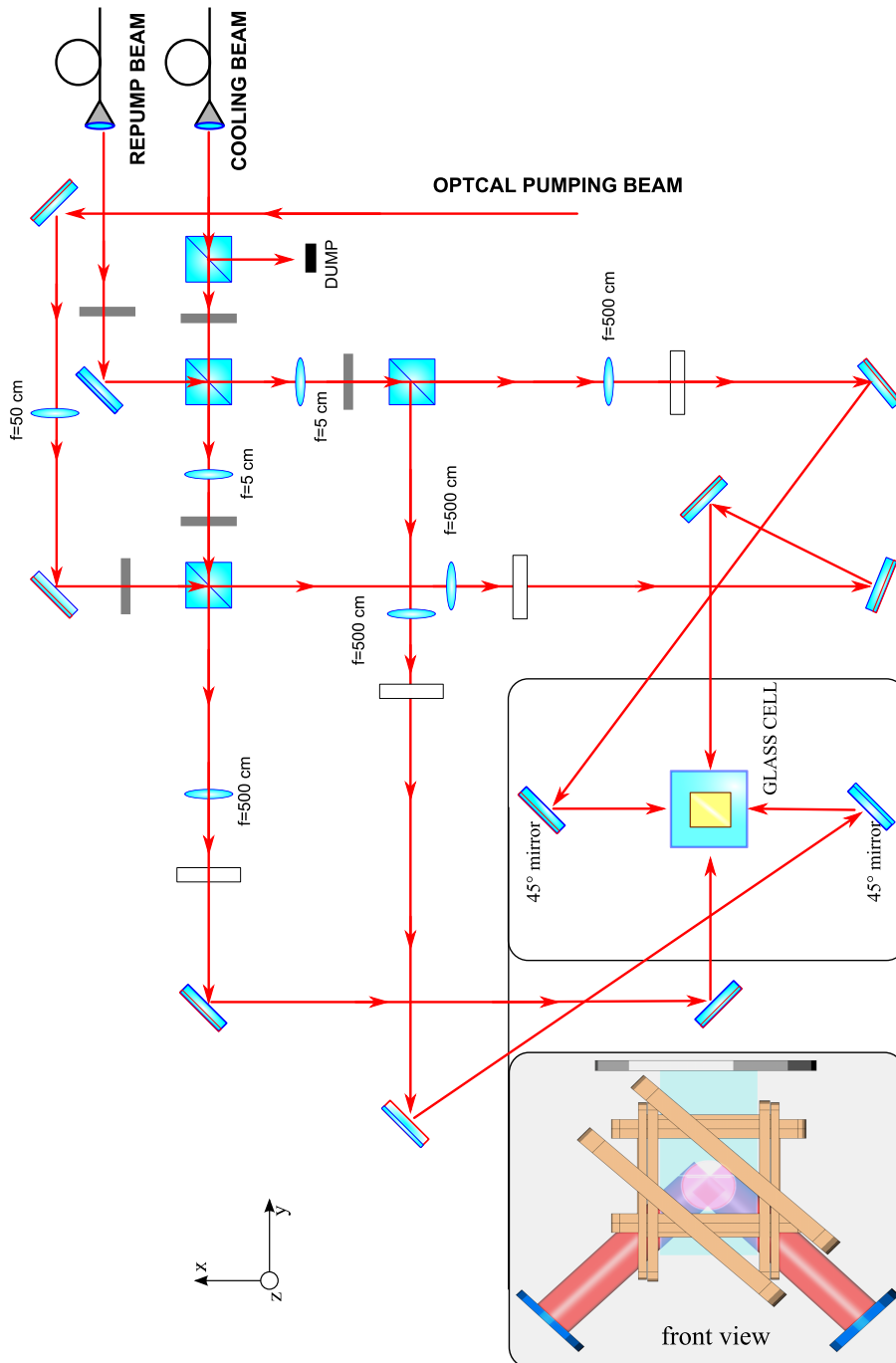


Figure 3.34: The optical setup of the MOT.

3. APPARATUS AND METHODS

during ballistic expansion. Only in this case the imaging process is destructive, as the atoms are accelerated and heated by the probe light.

A superior technique for these clouds is absorption imaging. Here, instead of imaging the light emitted by the atoms, the shadow cast in a probe beam due to the absorption by the atoms is imaged. This technique is also destructive for the same reasons. Its advantage over fluorescence imaging is a higher signal to noise ratio for short light pulses. The solid angle for light collection by the imaging system is small ($\ll 4\pi$) and therefore in fluorescence imaging, only a small fraction of the light scattered by the atoms is collected. This fact gives absorption imaging its strength; the whole of the absorption signal is collected, and as only a small fraction of the rescattered light makes it into the imaging optics, the contrast of the absorption signal is very high.

3.7.1 Fluorescence

We use fluorescence imaging to characterize the cloud in the first steps of the MOT regime. Fluorescence is useful for diagnostics of several parameters, such as efficiency of the MOT, temperature, loadings rates and decays. However, it is limited to the diagnostics in which it is not important to measure the absolute temperature and number of atoms in the trap but rather relative quantities for the purposes of comparison. We use fluorescence imaging because, although it has less absolute accuracy than absorption imaging, it is easy to set up and gives us the information we require, without destroying the MOT, meaning that quick measurements can be performed. The fluorescence imaging was particularly useful during the calibration for control the rubidium pressure during the MOT loading, dispenser or LEDs, to monitoring *in-vivo* the numbers of atoms in different regimes of the vacuum system.

The number of atoms in the MOT is related to the atom fluorescence by the the photon scattering rate R given by

$$R = \frac{\frac{I_0}{I_s} \pi \Gamma}{1 + \frac{I_0}{I_s} + 4\left(\frac{\Delta}{\Gamma}\right)^2}, \quad (3.4)$$

where R it is the rate of emitted photons/atom/sec, I_0 is the total intensity of the beam impinging on the atoms, I_s is the saturation intensity, Γ is the natural linewidth of 6 MHz for Rb, and Δ is the detuning from resonance. If

we collect this scattered light on a photodiode we have the number of atoms N related to the photodiode signal S

$$N = \frac{4\pi S}{d\Omega A \hbar \omega RL}, \quad (3.5)$$

where L is the transmission fraction of the optics, A the photodiode responsivity and $d\Omega$ the solid angle captured by the lens. The fluorescence is collected by a lens of $D = 42 \text{ mm}$ and nominal focal length of $f = 10 \text{ mm}$. We mount the lens approximately at $2f = 20 \text{ mm}$ from the cloud and the photodiode on a micrometer stage at $2f$ from the lens.

In these measurements there are two sources of uncertainty. The first is the uncertainty in the solid angle. This can be difficult to calculate as the solid angle can be limited by objects like the edge of the chip whose exact location is hard to measure. The second factor is the uncertainty in the scattering rate. This arises because in the MOT, the saturation intensity is not well defined. The atoms are scattering on many different transitions, with different amplitudes. Some authors use saturation intensity averaged over all the transitions, some the saturation intensity for the stretched state transition only. The saturation intensity in a MOT is 4.1 mW/cm^2 for random polarization for Rb. It should be noted that both these factors will only affect the absolute atom number.

3.7.2 Absorption imaging

The great part of the measurements were made by a absorption imaging technique. A flash of resonant light is sent to the atoms, they scatter photons out of the beam, and we focus the shadow cast by the atoms onto a CCD array. The amount of light absorbed gives the column optical density (OD) along a particular ray through cloud. Optical density is defined by Beer's law and is given by

$$I_t = I_0 e^{-OD}, \quad (3.6)$$

where I_0 and I_t are the intensities entering and emerging from the atom cloud, respectively.

After we acquire our data image, we take two additional pictures for nor-

3. APPARATUS AND METHODS

malization purposes. This three photos should be taken sequentially, with the time between them as short as possible in order to improve, this sequence is explained in detail in section 3.7.6. The final image gives us the full information about the cloud, like position, dimensions and density. In essence, everything that is experimentally known about the atomic cloud in this thesis has come from the analysis of images of optical density structures.

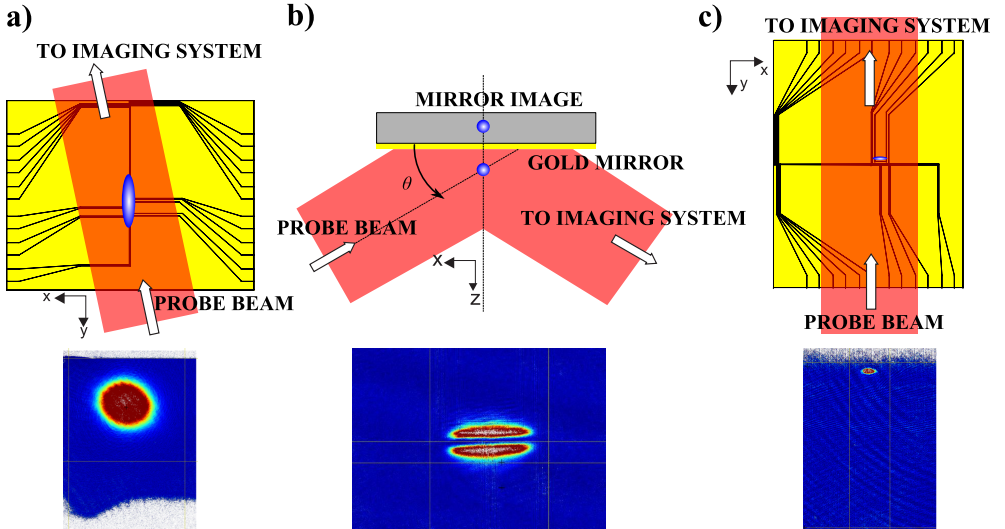


Figure 3.35: The layout of the three probe beams for testing the atom cloud with its results below. a) The TOF imaging: in this case the pulsed is sent quasi parallel to the one of the MOT horizontal beam. Is used to measure of the cloud when is far from the atom chip surface, MOT, Molasses are checked by this layout. b) The reflection imaging: the light is directed towards the chip, perpendicular to the radial symmetry of the cloud. Due to the reflection from the mirror chip we see two symmetrical clouds and from the distance between them and the angle of the beam with the surface we can recover the real distance to the chip surface. c) Direct imaging: In this case the beam is horizontal to chip surface and is perpendicular to the axial shape of the cloud. It is used with a larger magnification and a sensible CCD to imaging the condensed atoms.

3.7.3 Optical setup

Using imaging beam that we described in section 3.6, after the AOM the polarization of the beam is set with a polarizing beam splitter cube. The beam is then spatially filtered using a polarization-maintaining fiber. The diverging gaussian beam is collimated to a $7.14 \text{ mm } 1/e^2$ diameter with a Thorlabs fixed

fiber collimator (F810FC-780), the large spot size ensuring even homogeneous illumination across the atom cloud. The light is made circularly polarized after passing through a $\lambda/4$ -plate and sent to a flipper mirror mount in order to select the directions of the imaging beam. One direction: here the beam is parallel to the chip surface, is used when a long ballistic expansion is needed, specially, for temperature measures (see a) in figure 3.35) with the probe beam parallel to the chip surface. The second one is used when the atoms are close to the surface, at the distances of less than $700 \mu\text{m}$ from the surface (see b) in Fig.3.35). A third path is used for imaging the atoms perpendicular to the axial direction of the chip traps, this one is used for imaging the condensate, see c) in figure 3.35.

For the collecting optics we use two schemes. In one we make the image of the atoms with only one lens (see figure 3.36), it is a rough solution but is simple and economic. We chose this configuration for the direct imaging, used only for testing the cloud during the early stages of the apparatus set-up where no quality image is needed.

In the second case the image is formed by a high-quality lens, near infrared achromatic doublet. We use a confocal telescope configuration where two lenses have been displaced in the following way: calling f_1 and f_2 the focal lengths of the two lenses, we put the first lens at a distance f_1 from the object, and the CCD sensor at a distance f_2 from the second lens. The distance between the two lenses is not important. The magnification M obtained is $M = f_2/f_1$. Since we sought the possibility of having two different magnifications available, we have used two combinations of lenses, following the scheme presented in figure 3.36. The first combination, with $M = 1$, uses two equal lenses (with $f_1 = f_2 = 150 \text{ mm}$); in the second combination the first lens is unchanged and the second is substituted with a $f_2 = 750 \text{ mm}$ doublet, so that $M = 5$. As shown in the figure, distances between the lenses can be chosen so that, without moving the CCD camera, it is possible to switch between the two magnifications simply by changing the second lens.

We focus the image onto the CCD camera by imaging a small (few times our resolution limit), low OD cloud that has not expanded much, that give us the sensibility to find a good position of the lenses. But before we focus the image we first take a line shape to ensure we are on resonance (see figure 3.37). Above and below the optical resonance frequency the real part of the index of

3. APPARATUS AND METHODS

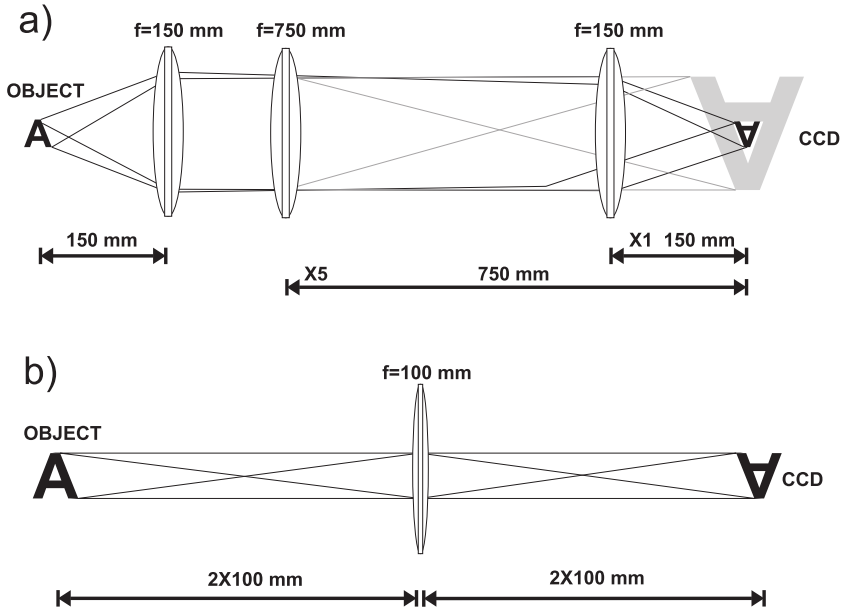


Figure 3.36: Schematic of the imaging system. a) The double magnification setup tested for our imaging apparatus. The first lens is fixed, and is positioned at a distance from the object equal to its focal length. By placing the lens second or third we obtain a different magnification factor ($X5$ or $X1$, respectively). The image is reproduced on the CCD plane, whose position does not change. b) The simple imaging configuration with one lens, the lens is disposed at $2f$ from the object and the image forms too at $2f$.

refraction of a gas differs from one, and the ellipsoidal cloud of gas will not only absorb light but also refract or "lens" it. Once we have tuned the probe laser to the resonant frequency of the atomic transition, we adjust the position of the camera along imaging axis with a micrometer stage that is firmly bolted directly to the optical bench to reduce vibrations. The focus of the image will be at the minimum cloud width. We focus the image by measuring the width in the radial direction.

3.7.4 Resolution

A theoretical resolution limit for imaging with a lens can be given by the Rayleigh criterion: two point sources are resolved if the center of the Airy disc of one overlaps with first dark ring of the other. The minimum distance that can be resolved is given by: $d_{min} = 4.122 \lambda f/d$, where λ is the wavelength of

the light, f is the focal length and d the diameter of the lens. The numerical aperture NA and its inverse, the F-number, are given by $1/F = NA = f/d$. In our setup, the first lens has an F-number of 2.95 resulting in a resolution limit $d_{min} = 3 \mu m$.

3.7.5 CCD Camera

We have three CCD cameras. One is from THETA SYSTEM, model SIS1-t258EM, equipped with a Texas monochromatic interline sensor, TC285SPD. Its dimensions are 1004×1002 pixels; each pixel has a linear dimension of $8 \mu m$, and the analog to digital conversion can be performed by the on-board electronic at 14 bit with a frame rate of 10 Hz and a quantum efficiency of 40 % at 780 nm. The other two cameras are from Sony (models XCD-SX710) and are equipped with Sony ICX-204AL monochromatic interline sensors, the pixel size is smaller $6.45 \mu m$. These have less good performance than the THETA camera, since the sensor dimension is 1024×768 pixels and the digitization is done at 8 bit. They are nevertheless much more versatile and faster, and can be used to image the MOT as well as the magnetically trapped atoms without any problem. For the imaging on the Bose-Einstein condensate, on the contrary, is used the THETA camera, since it provides a better sensitivity and a larger intensity dynamic range. The THETA camera is connected to a computer by an serial plus USB port; the Sony cameras use a high-speed Firewire connection (IEEE 1394). Both solutions ensure a fast data transfer and versatile device management.

For each model we have developed a Python program that not only controls the main settings of the device, such as digitization depth, subframe coordinates, exposure time and triggering options, but also acquires the images, displays them it on the PC monitor, and processes them in order to extract the relevant information about the imaged sample.

3.7.6 Absorption imaging procedure

The absorption imaging sequence starts by switching off all MOT lights and magnetic fields. We let the cloud expand and fall free for some ms, the exact expansion time depending on experiment, this time is called TOF, time of flight. After we probe our atomic samples with a σ^+ polarized light resonant

3. APPARATUS AND METHODS

with the closed transition $|F = 2, M_F = 2\rangle \rightarrow |F' = 3, M_{F'} = 3\rangle$, in order to ensure a strong absorption process and thus a large signal-to-noise ratio. While a weak homogeneous magnetic field of some Gauss it is pulsed in the direction of the imaging beam, for defining the quantization axis. The choice of this imaging frequency prevents us from revealing the atomic population that, after the molasses phase, could fall into the $|F = 1, M_F = -1\rangle$ state. We avoid to make the imaging with the confining magnetic fields on. This can be done but requires a different treatment for procedure and analysis due to the quantization axis defined by non-uniform magnetic field, but it is useful to find the exact position of a trapped cloud.

The imaging beam intensity is about 1 mW/cm^2 and can be switched on and off by the corresponding AOM in a very short time ($25 \mu\text{s}$). We use a short pulse for one reason. If the atoms in the cloud scatter too many photons they will pick up enough momentum to move along the direction of the probe beam; this motion could blur the image or cause the atoms' transition frequency to change as they move into regions of larger magnetic field.

With the exposure time $\tau = 25 \mu\text{s}$ we find from equation (3.4) $N_{scat} \simeq 100$ for the number of scattered photons at resonance. During illumination atoms are displaced by the recoil of the scattered photons. We can estimate the root mean square displacement transverse to the line of sight by $v_{rec}\tau\sqrt{N_{scat}/3}$. Inserting the recoil velocity of $v_{rec} = 5.9 \text{ mm/s}$ we find that 100 recoils give a displacement of $\sim 1 \mu\text{m}$. This displacement is below the optical resolution limit of $3 \mu\text{m}$ (see 3.7.4) and of the order of the effective pixel size in the object plane in the worst case, i.e. for the biggest magnification $M = 5$, $6.45/Mag = 1.29 \mu\text{m}$).

To understand the information that comes from the CCD we start writing the equation relating the digitized value V of a pixel to the light intensity incident on that pixel during the exposure. In order to do so we define the sensor quantum efficiency Q as the average number of electrons produced in the CCD cell by one photon. Obviously $Q < 1$ in the case of THETA camera we have $Q \sim 0.4$ at $\lambda = 780 \text{ nm}$. From device specifications we know the typical linear full well depth D of each pixel, that is the maximum number of electrons that a unit cell of the sensor can hold; in our case $D = 40000$. Finally, we can also measure the digitized output value corresponding to a saturated pixel, V_s . Typically V_s is much smaller than the full scale value of the digitization

3.7 Extracting the Information from Atoms Clouds

range (in the case of 14 bit, it would be 16384), in order to permit binning of multiple pixels. For a given exposure time T_{exp} , the light intensity incident on the pixel is

$$I_{i,j} = h\nu \frac{VD}{V_s Q T_{exp}}, \quad (3.7)$$

where ν is the frequency of the incident light and i, j identifies the pixel in the $n \times m$ sensor array. Now we use the Beer-Lambert's law in differential form

$$dI = -\sigma n(x)I dx. \quad (3.8)$$

Here I is the incident beam intensity, dI its variation during the transit dx through the sample, n the numerical density of atoms and $\sigma = 3\lambda^2/2\pi$ the resonant absorption cross section. Integrating along the complete optical path through the medium, and calling I_0 and I_t the incident and transmitted intensities respectively, we obtain

$$I_t = I_0 e^{-\sigma \int n(x) dx}. \quad (3.9)$$

In an image the real object is averaged out along the direction of observation (\hat{x}) and, from the previous equation, we can extract information on the column atom density

$$\tilde{n}(y, z) = \int n(x, y, z) dx = -\frac{1}{\sigma} \ln \left(\frac{I_t(y, z)}{I_0(y, z)} \right). \quad (3.10)$$

As already stated, the information on density depends only on the physical quantity σ and the ratio between intensities. This suggests to take two images: one with the sample of atoms, containing the information on absorption ($I_t(y, z)$), and the other without atoms, containing information of incident light ($I_0(y, z)$). In order to avoid offset errors, it is also useful to take a "dark" image, that is an image without atoms no imaging beam, that takes into account all the effects due to spurious light sources (we will call it $I_d(y, z)$). The final column density is given by

$$\tilde{n}(y, z) = -\frac{1}{\sigma} \ln \left(\frac{I_t - I_d}{I_0 - I_d} \right). \quad (3.11)$$

This equation has to be corrected by the area A of a single CCD pixel and

3. APPARATUS AND METHODS

by the magnification M , in order to give the number of atoms corresponding to each pixel indexed as i, j

$$\tilde{n}_{i,j} = -\frac{A}{\sigma M^2} \ln \left(\frac{I_t - I_d}{I_0 - I_d} \right). \quad (3.12)$$

Summing this quantity over all pixels gives the total number of atoms. The program that we have developed is able to extract this information from the image, once the user has manually delimited the region that contains the absorption spot. It can also perform fits on the intensity profiles, permitting to determine in a precise way the position of the sample in the frame reference of the image.

Absorption imaging permits to extract the important information even without knowing the full specifications of the CCD sensor. In fact, as we will see, relative-quantities measurements can be done, thus excluding the influence of the sensor features.

3.7.7 Imaging Spectrum

We confirm that we are on resonance by recording a transition line shape, which involves producing a series of identical clouds and probing them with different frequencies. We change the frequency of the first probe and measure the peak optical depth. The resulting curve should be a Lorentzian with the natural linewidth Γ .

Figure 3.37 shows a curve (circles) representing the optical density of the cloud as a function of the imaging beam detuning from the frequency of the $|F = 2\rangle \rightarrow |F' = 3\rangle$ transition. As we expected, the optical density is proportional to the absorption probability, and thus follows the Lorentzian profile of the transition. The FWHM of the recorded profiles fitted with a Lorentzian function is $W = 8.0 \pm 0.6$ MHz. If we add an external magnetic field along the direction of the imaging beam (circularly polarized), we can notice a frequency shift of the absorption profile, due to the different Zeeman shifts of M_F sublevels involved in the transition (figure 3.37, squares). In this case the fitted curve gives $W = 9.0 \pm 0.7$ MHz and a frequency shift of 2 MHz. We also observe an increment in OD which is due to the increment in the

absorption of atoms that are now polarized in the direction of the imaging beam.

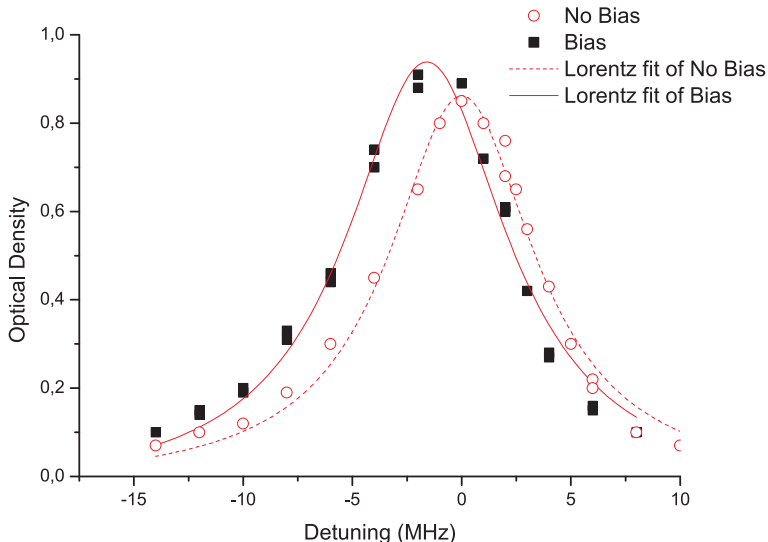


Figure 3.37: Transition line shape of our imaging beam. We take different absorption images changing the frequency of the probe. The plotted optical density has a typical Lorentzian profile. Here we show the two profiles, empty red circles correspond to the imaging procedure without the bias field and black squares to the imaging with the bias field on. The shift in the central frequency is due to the Zeeman shift, and the raise in the maximum OD means that the coupling between light and atom is better when a uniform magnetic field is pulsed on. The lines are the results of fitting with a Lorentzian function.

With the imaging beam circularly polarized, during imaging the atomic population will be rapidly driven to the closed cyclic transitions $|F = 2, M_F = 2\rangle \rightarrow |F = 3, M_F = 3\rangle$ (for σ^+ polarization), and $|F = 2, M_F = 2\rangle \rightarrow |F = 3; M_F = 1\rangle$ (for σ_- polarization). Recalling equation 2.17, the Zeeman energy shift of the lower levels is $\Delta E^l = \pm\mu_B B_z$ (since $M_F = \pm 2$ and $g_F = 1/2$), while that of the upper levels is $\Delta E^u = \pm 2\mu_B B_z$ (since $M_F = \pm 3$ and $g_F = 3/2$). This shift in the levels yields a frequency shift in the probe beam of $\Delta\nu_{\pm} = \pm \frac{\mu_B B_z}{\hbar}$.

As we said before in the reflection imaging we can see two clouds, one is the shadow cast by the atoms directly flashed by the probe beam, the other one is the shadow cast by the atoms due to the probe beam reflected. If we set the probe beam with circular polarization, the reflection on the gold mirror of

3. APPARATUS AND METHODS

the chip changes the polarization of the beam for 180° . So we can distinguish between the two absorptions, but only with the bias field on. As we have seen, if no magnetic field is present, the two absorption profiles have equal intensities. On the contrary, the introduction of an external field component can break the symmetry and enhance the absorption of one polarization component at the expense of the other. This effect is evident in the sequence shown in figure 3.38. In presence of the external field, we can play with the polarization of the imaging beam in order to make one absorption spot brighter than the other and vice-versa.

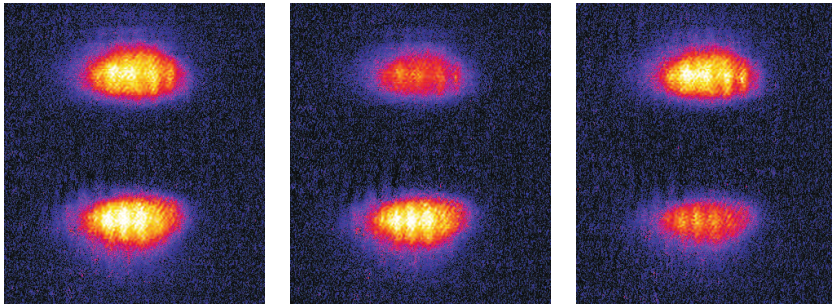


Figure 3.38: In these three images we can see the effects of the polarization of the probe beam. In the first image (starting from the left) we give a random polarization to then imaging beam, here both clouds are equal in intensity. The next two images are refer to opposite and circular polarizations, we can increase the absorption due to the reflection on to the gold mirror or not, before arrives to the cloud.

The line shape can also be a useful probe for the laser frequency noise. Often the probe laser frequency can be affected by shutter-induced vibrations or current transients right before imaging. Therefore it is important to measure the noise on the laser during the imaging pulse. One can find the shot-to-shot standard deviation of the measured atom number while the probe is tuned on resonance and while the probe beam is half linewidth off resonance. Comparing the two measurements rejects uncorrelated atom number fluctuations. A significant increase in shot-to-shot noise when the laser is tuned a half linewidth off resonance indicates a probe laser frequency or magnetic field noise.

3.7.8 Magnification

We determine the magnification of our imaging system by watching a cloud fall under the influence of gravity (see figure 3.39). We turn off all the magnetic fields and laser light, with all the fields off, the center of mass of not only a MOT but of any cloud falls. Of course we turn off all the fields but leaving on the compensation coils in order to remove the spurious magnetic fields. The only active force over the atoms is the gravity and the vertical position of the center of the cloud must follow the expression

$$z(t) = M(z(0) - a/2t^2), \quad (3.13)$$

where a is the acceleration due to gravity in m/s^2 , $z(0)$ the cloud's initial position in m, and M is the magnification factor. Fitting the falling of the cloud with a gravity as constant we can set accurately the magnification factor. An initial velocity factor can be added to check if during the release of trap the cloud was pushed. If we chose the reflection imaging, we must include an easy-to-measure angle factor.

We can raise some objections, how we are sure that we eliminate all the spurious field, or how we are sure that there is not any initial velocity of the atoms. During the optimization of molasses we set the compensation coils for the minimum temperature, which means that we cancel all the spurious magnetic fields. All magnetic fields and laser lights were turned off fast enough (less than ms) and synchronized, during these tests.

3.7.9 Image Fitting

We use three different fitting routines depending on the degeneracy of the cloud. For clouds above the condensation temperature we fit the image to a 2-D Gaussian. Clouds at finite temperature but with a condensate present are fitted with two separate functions. The condensate portion of the image can be fit to a Thomas-Fermi profile, which is a paraboloid integrated along the line of sight. The thermal cloud is no longer an ordinary Gaussian when it is degenerate but is modified by Bose statistics and must be fitted with the appropriate function.

3. APPARATUS AND METHODS

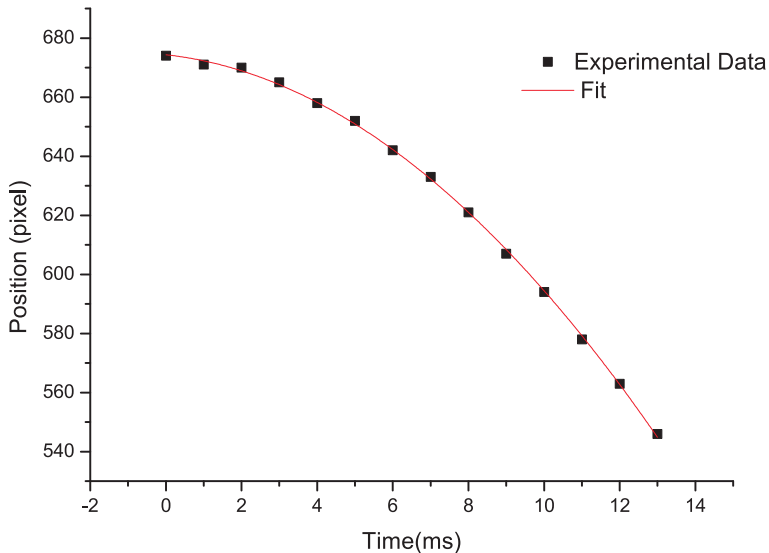


Figure 3.39: The position of the cloud center of mass is falling into gravity. We allow the atoms to fall for a varying time and measure their resulting position. The fitting results it is the red line, and give us the magnification of our optical system.

3.7.10 Signal to noise ratio between absorption and fluorescence imaging

Absorption imaging is discussed first. Consider the photons arriving at a single CCD pixel which has an effective area A_{eff} where $A_{eff} = A/M$ given that A is the true pixel size and M is the magnification factor of the imaging system. Now if we have a small number of atoms N localized within a section of area A_{eff} of the probing light with intensity I , the reference signal (in counts) obtained (just the probing light without illuminating the atoms) is given as $S_1 = \eta I A_{eff}$ where $\eta = Q/\hbar\omega$ and Q is the quantum efficiency of the detector. The absorption signal is then given as $S_2 = \eta I A_{eff} e^{-n\sigma l} = \eta I A_{eff} e^{-N\sigma/A_{eff}}$ where σ is the scattering cross-section of the atom. From here, we obtain our useful signal to be $S_1 - S_2 = S_1(1 - e^{-N\sigma/A})$. The noise on absorption is just $\sqrt{S_1}$ and therefore our signal to noise ratio for absorption imaging is $\sqrt{S_1}(1 - e^{-N\sigma/A})$.

For fluorescence imaging, the fluorescence emitted by the atoms is simply related to the amount of light that was absorbed by the atoms during absorption imaging i.e. $S_F = f(S_1 - S_2)$ where f is the fraction of fluorescence light

collected by the collection optics. The noise of this signal is $\sqrt{S_F}$. Therefore, the signal to noise ratio for fluorescence imaging is $\sqrt{f(S_1 - S_2)}$. We have assumed that the magnification and quantum efficiency of the detector is the same in our example for both imaging methods. With the above expressions, the ratio of signal to noise ratio between fluorescence imaging and absorption imaging is

$$\frac{(S/N)_F}{(S/N)_{abs}} = \sqrt{\frac{f}{1 - e^{-N\sigma/A}}}. \quad (3.14)$$

If this ratio is calculated with typical experimental parameters where $N\sigma/A \ll 1$, then it can be approximated as

$$\sqrt{\frac{fA}{N\sigma}}. \quad (3.15)$$

The formula shows that the fluorescence imaging is more suitable for clouds with small number of atoms. However, this is also valid when the other sources of noise are taken into account. For example, imperfections in the CCD and optics may cause the laser beam (with no atoms present) to record a slightly different intensity on each pixel. There will also be fringing effects due to the interference of back reflections off optical components. These imperfections make the absorption background IQ uncertain by a small fraction (a few percent). If only a small number of atoms are imaged by each pixel, the absorption signal will be relatively small (also around a few percent) and this uncertainty in the background will overwhelm the absorption signal. However, for fluorescent imaging these imperfections will show up only as a small percentage of the total fluorescent signal, and so will have far less negative influence on the measurement.

3.8 The remote control electronics and software

As you have seen, the whole lot of synchronized signals are needed to control the whole experiment. The experiment can be actually considered as a sequence of actions completing in a relatively short time, of the order of a milliseconds. One of the properties of Microtraps is that they "shrink" almost all the typical times of a standard BEC experiment by a factor of 10. Therefore, a precise timing capability is even more necessary than in standard experiments.

3. APPARATUS AND METHODS

The core of the control system is a digital input-output board (ViewPoint, model DIO-64), mounted on a personal computer. The board has 64 logical ports, independently configurable as input or output ports. It has FIFO (First In First Out) buffer, in which a preprogrammed sequence of "actions" (the port configurations) can be loaded by the control software. Each action is associated with a time stamp, and is executed when the board clock fits the time stamp. The big advantage of this system is that the timing is based on an internal 20 MHz clock independent from the computer clock: this means that the timing precision of each action is 50 ns, without any dependence on the computer CPU timing. Once the board operation starts the board operation has started, the execution of the programmed sequence is completely autonomous and the computer can be dedicated to other tasks without influencing the board performance.

The 64 input/output ports are divided into 4 banks of 16 bits. Our applications use only 2 of these banks, so that in principle it has many expansion possibilities. One of the two banks used is dedicated to signal data transfer (16 bit data), the other is assigned to addressing function (8 bit addressing, since only half bank is used).

The board is connected by a specific buffer to our electronic modules, which provide the final output control signals for the experiment. Each module has its own 8-bit address. To be more precise the effectively available address bits are 7, so that the maximum number of modules that can be connected to the ViewPoint board is 128.

There are two types of modules: TTL and analog modules. The former readdress the 16-bit data signal to 16 TTL output ports, thus providing 16 switch-type controls each. The latter convert, by means of a Digital-to-Analog Converter (DAC), the 16-bits bus signal into a single -10 to +10 Volts analog signal, tunable in steps of 0.3 mV.

Currently in our experiment we have two TTL and 12 Analog Modules, so that in total we have 32 TTL and 12 Analog signals available for controlling the experiment.

All the electronics have been designed, tested and realized by researchers and technical staff of the European Laboratory of Non-Linear Spectroscopy (LENS). Similar systems are being used to control at least 5 more experiments in the cold atoms, non atom chips, research activity of LENS. We have built

3.8 The remote control electronics and software

the electronic modules specific to our experiment by ourselves.

A lot of work was put into writing the software necessary to program the Viewpoint board and to build and manage a complex sequence of digital and analog actions. Our program is inspired by and based on a preliminary version written for the first applications of the ViewPoint board. Our aim was to realize a very simple and versatile interface suitable for controlling almost all the devices and instrumentations involved in the experiment. To this purpose, the basic functions of the original program as well as their implementations had to be rewritten.

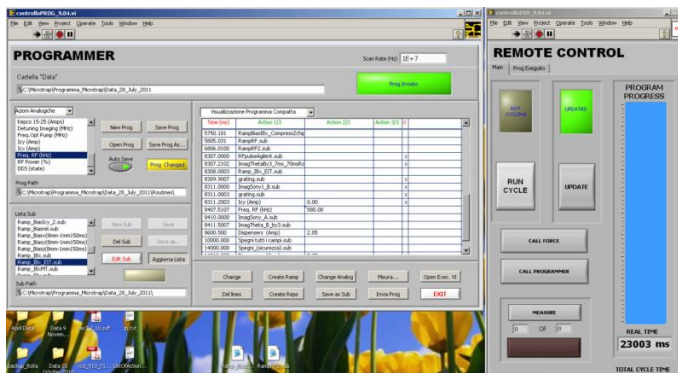


Figure 3.40: The front panel of the Main Controlling Program, from where almost all actions can be controlled and timed, using the pop-up menus like the one appearing in the bottom-left corner.

The work is still in progress, but the program has now an almost definitive structure and can be readily used and adjusted to any experiment involving the use of the ViewPoint board.

The program has been written in Labview graphical programming environment. Its main window is divided into two main parts: the left part contains the lists of all available commands, including TTL, analog and GPIB commands, plus a list of subroutines, that are groups of actions which are possible to refer to by a single *title* name. Each action appears with a label name that makes the identification of the action easy for a user. The program converts it into the format accepted by the ViewPoint board, in order to load the sequence on it. For example, the TTL command "All Shutters ON" corresponds to the switching of all the TTL outputs driving the mechanical shutters on the

3. APPARATUS AND METHODS

cooling, repumping and imaging beams.

By double-clicking on any of these objects (actions or subroutines) it is possible to associate it to a time and insert it in the right table of the main window, thus forming the actions sequence, or program. A program can be composed by an indefinitely big number of actions, and can be executed in *single run* or *cyclic* mode. The timing resolution has been set to $1 \mu\text{s}$, that is well enough for any experimental application involving cold atoms but, as we have already noted, it can be reduced to 50 ns. Each line of the program can be edited, both the *time* and the *data* arguments. For example, the line "1500.000 – AOM Cooling frequency – 59 MHz", corresponds to the analog output connected to the VCO of the oscillator driving the AOM on the cooling beam, and can be modified to change both the time of execution (for example: 1500 ms \rightarrow 2300 ms) than in the argument (for example: 59 MHz \rightarrow 57 MHz). The program continuously monitors the sequence of time dependencies, arranging the actions in the right order. It is possible to delete any program line, or simply to suspend it, so that it is not executed in the final cycle. Finally, it is possible to create equally time-spaced repetitions of an action in the program, and also to create fully customizable ramps for an analog or GPIB parameter.

Finally, it is possible to save any new subroutine or program, and to archive all the data folders in order to track modifications performed day by day. Other secondary upgrades are in progress, but the program is already fully functional and is currently used in our experiment.

4

Reaching BEC

4.1 Overview

The goal of the trapping and cooling sequence is to reach quantum degeneracy with the highest atom number possible. Assuming an elliptical gaussian cloud of a transversal radius r_{ra} and axial radius r_{ax} containing N atoms, the central spacial density can be written

$$n_0 = \frac{N}{\pi^{3/2} r_{ra}^2 r_{ax}}. \quad (4.1)$$

If n_0 is the spacial density of atoms, then we define the atom density in the phase space as a dimensionless quantity

$$\Phi = n_0 \Lambda^3, \quad (4.2)$$

with the thermal de Broglie wavelength Λ given by

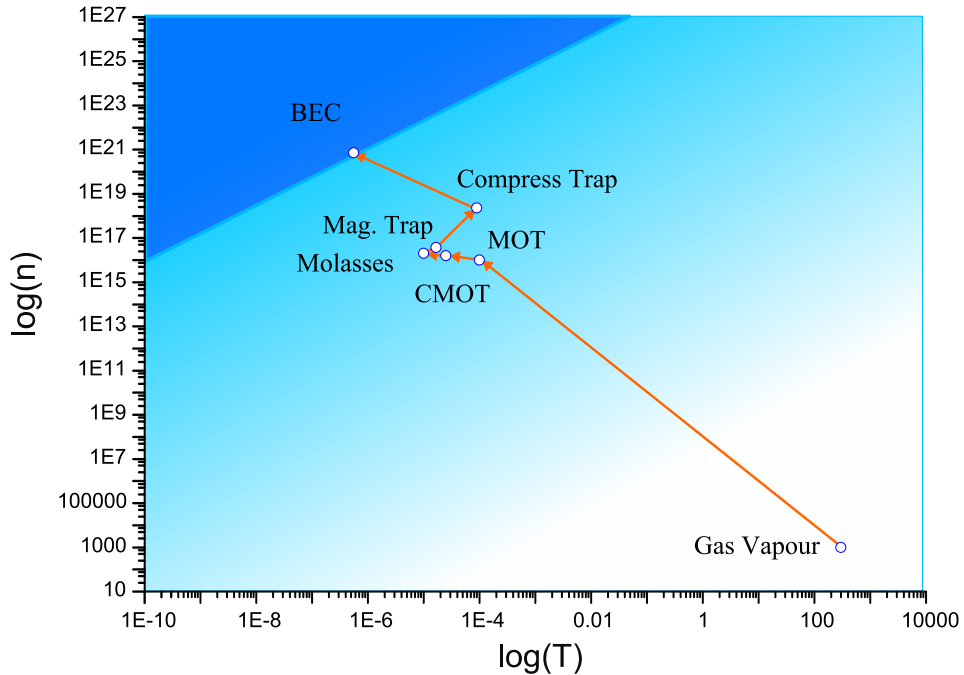
$$\Lambda = \sqrt{\frac{2\pi\hbar^2}{m_{Rb}k_bT}}. \quad (4.3)$$

This can be considered roughly as the number of particles in a box of volume \hbar^3 . For spin-zero particles confined in a box, Bose-Einstein condensation in a three-dimensional ideal Bose gas is reached for $\Phi = 2.612$ (see 2.5).

The successive steps, discussed here, that increase the phase space density of a diluted cloud of atoms and finally lead to Bose condensation are generally

4. REACHING BEC

applied in BEC labs worldwide. Specific to our experimental setup is the use of a millimeter wire bent to get a z-shape to generate the magnetic potentials for the trapping stage.



Stages	MOT	CMOT	Molasses	OP: Pumping	Ztrap	Zchip. trap compression	Ev.Cooling	Vacuum Recover
Duration (ms)	5000	14	3	0.5	250	450	2500	14700

Figure 4.1: A phase space diagram indicating the various stages of the production of our BEC. Table below shows a time line of the BEC production program.

The sequence, see figure 4.1 is based on the background reviewed chapter 2, and adapted to the sequence used in our experiment. The procedure is as follows. The first step is a mirror-MOT stages [6] after which the cloud is compressed and cooled with a CMOT and molasses stage [28]. Subsequently the atoms are optically pumped to a single low-field seeking Zeeman state and trapped in a z-wire magnetic trap. A transfer to the magnetic potential of the on-chip z-wire enables the compression of the trapping volume and hence an increase in the inter-atomic collision rate. At this stage the goal is to get the highest possible value of $\gamma_{el}\tau_{loss}$ in the compressed trap at the beginning of evaporative cooling. From there, the atoms must be evaporatively cooled as

effectively as possible using the radio frequency induced spin flips. Two RF ramp of 2.5 seconds lead to the fast production of a Bose-Einstein condensate of 5×10^4 atoms. Therefore the story of this chapter is really the quest for more atoms at every step along the way.

In this chapter I will discuss in detail how each stage of the path to a BEC outlined above was implemented. To reach the BEC, the performance of each stage needed to be carefully optimized. Therefore the optimization of the experimental parameters at each stage is described in some depth.

The order of the sections reflects the order of the experimental sequence.

4.2 Mirror MOT

The magneto-optical trap (MOT) is the largest compressor of phase space density in this experiment. The hot ($T > 600$ °C) rubidium atoms that escape from the dispenser thermalize by collisions with the walls of the cell at room temperature. Their initial phase space density is $\Phi \simeq 10^{-25}$. At the end of this laser cooling stage the cloud has the phase space density of the order of $\Phi \simeq 10^{-8}$.

4.2.1 Pulsed dispenser

The first task is to load the cell with a rubidium vapor gas, but at the same time one has to be careful not to overload the cell and thus reduce the lifetime of atoms in the magnetic trap, to achieve this the rubidium partial pressure one can use pulsed dispenser dynamic. In a normal vapor cell MOT the rubidium partial pressure is constant, and the loading rate and decay rate are both independent of time. In the case of our pulsed MOT, the rubidium partial pressure in the trapping region is time-dependent and the situation is more complicated.

The dispenser pulse starts at the beginning of the sequence with a 7 A running for 1.7 seconds, after that the current is switched off completely. After another 8.3 seconds the current through the dispenser is set at 2.2 A. This is below the threshold for rubidium production, but keeps the dispenser warm so that it heats up more quickly when pulsed. The system is allowed 13 second of vacuum recovery before the cycle starts again, the total cycle time is 23

4. REACHING BEC

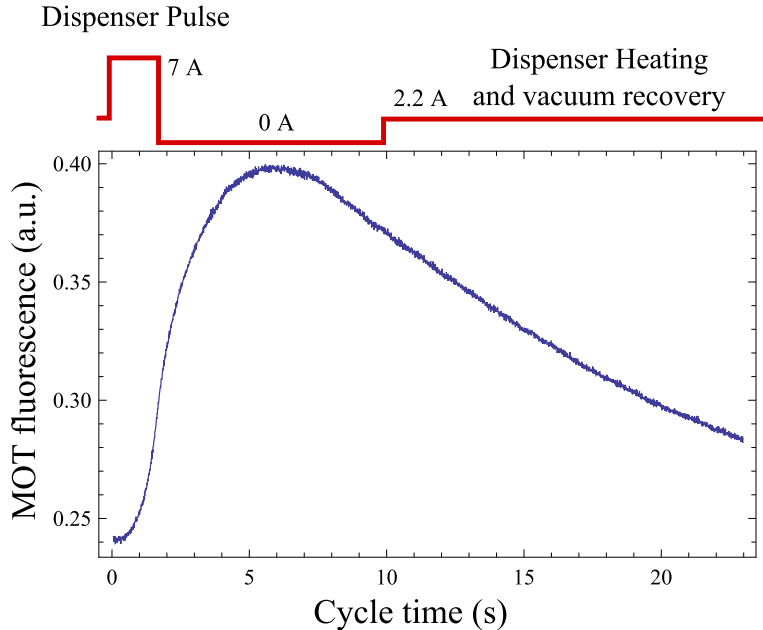


Figure 4.2: Response of the MOT fluorescence in a complete cycle time of a BEC sequence. The pulse of the dispenser current reaches 7 A and starts at 0 seconds with a width of 1.7 of seconds. The total cycle time is 23 seconds.

seconds. Other groups have this vacuum recovery stage just before the magnetic trapping, but they have to use longer pulses on the dispenser. Figure 4.2 shows that atoms are being collected for several seconds after the dispenser is switched off, which means that it takes several seconds for the rubidium pressure in the trapping region to reach to the background level. At long times, the decay of the MOT is exponential and the loss rate is constant. This suggests that the untrapped rubidium background decays away and that the lost atoms cannot be supplemented by collisions with background rubidium. The fundamental limit on this loss rate is set by collisions with non-rubidium background gas. However, as shown in the next section, the lifetime also depends on the parameters of the MOT, and we do not reach this limit. Within 3.2 s the MOT is filled at 2/3 of its maximum, which is reached at 5.5 s, as shown in the figure 4.2. The loading of the MOT from a pulsed Rb source was repeatedly performed with the period of 23 s for many hours without any change in the lifetime and number of atoms in the MOT, at the stable vacuum pressure of about 2×10^{-11} mbar.

4.2.2 Mirror MOT

A mirror MOT [6] configuration is used to load the atoms this technique can provide a large number of pre-cooled atoms in proximity of the chip surface.

The basic concept underlying a mirror-MOT operation is that a circularly polarized laser beam changes helicity upon reflection from a mirror. The 6-beams MOT configuration is replicated by using only 4 beams (see figure 4.3): two are parallel to the mirror, touching it; the other two impinge on the mirror at 45° from opposite directions and lay in the plane perpendicular to the first pair. The quadrupole coils axis is oriented along the direction of the beams of different helicity, i.e. tilted by 45° with respect to the mirror plane. The center of the quadrupole magnetic field has to be situated into the beams overlapping region. In this way usual MOT geometry is realized in the half space delimited by the mirror.

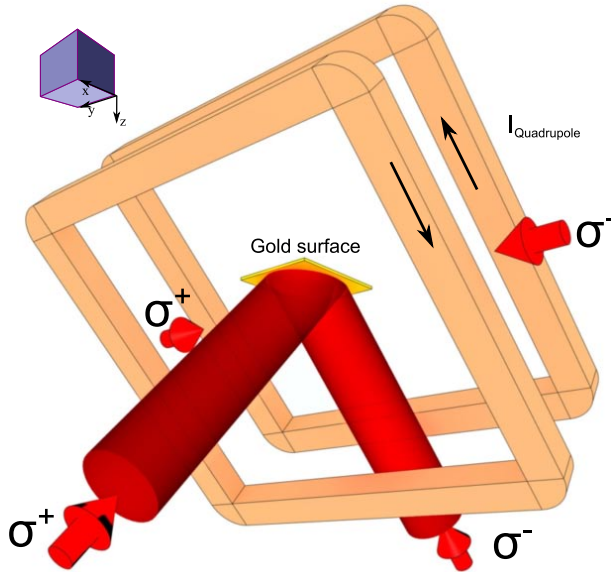


Figure 4.3: Schematic of the mirror-magneto-optical-trap. Cooling light beams in the xz -plane reflect from the chip surface (beams along x are omitted for clarity). σ^+ and σ^- are defined in the propagation direction of the light. The quadrupole coils are shown in light red. Black arrows indicate the current direction.

Indeed, in conventional MOTs the confinement volume can be of several cubic centimeters [17], depending essentially on the laser beam's diameter.

4. REACHING BEC

In a mirror MOT configuration this volume is reduced for several reasons: a practical reason is that the mirror dimensions can limit in some cases the size of the reflecting laser beams; a more fundamental reason is that the MirrorMOT is by definition a half-space MOT. In the strictly geometric configuration, the center of the Mirror-MOT should lay exactly on the mirror, in order to make a perfect light-field symmetry. In this case the effective volume would be reduced of a factor of 2, and the MOT would not work effectively.

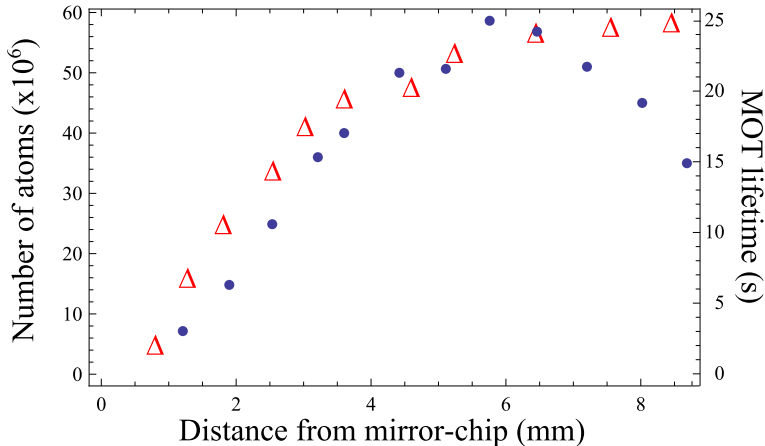


Figure 4.4: The dependence of MOT atom number (blue discs) and lifetime (red triangles) the distance from the chip surface.

Typically, the quadrupole center in the Mirror-MOT is between 1 mm and 7 mm far from the mirror surface, depending of the chip area. This distance is critical to ensure a good number of trapped atoms. The position of the MOT center can be displaced by superposing an appropriate homogeneous magnetic field on the quadrupole field. When the center is located sufficiently far away from the surface the mirror MOT achieves a performance comparable to a standard half-space MOT, but for distances below 1 mm the trap lifetimes decrease, leading to a smaller stationary number of trapped atoms [6]. Results of the measurements performed on this system shows the same trend, see figure 4.4. As magnetic microtraps are effective only in a small range of distances from the chip, typically below 3 mm, keeping the MOT far from the chip surface means that a transfer mechanism has to be realized, in order to bring cold atoms closer to the chip after the MOT phase. The MOT is loaded far from the chip surface, where the atom number is maximum, then shifted and

transferred into a chip trap. The MOT atom number was optimized at different heights to get the best loading point. In figure 4.4 this point lies at 7 mm from the chip.

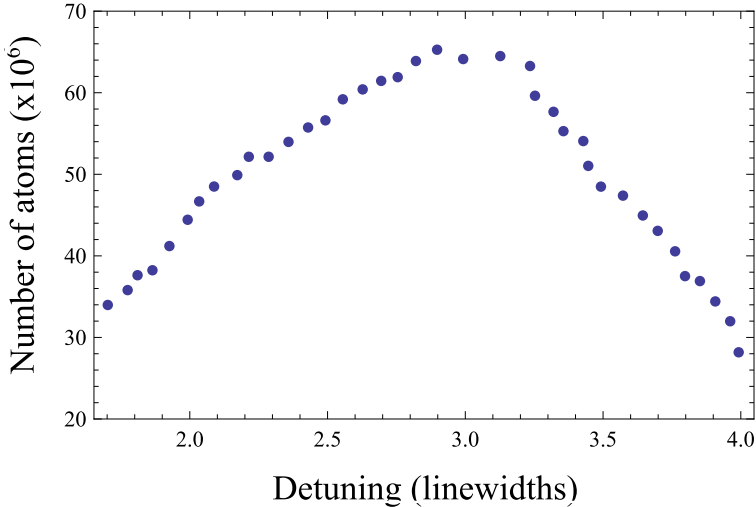


Figure 4.5: MOT atom number versus detuning.

Optimization.

The number of atoms collected in a MOT depends on several parameters. Previous work on 6-beam MOTs has shown that the number of atoms increases with both increasing beam size and power, and that the largest number of atoms is collected at moderate field gradients (15 Gauss/cm) and detunings (3Γ). In our experiment, the maximum useful beam size is fixed by the area of the atom chip.

The dependence of N on trap laser detuning intensity and field gradient is shown in figures 4.5, 4.7 and 4.6 respectively. These are in good agreement with results for six beam MOTs already presented in the literature [77]. The peak atom number is obtained with the detuning of -3Γ (-18 MHz) and the field gradient of 15 Gauss/cm, therefore the MOT is normally operated with these parameters.

No saturation is observed on the atom number with the intensity, suggesting that not enough power is used or the beams are too big. Since the power of the

4. REACHING BEC

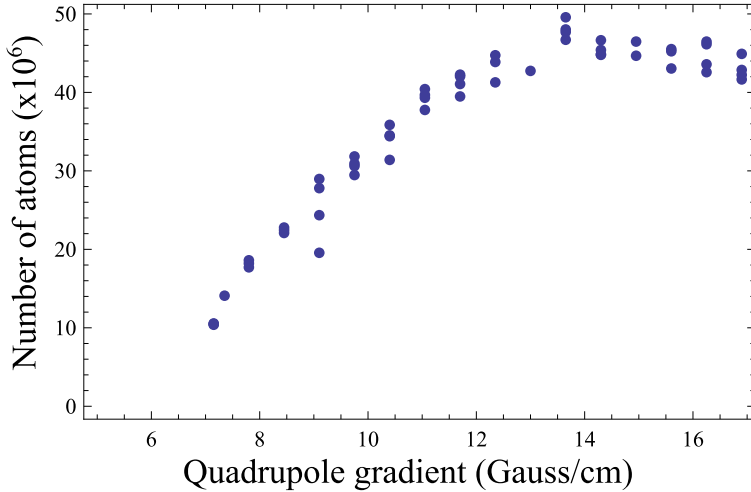


Figure 4.6: MOT atom number versus quadrupole gradient. During the measurements the detuning and the intensity were set to their optimum values.

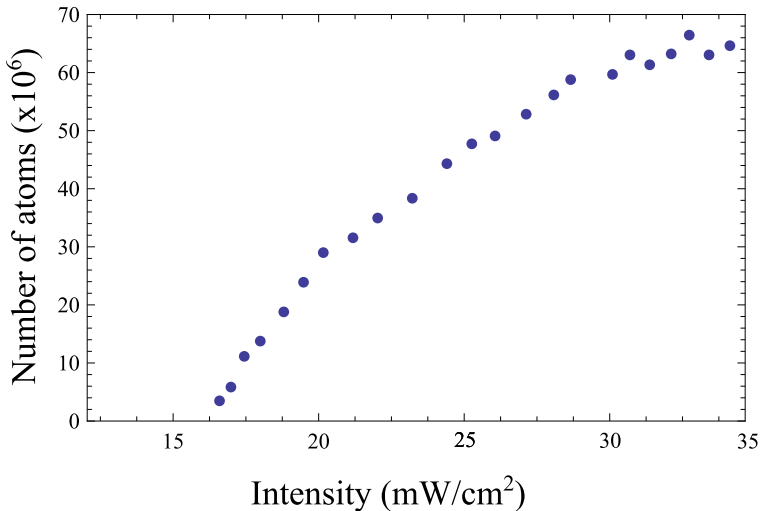


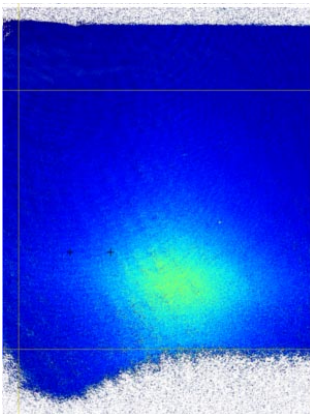
Figure 4.7: MOT atom number versus trap laser intensity. The detuning here was 18 MHz (-3Γ).

laser is at maximum the reduction of the beam diameter could be a solution. Indeed the measures of the beam waist at the output of the optical fiber give us a diameter of 3.2 mm. The telescope after the fiber enlarge the beam by a factor 10, thus the final beam diameter is 32 mm. The chip surface limits the capture area to 21 mm \times 30 mm, see Section 3.3. The asymmetry comes

from the 45° reflecting beams, indeed $21 \times \sqrt{2} \simeq 30$. This surface limits us to a beam diameter of 21 mm. A change in the telescope of the MOT beams can be the way to reach saturation. Now the beam has the maximum intensity of 35 mW/cm^{-2} .

The number of atoms and the lifetime are quite sensitive to the alignment of the MOT beams. Empirically we find that perfect overlap and alignment do not always give us the optimum conditions for the MOT. This is partly due to interference fringes in the light field, reflections from the science cell internal and external windows generates this optical interference. A science cell with a reflection coating will prevent this feature.

To make the MOT, the trapping and repumper lasers are locked to the correct frequencies and the shutters are opened. The MOT coils are switched on and a pulse of current is send to the dispenser. After 5 seconds of loading the MOT, we can collect 7×10^7 atoms at $120 \mu\text{K}$ at 7 mm above the chip surface. This MOT is clearly visible by the naked eye. At this point, the MOT has to be moved closer to chip to be compressed before the loading to the magnetic trap.



MOT

Number of atoms N . 7×10^7
 Radial size y (μm) .**800**
 Axial size z (μm) .**1200**
 Peak density n_0 (m^{-3}) . **1.0×10^{16}**
 Temperature T (μK) .**120**
 Phase space density PSD **8.5×10^{-8}**

Figure 4.8: An absorption image of a typical mirror MOT of the experiment. The image was taken after 15 ms of free falling and expansion. At the top of the image we can see the shape of the chip surface.

4.3 CMOT and Molasses

Once the MOT is full, as many of the atoms as possible must be transferred to the magnetic trap. The goal is to load the atoms into the trap with the largest possible phase space density. When the atoms are caught in the magnetic trap, most of the resultant energy of the atoms comes from the added potential energy due to the Zeeman energy from the magnetic field. The larger potential energy gained by the atoms is when the magnetic trap is turned on. The magnetic trap cannot be adiabatically ramped from zero gradient, because at low magnetic gradients the trap center is significantly offset from the cloud center due to gravity. The center offset induces a sloshing motion in the trap, which turns into thermal energy. Therefore, the reduction in the initial spatial extent of our MOT cloud is important for an optimum loading of the magnetic trap. That is the goal of the CMOT stage. The loading can be further improved by lowering the temperature in a short molasses stage to boost the starting phase space density in the magnetic trap.

The first thing is to transfer the atoms from 7 mm of height above the chip to the height where the magnetic trap will be switched on. In terms of temperature and number of atoms it is better to perform the CMOT and Molasses stages where the trap will be turned on. If one do the opposite the movement heats the cloud, making the previous work of the CMOT and molasses useless. One cannot make a the magnetic trap at any height since it is basically limited by the maximum current that can be sent to the wire. Here, a driver source with 25 Amps max current is used. For the moment lets assume that the minimum trap gradients and trap depth, with 25 amps through the wire, are produced at around 2 millimeters above the chip surface. The field gradients and potential depth necessary to create a good trap are described together with the magnetic trap stage in section 2.3.

The position of the MOT center can be displaced by superposing an appropriate homogeneous magnetic field. With the bias $-z$ and $-x$ fields one can move the center of the quadrupole millimeters without any significant degrading. This step is delicate because the cloud has to be exactly where the center of the magnetic trap will appear. Perfect matching in position is necessary not to have heating or sloshing during the magnetic trapping. To have a reference point the structures of the chip are used. With reflection imaging it is possible

to see the structures of the chip and the cloud together, see figure 4.9.

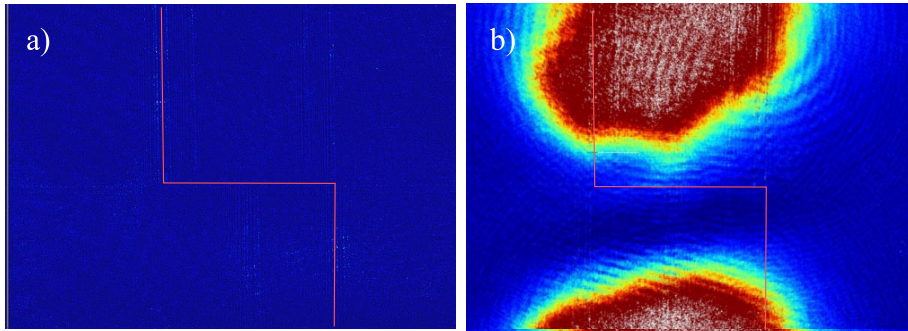


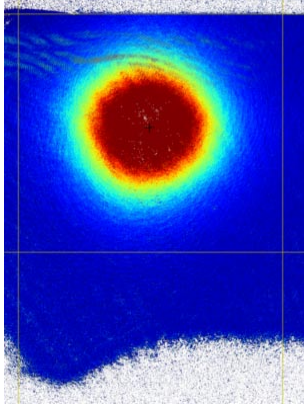
Figure 4.9: (b) Absorption image of the cloud using the reflection imaging at the end of the two ramps. The structures of the chip are visible from this imaging (a), and it can be used like reference for matching the position of the MOT with the magnetic trap.

At the end of the MOT stage two ramps of 450 ms applied the coils x and z bring the atoms to around 2 mm above the chip surface. After the movement of the cloud one proceeds with the cooling and compression stages. The CMOT step consists of a normal MOT with increased red detuning of the trapping laser, decreased power of the cooling light and greatly reduced repump laser power. MOTs with large numbers of atoms have a maximum density of around 10^{10} atoms/cm³, which ultimately is limited by the re-radiation pressure. The CMOT has the effect of reducing radiation pressure in the trap and thus creating a denser cloud of atoms. Reducing the repump power reduces the time the atoms spend in the state ($F = 2$) resonant with the trapping light. Increasing the detuning of the trapping laser decreases the scattering rate and thus the absorption of re-radiated photons. The CMOT stage not only reduces the overall spatial extent of the atoms in the MOT, it also cleans up much of the irregular shape.

We use a short CMOT stage in preparation for transfer to the magnetic trap. The CMOT has a much smaller loading rate than a regular MOT. Therefore we want to minimize the time spent in the CMOT stage before the magnetic trap is turned on. The repump power is reduced from several mW to $50 \mu\text{W}$ for the CMOT stage. Simultaneously with the repump power decrease, we jump the detuning of the trapping laser to 14Γ red of resonance and reduce its power by 80%. The frequency jump is accomplished by moving the

4. REACHING BEC

locking point in the FM spectroscopy, see section 3.6. We keep the magnetic field gradient constant at the MOT value during the CMOT stage. The entire CMOT stage lasts about 14 ms, during which the temperature is reduced to $25 \mu\text{K}$ and the peak density increased to $1.6 \times 10^{16} \text{ m}^{-3}$, see figure 4.10.



CMOT

Number of atoms N . 7×10^7
Radial size y (μm) .700
Axial size z (μm) .800
Peak density n_0 (m^{-3}). 1.6×10^{16}
Temperature T (μK) .25
Phase space density PSD 8.5×10^{-7}

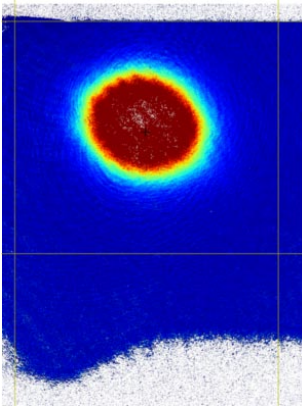
Figure 4.10: Absorption image after the CMOT stage, with properties of the cloud.

At the end of the CMOT stage a short molasses step is performed. During 4 ms the quadrupole field is switched off and the current of the bias coils are changed to the value that compensates the spurious magnetic fields. In the first step of finding the correct fields a free expansion of the cloud is done, the expansion has to be homogeneous in all directions. If one direction of the field is not correctly compensated the cloud tends to move in that direction. In this phase the balance of the beams is important, so it has to be correctly set up too.

The benefits of the molasses are greatest in terms of temperature, at the end of the stage the cloud has a peak density of $2.1 \times 10^{16} \text{ m}^{-3}$ at $10 \mu\text{K}$ and phase space density of $4.5 \times 10^{-6} \text{ m}^{-3}$, see figure 4.11.

4.4 Optical Pumping

At the end of the molasses phase, all the magnetic fields and the trap AOM are switched off. The compressed MOT leaves the atoms in a distribution of



Molasses

Number of atoms N . 7×10^7
 Radial size y (μm). 600
 Axial size z (μm). 800
 Peak density n_0 (m^{-3}). 2.1×10^{16}
 Temperature T (μK). 10
 Phase space density PSD 4.5×10^{-6}

Figure 4.11: Absorption image after the molasses stage, with properties of a cloud.

m_F sublevels. To magnetically trap as many as possible, optical pumping is used to transfer the atoms into the $F = 2$, $m_F = 2$ state.

In this experiment, the atoms are optically pumped into $F = 2$, $m_F = 2$ using the $F = 2 \rightarrow F' = 2$ transition with σ^+ light, for which this state is a dark state. This keeps the heating to a minimum during the optical pumping pulse. The optical pumping light is derived from the reference laser using a double pass through an AOM, as shown in figure 3.26.

After the AOM, the optical pumping beam is mixed with ~ 1 mW of the repumper and expanded to a 2 mm diameter (FWHM) spot to ensure that the atom cloud is evenly illuminated. The intensity of the optical pumping beam is around 1.5 mW/cm². The beam enters the chamber along the same path as one of the horizontal MOT beams, as shown in figure 3.34. The beam paths are overlapped using a polarizing beam splitter cube. A linear polarizer before the beam splitter enhances the polarization purity of the beam, and ensures that all the light leaves through the correct port of the beam splitter cube. The beam is circularly polarized by the MOT quarter-wave plate. The optical pumping beam is σ^+ polarized with respect to a quantization axis in the $-y$ direction, opposite to its propagation direction. This quantization axis is provided by the magnetic field produced by the $-y$ coils.

The optical pumping cycle lasts 300 μs , and begins as soon as the CMOT and molasses stage is switched off. Figure 4.12 illustrates the timing. At the end of the CMOT and molasses phase, all the magnetic fields are switched off.

4. REACHING BEC

The trap light, repumping and cooling, is switched off using the trap AOM and the trap laser shutters. The optical pumping beam shutter opens. At the same time, the y - coils are triggered. The optical pumping light pulse, which lasts $150 \mu\text{s}$, is triggered $100 \mu\text{s}$ later. The beam is pulsed by switching the RF power to the AOM 4, see figure 3.26

Small heating of the atom cloud by the optical pumping pulse was observed; however if too much light is used the cloud could be pushed slightly in the direction of the beam. This suggests that the σ^+ polarization of the light was not perfect and therefore the $F = 2$, $m_F = 2$ state was not entirely dark.

After the optical pumping pulse has finished, the optical pumping and repumper shutters are closed, leaving the atoms in the dark. The guide wire and bias field switch on at the end of the cycle to complete the magnetic trap.

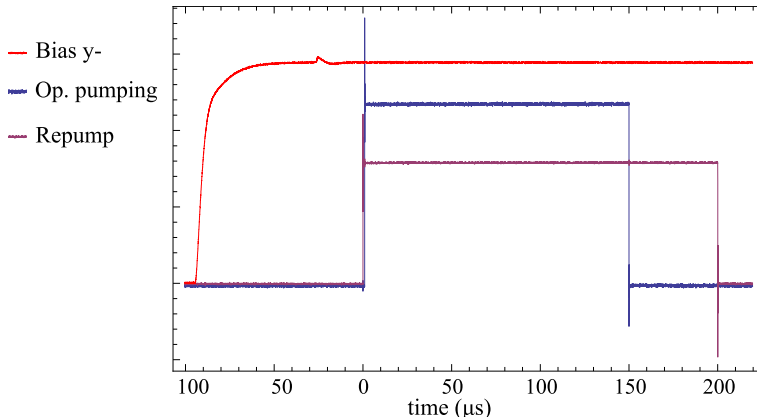
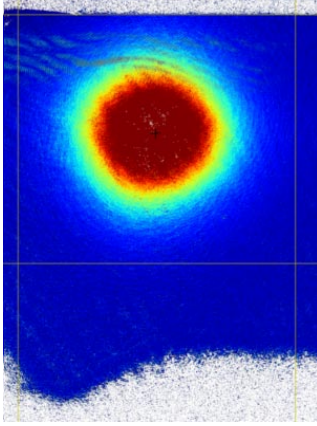


Figure 4.12: The optical pumping sequence. Red trace shows the current through the $-y$ coil, and the signals for the optical pumping and the repumper are shown in blue and magenta respectively.

Using this cooling path one has two advantages; one is that the polarization and alignment are known as they are optimized for the MOT, the second is that the $-y$ coils are used to set the quantization axis, these coils will be used in the next step, the magnetic trapping. A bias field in the $-y$ direction is used to set the depth and the bottom of the trap. Since during the magnetic trapping the speed of the fields is important to catch them, this field will be switched to the value necessary for the magnetic trapping in this stage, so that it is not necessary to turn it on during the magnetic catching, thus improving the number of atoms and their temperature in the magnetic trap.

After this step the cloud is slightly hotter and moved from the starting position due to the pushing of the optical pumping beam. In figure 4.13 the parameters of the cloud after the pumping are given. However to check the efficiency of the optical pumping one has to wait till the next step, the loading of the magnetic trap, described in the following section.



Optically pumped cloud

Number of atoms N . 7×10^7
 Radial size y (μm) . **600**
 Axial size z (μm) . **800**
 Peak density n_0 (m^{-3}) . 2.1×10^{16}
 Temperature T (μK) . **13**
 Phase space density PSD 3.0×10^{-6}

Figure 4.13: After the optical pumping the cloud has this characteristics.

4.5 The magnetic trapping

The atoms are now ready to be caught in a magnetic trap. The magnetic trap is formed by ramping up the current of the Z-shape wire under the chip and $-x$ bias coils. At this point the key optimization parameter will change, now the elastic collision rate provide the necessary information for starting the last cooling stage, evaporative cooling. Let see how one can get this number and optimize it during the loading of the trap.

Efficient evaporative cooling requires the elastic collision rate,

$$\gamma_{el} = n_0 \sigma_{el} \bar{v}_{th}$$

to be much larger than the loss rate in the magnetic trap. Here n_0 is the density, σ_{el} the elastic scattering cross section, and \bar{v}_{th} is the average velocity of the thermal atoms

$$\bar{v}_{th} = \sqrt{\frac{8\kappa_B T}{\pi m_{Rb}}} . \quad (4.4)$$

4. REACHING BEC

Furthermore, for continued cooling as the evaporative ramp progresses, the elastic collision rate must be maintained despite the reduction in atom number. With the correct conditions, γ_{el} can actually increase during the evaporation process and runaway evaporation can be achieved.

In a harmonic trap the Maxwell-Boltzmann velocity distribution of the atoms of a thermal cloud gives a Gaussian spatial distribution, and the peak density is

$$n_0 = \frac{N}{(2\pi)^{3/2} \sigma_x \sigma_y \sigma_z}, \quad (4.5)$$

where σ_i is

$$\sigma_i = \sqrt{\frac{\kappa_B T}{m \omega_i^2}}. \quad (4.6)$$

Defining the geometric mean of the frequencies as $\bar{\omega} = \sqrt{\omega_x \omega_y \omega_z}$ one can write the density as

$$n_0 = \left(\frac{m}{\kappa_B 2\pi} \right)^{3/2} \frac{N \bar{\omega}^3}{T^{3/2}}, \quad (4.7)$$

Using the relation 4.4, the elastic collision rate therefore varies as

$$\gamma_{el} \propto \bar{\omega}^3 \frac{N}{T}. \quad (4.8)$$

The parameter $\bar{\omega}$ is linked with the potential and will not be taken into account in the loading step. Hence, it will be considered that the elastic collision rate scales as

$$\gamma_{el} \propto \frac{N}{T} \quad (4.9)$$

Phase space density is another crucial parameter in reaching BEC. The transition to BEC occurs when phase space density increases to the order of one. Using equations 4.2 and 4.3, it can be obtained that the phase space density is proportional to

$$\rho \propto \frac{N}{T^3} \quad (4.10)$$

and so that there is a regime in which ρ can increase even though the elastic collision rate decreases. Therefore, an increase in ρ is not a stringent enough criterion for maintaining runaway evaporative cooling. The standard method of characterizing an atomic cloud is absorption imaging. Optical depth, defined through Beer law's as $OD = \ln(\frac{I_0}{I_t})$ is the important quantity to extract. On resonance, for a closed transition with equal statistical weights, and for the laser linewidth much smaller than the natural linewidth of the transition, the peak optical depth measured at the center of a cloud that has been released

4. REACHING BEC

and expanded from a trap is described by the equation below

$$OD = \frac{\lambda^2 m}{4\pi^2 \kappa_B t^2} \frac{N}{T}. \quad (4.11)$$

In deriving this equation, one has to assume that the cloud has been expanded for a time t to a size much larger than the original size of the cloud in the trap. See section 3.7 for the full equations describing atom number and temperature. The peak optical depth is seen to be proportional to N/T and is therefore directly proportional to the elastic collision rate. The simple observation of the trend of the optical depth peak in a series of absorption images tells us whether our evaporation is efficient. An increase in the peak optical depth indicates an increase in the elastic collision rate, efficient runaway evaporation, and is a sufficient criterion to ensure that the phase transition will be reached. Decreasing peak optical depth on the other hand indicates decreasing elastic collision rate and inefficient evaporation. The phase transition will not be reached under these conditions.

Trap height

The selection of the height of the trap, with respect to the chip surface, was made respecting two criteria. First, to be near to the center of the quadrupole to avoid the problems with the ramps. Second, the potential has to be strong and deep enough to trap the falling atoms, and that means to be near the surface. These two criteria push in opposite directions, so lets look at some numbers.

For the restoring force $F \propto B'$ along the vertical axis, the minimum requirement to compensate gravity is $B'_z \geq mg/\mu_m$. For the state $F = 2, m_F = 2$ of ^{87}Rb , the minimum field gradient is 15 G/cm. According to the simulation of the fields this minimum is around 4 mm above the chip surface with the maximum current, 25 Amps, in the z wire.

But at this distance there is not enough depth. In order to properly confine atoms, the trap potential has to be well above the mean level of the atoms energy. A trap of a finite depth containing a thermal atomic ensemble (temperature T) will have losses due to the atoms boiling out of the trap. Therefore, the trap depth should be large compared to the mean atomic energy.

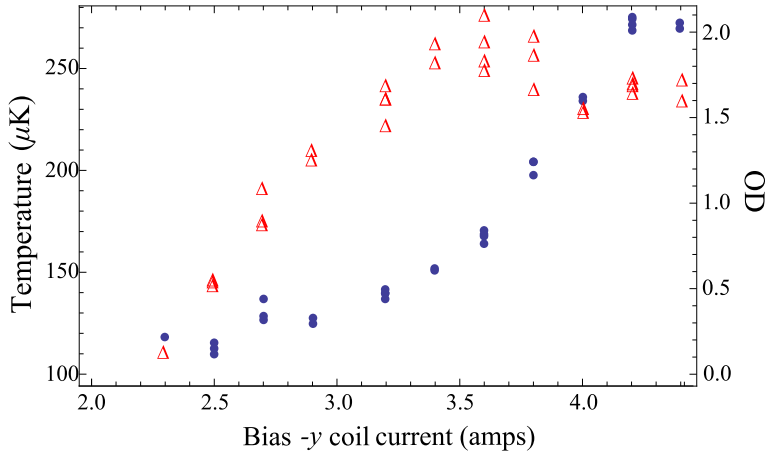


Figure 4.14: Optical density (red triangles) and temperature (blue discs) of the magnetic trapped atoms at different values of bias $-y$ coils. The number of atom increases linearly but the OD has a saturation behavior, the bottom of the trap is crossing the zero field, this heats the atoms and saturates the OD.

This leads to the condition $V_{pot} = |\mu_m B_{max}| \geq \eta \kappa_B T$ with the rule-of-thumb value $\eta=5-7$ in order to make this loss term negligible. For $F = 2, m_F = 2$ of ^{87}Rb state, a bias of 1 Gauss is equivalent to the temperature $T = 67 \mu\text{K}$. Hence, for a cloud of $13 \mu\text{K}$ we need at least 2-3 Gauss of bias field, if one checks with the simulations that take into account the gravity, this requirement is accomplished at 2.5 mm over the chip surface.

We show in section 2.3.5 that the z shape trap is the analogous of a Ioffe trap. The bias field at the bottom of the trap is produced by the arms of the z . In the previous calculations this bias is canceled to achieve the full depth of the trap; in the experiment this is done by the $-y$ coils. In order to avoid the Majorana spin flips 2.3.2, some bias field is needed not to cross the zero field. So the final trap will be a bit nearer to the chip, at 2 mm, in order to get more bias. During the experiment we prefer to have smaller trap depth in order to get colder atoms, to do this we increase the bias at the bottom of the trap decreasing the field of the $-y$ coils.

The initial point to catch the atoms is at 2 millimeters from the chip surface an 2 Gauss of bias field at the center of the trap. With 25 Amps running through the z shape wire 10 Gauss field are needed on the $-x$ direction and 3 Gauss in the $-y$ direction.

Later measures of OD versus these two magnetic fields are reported in the

4. REACHING BEC

figures 4.14 and 4.15. From this new data one can conclude that there is space to improve the number of atoms or the optical density using more bias. A trap near the chip means more bias in the $-x$ direction, this increase the gradients of the trap heating the atoms, but at the same time this increase the number of atoms. In this competition the key parameter of the cloud, OD, increases up to some value, as in the bias $-y$ case. This behavior is show in figure 4.15. In both cases, $-y$ and $-x$ biases, the determining factor to increase the OD is the trap depth. Therefore, this point can be improved, a change in this trapping bias can lead to an increase in the number of atoms in the condensate.

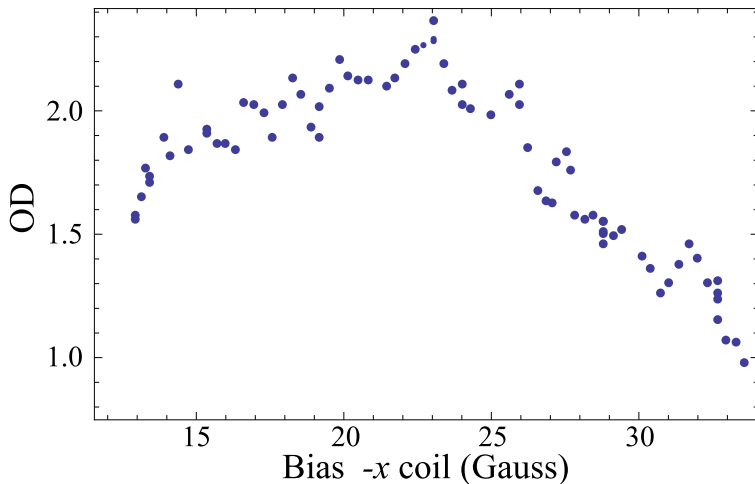


Figure 4.15: Optical density of the magnetic trapped atoms at different values of bias $-x$ coils. The heating that the atoms suffer during the non adiabatic magnetic catching is in competition with the number of atoms.

Optimizing the magnetic trapping

In order to maximize the loading of the magnetic trap, one had to be cautious with two points:

First, the position and size of the trap should be matched to the position and the dimensions of the atom cloud after optical pumping. This is called mode-matching, in analogy with the coupling of light into an optical fiber. If the trap is too tight or too weak, breathing oscillations of the cloud are excited. If the trap and the cloud are not properly overlapped, center of mass oscillations will occur. Both excitations heat the cloud.

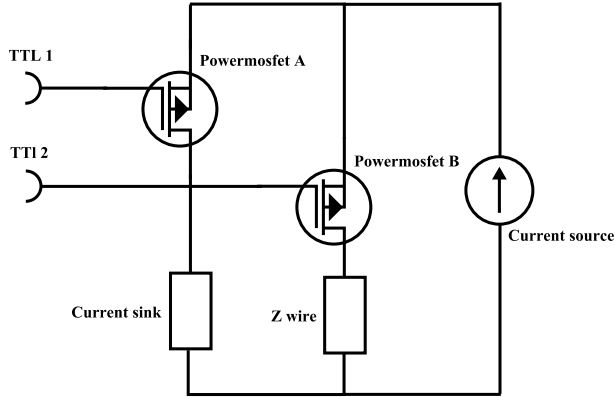


Figure 4.16: The circuit used to enhance the dynamics of the Z-shape wire driver. Around 100 ms before the trap is switched on by closing the circuit with the PowerMOSFET A, using the TTL signal 1, the PowerMOSFET B opens with the TTL signal 2 and the driver is set to 25 amps, the current in this case flowing only in the current sink circuit. In the trap catching the situation can be inverted by opening PowerMOSFET B and closing the PowerMOSFET B, the switch the current to the Z-shape wire circuit. The impedances of the current sink and the Z-shape wire have to be similar, if is not possible to change the value of the current in the first step the output voltages can be matched.

Second point is the dynamics of the switch. One can not slowly ramp the magnetic field up from zero because of the effect of gravity. Instead, the magnetic trapping field has to be turned on fast compared to the atomic motion. One also does not want to turn on the magnetic trap at the highest gradient possible because this will add an excess amount of energy to the cloud. So one has to diabatically turn on the magnetic trap to a point where gravity has a minimal effect and yet the magnetic trap adds as little potential energy as possible.

The design of this Z-shape wire trap is described in the section 3.3, size and shape is decided by the geometry of this Z-shape wire. In order to get better mode-matching the previous steps can only be optimized, CMOT and molasses, to reduce the volume of the cloud. The effect of the dimension of the cloud can be seen because for small numbers of atoms, the transfer efficiency is above 90 %, whereas for larger atom numbers, the transfer efficiency drops, because the size of the laser-cooled atomic cloud exceeds the magnetic trap volume.

To obtain good loading efficiency, it was important to minimize the center

4. REACHING BEC

of mass motion (sloshing) of the atom cloud after loading. The sloshing causes heating and in a shallow trap it can lead to atoms spilling out of the trap. Minimizing the sloshing means optimizing the relative position of the magnetic trap and the optically pumped cloud. The sloshing was suppressed by adjusting the optical pumped cloud position to the center of the magnetic trap by using the bias coils. The sloshing was suppressed by adjusting the optical pumped cloud position to the center of the magnetic trap by using the bias coils. The residual sloshing observed was $\sim 30 \mu\text{m}$ (p-p) in the z direction and $\sim 10 \mu\text{m}$ (p-p) in the y direction. In the z direction, this was primarily due to the anisotropic shape of the trapping potential, and the small amount of kinetic energy that the cloud acquired while falling during optical pumping. The residual motion in the y direction occurs because the cloud is pushed slightly during optical pumping.

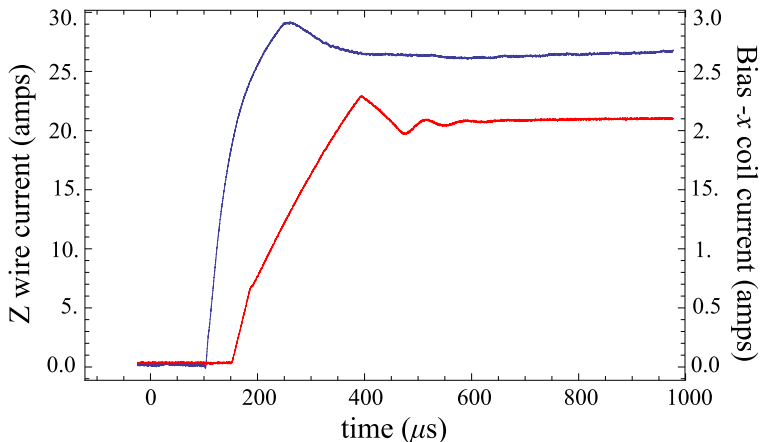


Figure 4.17: The magnetic trap sequence. Red and blue traces show the current, in different scales, through the Z-shape wire and bias $-x$ coils respectively. The trap sequence starts at 0 and both field are on in less than 0.5 ms.

The dynamics is another point that can improve the magnetic catching. The fields from the Z-shape wire and the bias $-x$ coils have to be fast enough and synchronized to trap a good number of atoms with small heating. The current driver of the Z was not fast enough to switch on, the power supply takes more than 5 ms. To improve this first step were used a PowerMOSFET system like a fast switch, setting the driver to the right current level before and then switching on the current with the PowerMOSFET circuit. The main problem of this mechanism is that the driver with the PowerMOSFET open gives the maximum voltage so a peak on voltage appears in the first ms till the driver

adjusts the output voltage. The solution was a double PowerMOSFET circuit. In this case the a second PowerMOSFET is used to deviate the current to a current sink closed circuit before the switching on, in this case voltage output of the driver depends on the current sink impedance. The circuit is shown in figure 4.16 and the procedure is illustrated in its caption.

Using of this circuit allow us to turn on faster the current in the Z-shape wire. If we take a look at figure 4.17 we can see that the Z can be switched on in less than $300 \mu\text{s}$. The total switching on of the trap can be done in less than $500 \mu\text{s}$, the slowest field being the bias $-x$, due to its high impedance. Remember that the bias $-y$ field is still on from the optical pumping stage. As a result of this, ones an increase of the atom number is observed, at least 50 %, without any increment in the temperature of the magnetically trapped atoms. Some tests with ramps of the current were done to make the switching even smoother, but poor results brought the end to this activity.

At this point the optical pumping can be optimized (pulse time length, power and frequency) to maximize the magnetic trap loading efficiency. The increase in transfer to the magnetic trap with optical pumping is shown in figure 4.18. The gain factor of 2.5 corresponds to the expected ratio of all-trapped to untrapped states assuming an even distribution across m_F states after optical cooling.

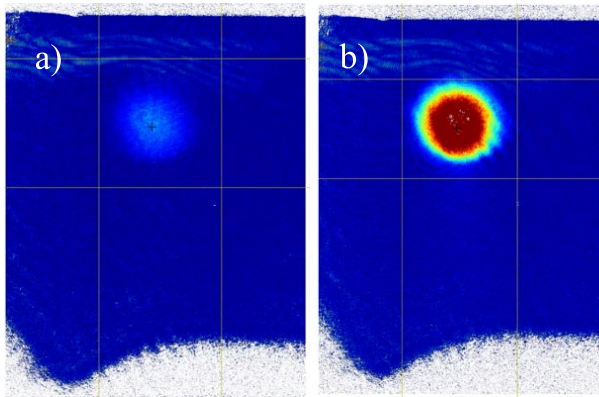


Figure 4.18: Absorption images of the atoms after 5 ms expansion from the magnetic trap a) without optical pumping before the capture in the magnetic trap, and b) with optical pumping.

The lifetime of this magnetic trap was impossible to measure due to a big heating rate of the wire. The wire with 25 Amps running through it cannot be

4. REACHING BEC

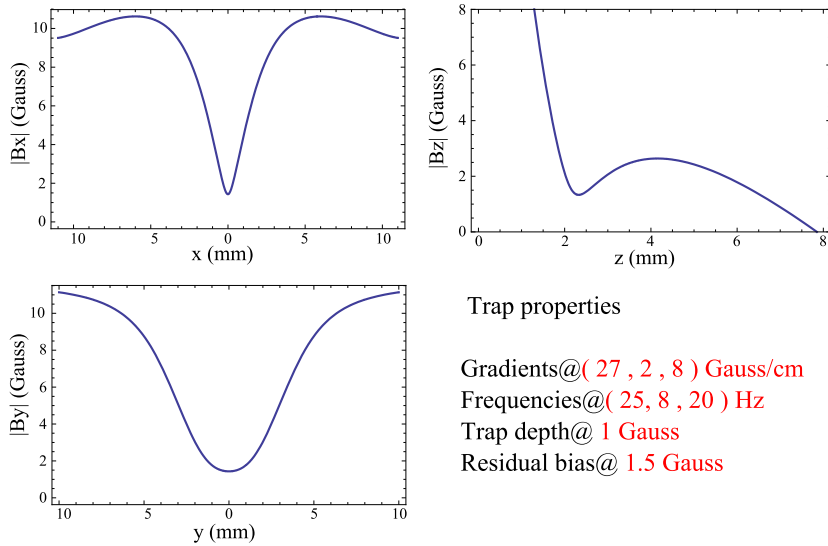
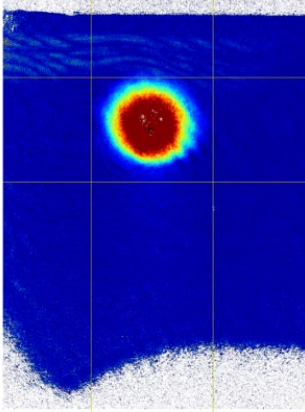


Figure 4.19: Simulated fields of the Z-shape wire trap with 25 amps and bias fields of 10.8 Gauss in $-x$ and 4.1 Gauss in $-y$ directions. The simulations includes the gravity. The calculated trap depth is in z direction because it has the lowest barrier.

on for more than 2 seconds, because its small cross section (0.6 mm in diameter) cannot support 25 Amps without significant ohmic heating. If the wire is on for more than 2 seconds a big increment in the pressure of the chamber, due to a degassing of the wire is observed. No lifetime measurements of this trap are presented due to this overheating problem. In future designs, this wire will be replaced by a bigger area conductor without kapton isolation. For this set up we ignore the lifetime in this trap since is used only for the magnetic trapping of the atoms, and is not the final trap to make the evaporation, it is used the time necessary to trap and transfer the atoms to the z on-chip trap. In the next section it will be show that this adiabatic transfer takes only 250 ms, the Z-shape wire does not suffer any heating. In the figure 4.20 all the characteristic of the magnetic trap based on experimental data are resumed.

4.6 The compressed trap

The last cooling stage, evaporative cooling, needs a high collision rate to thermalize the atoms faster than they are lost from the magnetic trap. To boost



Magnetic Trap

Number of atoms N . 3×10^7
 Radial size y (μm). $.300$
 Axial size z (μm). $.700$
 Peak density n_0 (m^{-3}). 4.3×10^{16}
 Temperature T (μK). $.15$
 Phase space density PSD 4.9×10^{-6}
 Elastic collision rate (s^{-1}) 0.5

Figure 4.20: An absorption image of the trapped atoms after 15 ms of free falling, with its characteristics.

the collision rate so that effective evaporative cooling is possible, the trap must be compressed to increase the density.

The extreme compressibility of chip traps is one of the strongest points of this kind of magnetic traps. Compression plays a crucial role in BEC experiments because it increases the collision rate γ_{el} , which sets the time scale for evaporative cooling. Remember from 2.80 reaching the situation for runaway evaporation requires the following condition

$$\gamma_{el}\tau_{loss} \geq 150. \quad (4.12)$$

Adiabatic compression

The magnetic trap is conservative and so the optimum compression is adiabatic, i.e. the initial phase space density is preserved. Compressing adiabatically also gives the highest possible collision rate for a given compression ratio.

We can calculate the theoretical temperature rise in the case of a perfectly adiabatic compression. Using equations 4.2 and 4.3, in the magnetic trap, the volume of phase space occupied is proportional to

$$\Phi \propto \frac{\bar{\omega}^3}{T^3}, \quad (4.13)$$

4. REACHING BEC

including $\bar{\omega}$, the geometric mean trap frequency, because it increases during the adiabatic compression while the number of atoms, N , remains constant. Adiabatic processes conserve phase space volume, and so the ratio of initial and final temperatures is given by

$$\Phi = \text{const} \quad \Rightarrow \quad \frac{T_i}{T_f} = \frac{\bar{\omega}_i}{\bar{\omega}_f} \quad (4.14)$$

Therefore, in adiabatic process

$$\Delta T \propto \Delta \bar{\omega}. \quad (4.15)$$

While adiabaticity is very desirable, the need for a slow compression must be balanced against the finite lifetime of the magnetic trap. By examining the trap frequencies for the uncompressed and compressed trap one can check if a compression ramp is well within the adiabatic regime.

Actually we use a more empirical mode to see if the compression is adiabatic, starting from a fast ramp we slow the ramps till the atoms arrive to the lowest temperature. This scaling law, equation 4.15, also is useful for the next calculations.

Trap depth

A potential loss factor that has to be considered is the limited trap depth. Obviously, the higher temperature after compression requires a deeper trap, and this is not always achieved. Lets think what happens during the classical compression when the bias field B_0 is increased. When the trap is compressed adiabatically by slowly increasing the bias field the trap depth grows proportional to B_0 (if we neglect the small bias field in the trap center). To obtain a crude estimate of the associated temperature increase, let me approximate the process as the compression of the potential of a thin wire trap. The scaling

laws for the wire potentials are

$$B \propto \frac{I}{r} \quad \text{magnetic field,} \quad (4.16a)$$

$$B' \propto \frac{I}{r^2} \quad \text{gradient,} \quad (4.16b)$$

$$B'' \propto \frac{I}{B_{ip}r^3} \quad \text{curvature,.} \quad (4.16c)$$

Where I is the current of the wire, r is the distance from the trap center to the wire and B_{ip} is residual magnetic field at the trap center. The radial frequency of this potential scales with the curvature as

$$\omega^2 \propto B'' \quad \Rightarrow \quad \omega^2 \propto \frac{I}{B_{ip}r^3}. \quad (4.17)$$

If during the adiabatic compression the current and the residual bias are constants, using the relations 4.16a and 4.17 we can arrive to the relation

$$\omega^2 \propto B^3. \quad (4.18)$$

If the compression is adiabatic from the relation 4.15 we see that the temperature scales as

$$T \propto B^{3/2}. \quad (4.19)$$

If the trap temperature limit, T_{depth} , is proportional to the change in the bias field, B_0

$$T_{depth} \propto B_0. \quad (4.20a)$$

$$T \propto B_0^{3/2}.$$

Hence, the temperature only grows slightly faster than the trap depth. Within this crude model, the trap will remain about "as full" as it was before compression, and boiling out of the trap will not become a major loss factor due to the compression, which is a reassuring result.

If we compress by increasing the current of the wire and maintaining the

4. REACHING BEC

distance, following the same deduction as above we can arrive to the relation

$$\begin{aligned} T_{depth} &\propto I. \\ T &\propto \sqrt{I}. \end{aligned} \tag{4.21a}$$

In this case the trap depth grows faster than the temperature of the atoms. There are no losses due to the *boiling out* with this compression, but the problem is limited current that we can send into the wire.

Note that, in view of the spill-over problem, compressing the trap by increasing B_0 is certainly a better choice than reducing I . The latter method also leads to trap compression, but leaves the trap depth unchanged. Thus, unless the initial n was very large, such a compression will present significant losses.

The simplification made above, to identify the external field B_0 with the trap depth, has some limits that should not be forgotten. First, the contribution of gravity to the total potential has been neglected. In steep traps, the effect of this correction is small. On the other hand, when the trap is very strongly compressed by increasing B_0 , the finite field at the wire surface must be taken into account; for a wire of finite width, this is

$$B_s = \frac{\mu_0 I}{w} - B_0. \tag{4.22}$$

Thus, B_s limits the trap depth only when $z \lesssim w$.

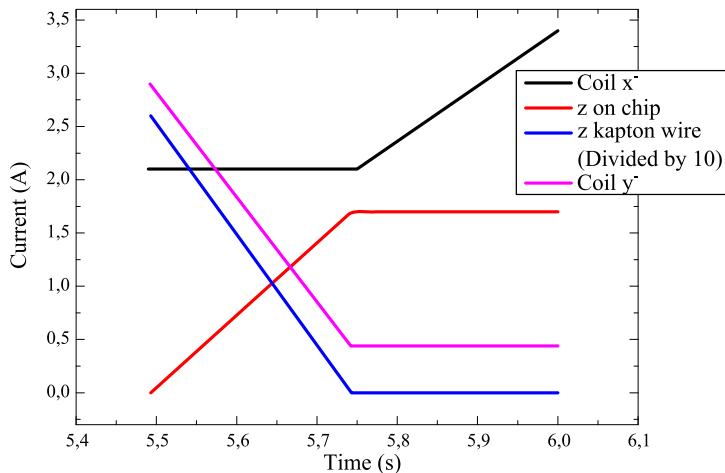


Figure 4.21: A timeline of the currents involved in the two compression step.

Adiabatic compression in practice

The adiabatic compression of the cloud in two steps: In the first step the cloud is transferred from the Z-shape kapton wire to the z on-chip wire, in this step the compression is strong. In the second step the cloud is compressed by increasing the bias necessary to form the wire trap, bias $-x$.

After having loaded the Z-shape kapton wire trap we start a magnetic field ramp that adiabatically transfers the atoms to a potential made with the z wire on-chip. The z wire on-chip current is linearly ramped to 1.7 A in 250 ms while the Z-shape kapton wire is turned off by a linear ramp. At the same time the bias field in the y-coils are ramped down to maintain the residual field at the trap center. In the second compression the bias coils $-x$ is ramped up from 10.5 G to 15.5 G in 250 ms. A time line of the compression is showed in figure 4.21.

Compress trap magnetic potential properties

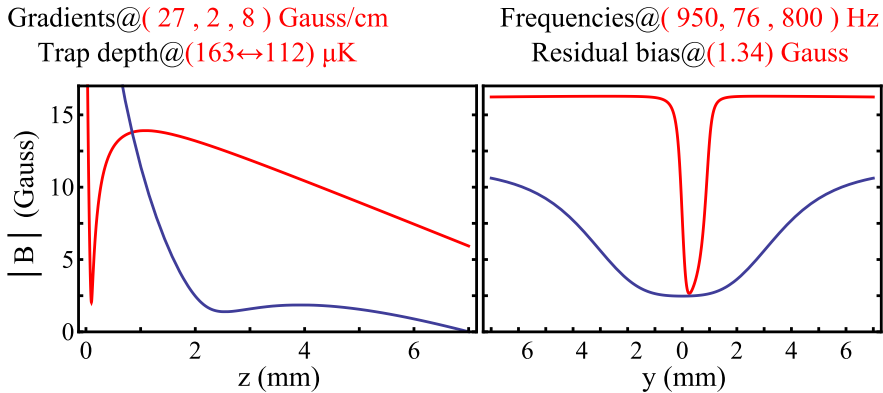


Figure 4.22: Up: Properties of the magnetic potential of the compress trap. Down: Simulated magnetic fields of the first magnetic trap (blue), and the compressed trap (red).

After this transformation the predicted trap frequencies are $\omega = 2\pi \times 75$ Hz in the axial and $\omega = 2\pi \times 800$ Hz in the radial direction. The bottom field was try to maintained nearly 1 Gauss, and the trap depth is increased enough to contain all the "heated" atoms. In figure 4.22 the simulated potential compression is showed. This trap is highly anisotropic, most of the compression comes from the radial dimension, as is showed in figure 4.23, the cloud takes its typical

4. REACHING BEC

cigar-shaped form, this is one of the reasons why the trap is not useful for the magnetic catching. The MOT or CMOT, shape differ greatly from this trap.

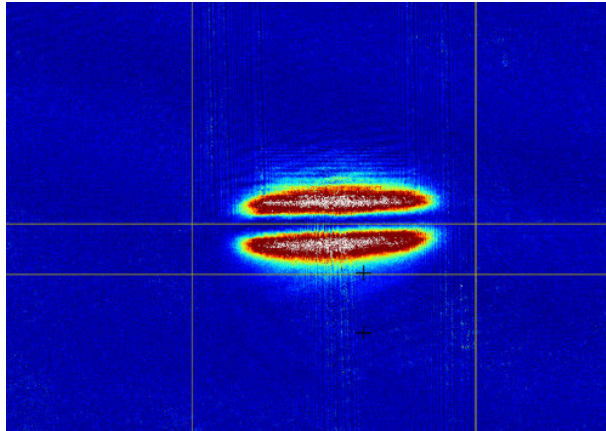


Figure 4.23: Absorption image after 2 ms of free expansion of the compressed trap, the cloud has typical cigar-shape form due to the anisotropic potential.

At the end of the compression phase, the trap was located $190 \mu\text{m}$ above the surface of the guide wire. The parameters of the compressed trap can be calculated from the fields produced by all the wires and the coils. However, uncertainties in the position of the end wires mean that it is difficult to make accurate calculations of the trap frequencies and the magnetic field at the bottom of the trap. Instead, these parameters were measured experimentally.

The trap frequency can be measured by displacing a cloud from the center of the trap and measuring the oscillation frequency of the center of mass of the cloud. These measurements must be performed using small displacements and cold clouds to ensure that the cloud remains in the harmonic region of the potential.

Such measurements are presented in figures 4.24 and 4.25. In both cases, evaporative cooling was used to prepare cold clouds at $\sim 5 \mu\text{K}$. The position of the center of mass of the cloud is measured using Gaussian fits to the radial and axial profiles. The radial fit is an exponentially damped sine wave with a linearly varying offset. This gives an oscillation frequency of $\omega_r = 2\pi \times 935 \text{ s}^{-1}$. The axial fit is a simple sine wave, and yields an axial frequency of $\omega_a = 2\pi \times 76 \text{ s}^{-1}$. The axial bottom field was measured spectroscopically, with a RF radiation and yields a number of 1 Gauss. The divergence from the calculated

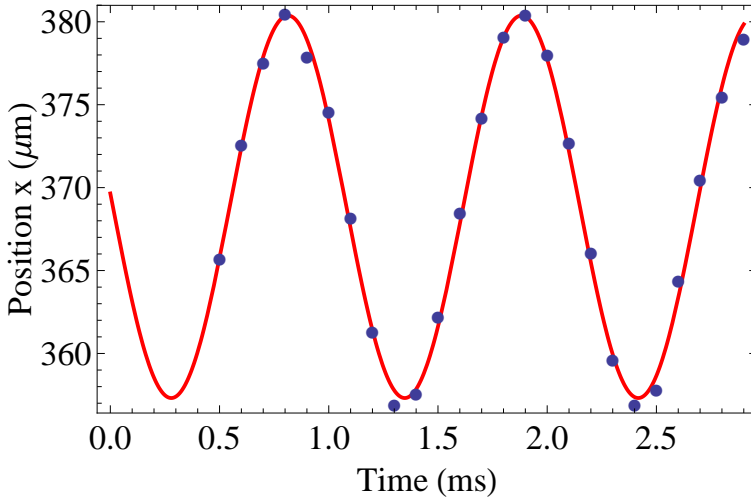


Figure 4.24: Measurements of the radial trap frequencies. Solid red lines are fits to the measured cloud positions (points).

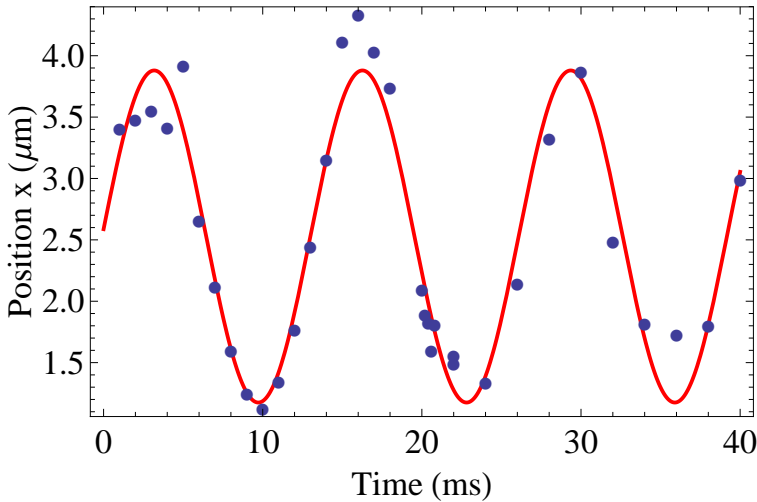


Figure 4.25: Measurements of the axial trap frequencies. Solid red lines are fits to the measured cloud positions (points).

potential will be explained in the next section 4.7.

For our compression, equation 4.15 predicts that the temperature should increase by a factor of 10, giving a the final temperature of $\sim 150 \mu\text{K}$. This is close to the temperature calculated from the width of the cloud $\sim 90 \mu\text{K}$, which suggests that our compression is close to adiabatic.

4. REACHING BEC

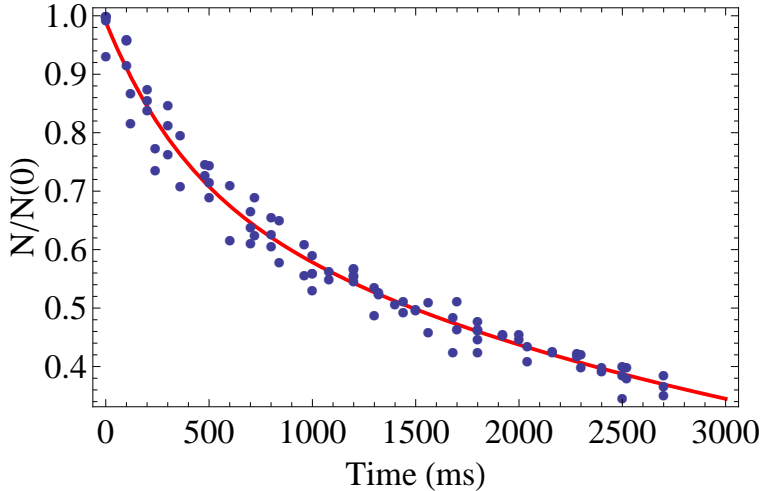
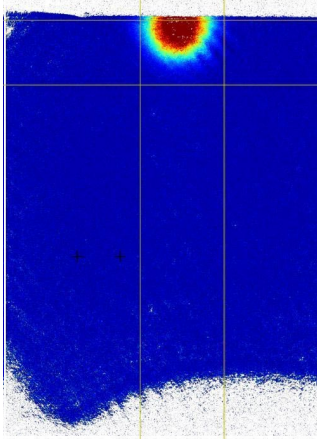


Figure 4.26: The decay of the compressed cloud. Points show the experimental data. The solid line is a fit to an exponential decay with the lifetimes of 0.4 s and 3.4 s at short and long times respectively.

In the mode-matched trap, the collision rate is very low, and the compression is not slow compared to the collision rate. The cloud parameters presented in figure 4.27 were measured 500 ms after the end of the compression phase, when rethermalization has taken place. If the cloud is imaged immediately after the compression, it is much wider radially and shorter axially, which reflects the greater heating in the radial direction due to the anisotropic compression. The number of atoms drops faster due to the limited trap depth. As is showed before the potential trap depth increase can not compensate the heating up of the atoms. During the compression, the collision rate has increased by a factor of 90, reaching 250 s^{-1} . The decay in atom number of this cloud in the compressed trap is shown in figure 4.26. The faster decay at short times is probably due to the trap depth. Using this initial lifetime, our value for the factor $\gamma_{el}\tau_{loss}$ is therefore 370, which is within the regime where runaway evaporation can be achieved. As the evaporation progresses, the decay rate drops, which will improve the efficiency. The lifetime at long times is shorter than the 30 s observed in the mode-matched trap. However, for clouds that have been evaporatively cooled to a few μK , the lifetime in the compressed trap can be as long as 30 s, which indicates that there is another loss mechanism other than background collisions operating for these relatively hot clouds.



z on chip compress trap

Number of atoms N . 1.5×10^7
 Radial size y (μm). $.17$
 Axial size z (μm). 500
 Peak density n_0 (m^{-3}). 2.3×10^{18}
 Temperature T (μK). $.90$
 Phase space density PSD 1.8×10^{-5}
 Elastic collision rate (s^{-1}). $.265$

Figure 4.27: Absorption image of the z on-chip compressed magnetic trap with its characteristics.

4.7 Evaporative Cooling step

The next step along the path to BEC is to apply forced RF evaporative cooling to the compressed atom cloud. After compression we start an exponential frequency sweep from 22 MHz to a final value of 2.2 MHz with a duration of 1 s, after which a linear frequency sweep from 2.2 MHz in 2 s is enough to cool the atoms to the degeneracy. In figure 4.28 these two sweeps are shown. Condensation is reached at the atom number of 3×10^4 and the temperature of 500 nK. The RF ramp was optimized experimentally, by measuring the final phase space density and collision rate as the parameters were adjusted. In the next section we describe the signatures for Bose-Einstein condensation, and summarize our condensate's properties.

Fragmentation of the cloud

During the first testing of evaporation ramp an unexpected structure were revealed as the cloud were cooled down. Figure 4.29 shows that the cloud fragments in the area of a T-junction in the main wire. This occurs because the current expands into the T-junction and is thus no longer straight down the wire 4.30. If the current is locally bowing at an angle to the primary wire, it produces a localized longitudinal field. We estimate that the T-junction

4. REACHING BEC

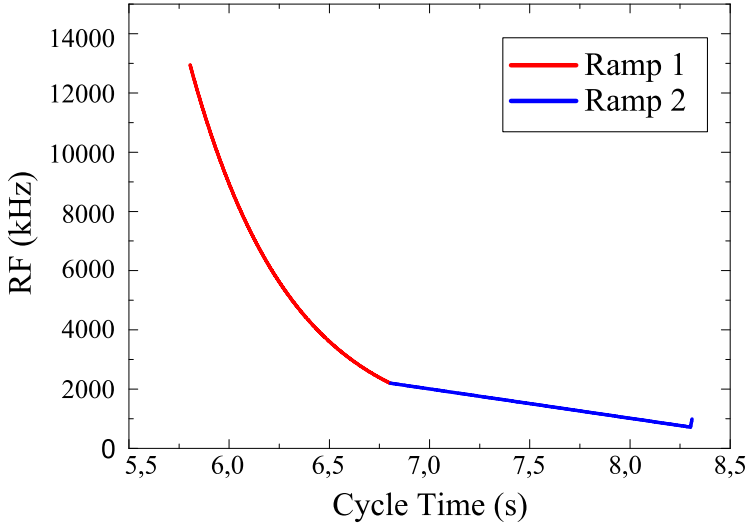


Figure 4.28: The evaporative cooling rf frequency sweep. Over 2.5 s, the frequency is changed from 13 MHz down to ~ 700 kHz, where the phase transition occurs. The slight frequency increase at the very end is used to extend the condensate lifetime by keeping a constant RF knife on.

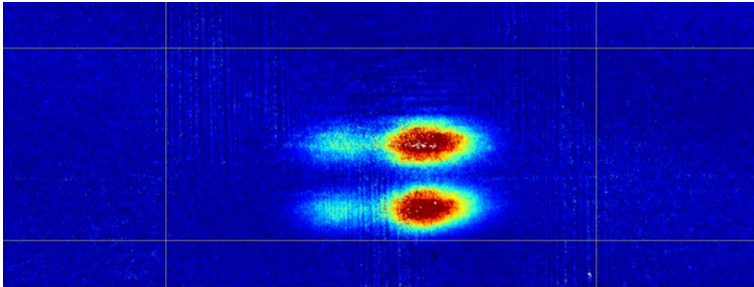


Figure 4.29: Image of the fragmented cloud. The division of the cloud occurs before the evaporation is completed.

causes a 100 mG feature in the longitudinal field when there is 1.7 A running through the wire. When there is a cross in the main wire, the current expands symmetrically, and the effect is minimized. Other structures can appear in the cloud due to small deviations of the average direction of current in the primary wire as shown by References [49, 51].

This new feature of the trap was not desirable but on the other hand could

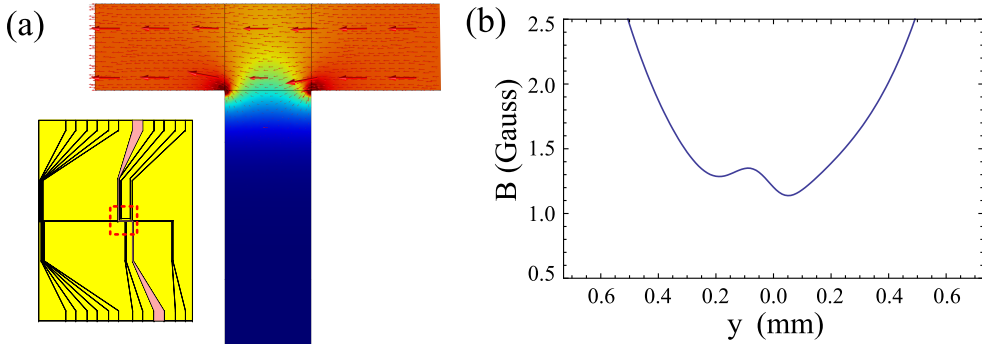


Figure 4.30: (a) Simulation of the current inside the primary wire as it passes by an intersecting wire forming a T-junction. (b) Simulation of the trapping magnetic field taking into account the longitudinal current deviations. The simulation of the current density was performed with Comsol multiphysics software.

be of help to the cooling process. This trap can bring a localized increment of the density, due to the diminution of the volume, Since the temperature remains constant, this leads to a local increment in the phase space density.

4.8 BEC signatures

Once the RF sweep was producing cold clouds ($T < 1 \mu\text{K}$), and the evaporation was clearly working, we started looking for evidence of Bose-Einstein condensation. In this section I will look for fundamental signatures of this phase transition.

The density distribution of a thermal cloud and a pure BEC in a harmonic trap were both considered in Chapter 2. The thermal cloud was shown to have a Gaussian spatial distribution, while the ground-state of the condensate was shown to have the parabolic Thomas-Fermi distribution. To analyze the data on condensate formation, the discussion must be extended to include the density distribution of partially condensed clouds. The condensed cloud in the TF approximation acquires an inverted parabolic density profile

$$n_{TF}(\vec{x}) = \frac{15}{8\pi} \frac{N}{\prod R_j} \max \left(1 - \sum_{j=1}^3 \frac{x_j^2}{R_j^2}, 0 \right). \quad (4.23)$$

4. REACHING BEC

The Fermi radii of the cloud along direction j are related to the harmonic potential with

$$R(0)_j = \frac{1}{\omega_j} \sqrt{\frac{2\mu}{m}}, \quad (4.24)$$

where ω_j is the harmonic frequency of the potential in the j direction and μ is the chemical potential, given by

$$\mu = \frac{1}{2} \hbar \bar{\omega} \left(15a N_{TF} \sqrt{\frac{\bar{\omega}}{m\hbar}} \right)^{2/5}, \quad (4.25)$$

where a is the s-wave scattering length for ^{87}Rb and N_{TF} is the number of condensed atoms.

The BEC is formed and trapped in a cigar shaped trap where the radial confinement is much stronger than the longitudinal confinement ($\omega_{rad}\omega_{par} \sim 20$ for our trap).

The simplest approximation is to consider the cloud as composed of two non-interacting parts; a thermal component described by Boltzmann statistics with a Gaussian spatial distribution, and a condensate component, described by the Thomas-Fermi distribution. In this case the combined density distribution can be written as

$$n(\vec{r}) = (1 - f_c)n_{th}(\vec{r}) + f_c n_{TF}(\vec{r}), \quad (4.26)$$

where f_c is the condensed fraction.

4.8.1 Anisotropic expansion

The easiest to observe signature of BEC is anisotropic free expansion upon release from the cloud due to the anisotropic confinement. Unlike thermal clouds, once released from the trap, the condensate expands anisotropically, expanding much faster radially than longitudinally. Once released, the condensate undergoes a radial accelerated expansion as atom-atom interaction energy is converted to kinetic energy.

Following Castin and Dum [78], the asymptotic expansion parameters upon the release from the trap (i.e., the ratio between the width at t and the width

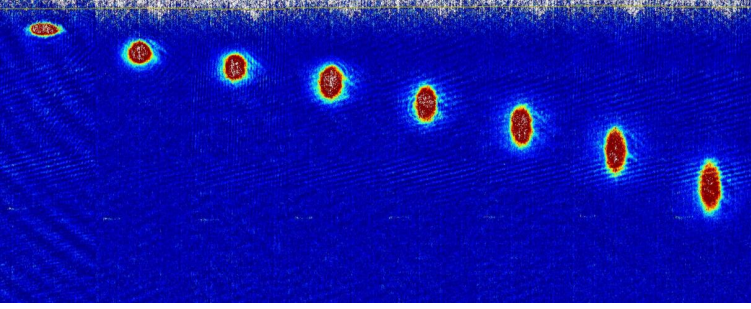


Figure 4.31: First signature of Bose-Einstein condensation a 90° rotation of the aspect ratio upon release from the trap, for a certain TOF . Starting with the long axis of the cigar-shaped cloud parallel to the surface in the trap, the aspect ratio changes during free expansion due to the stronger interaction in the transverse direction, and after $TOF = 10ms$ it is already perpendicular to the surface.

at $t = 0$) are given by

$$R(t)_\perp/R(0)_\perp = \sqrt{1 + (\omega_\perp t)^2} \quad (4.27)$$

$$R(t)_\parallel/R(0)_\parallel = 1 + \frac{\omega_\parallel^2}{\omega_\perp^2} (\omega_\perp t \arctan(\omega_\perp t) - \ln \sqrt{1 + (\omega_\perp t)^2}). \quad (4.28)$$

Taking into account $\omega_\perp/\omega_\parallel \gg 1$ and $\omega_\perp t > 1$ expansion longer than 1 ms, this can be approximated with

$$R(t)_\perp/R(0)_\perp = 1 + \omega_\perp t \quad (4.29)$$

$$R(t)_\parallel/R(0)_\parallel = 1 + \frac{\pi\omega_\parallel^2}{2\omega_\perp} t. \quad (4.30)$$

Since the longitudinal expansion is so small, it is practically negligible within our imaging field of view. When the TOF is large enough, one sees a 90° rotation of the aspect ratio of the initial cigar shape, i.e. the long axis turns from being parallel to the surface, to being perpendicular to the surface. The turn of the aspect ratio is shown in figure 4.31. One should note that this figure integrates the atom distribution over one of the transverse directions, and in fact the shape of the cloud after expansion is not a cigar anymore, but a *pancake* shape. The horizontal line at the top of the images indicates the location of the chip's surface.

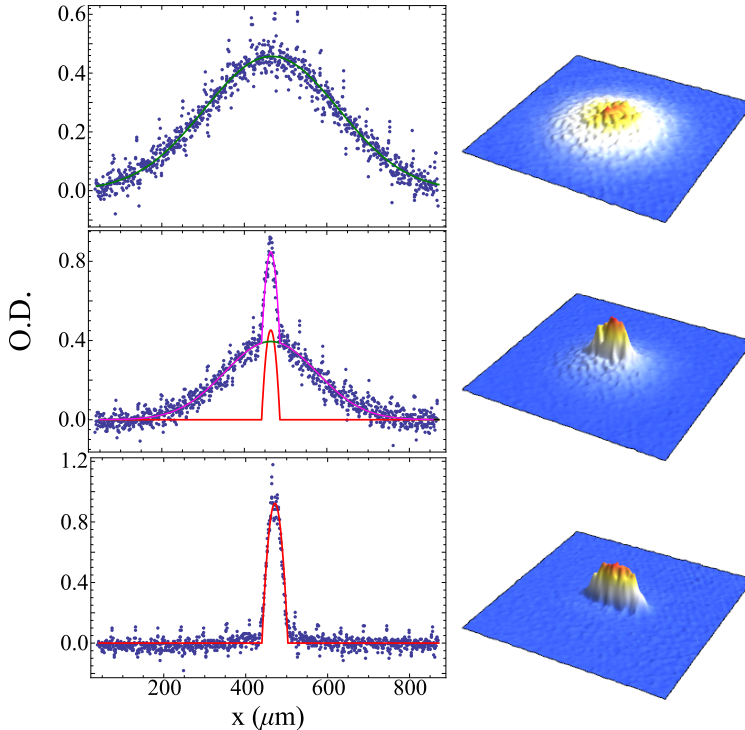


Figure 4.32: A bimodal density profile appears, as the RF sweep frequency crosses the threshold of the phase transition. From up to down: First one, slightly above the threshold, the density distribution is still Gaussian. Second one, a sharp parabolic peak of condensed atoms is emerging within a Gaussian profile of non-condensed atoms at a temperature of $T = 760$ nK. The condensate fraction here is $\sim 10\%$. Third, a Thomas-Fermi distribution of an almost pure condensate (condensate fraction $> 95\%$).

4.8.2 Bimodal density distribution across the phase transition

A closer look at the density distribution of the atom cloud near the threshold for the BEC phase transition reveals the second signature of condensation. As explained previously, condensed atoms in the Thomas-Fermi limit have a parabolic density distribution profile, 4.23. This density profile is substantially different from the Gaussian profile of thermal atoms. As the end frequency of the RF sweep is lowered across the condensation threshold, a narrow parabolic peak appears at the center of the wider Gaussian distribution. This is shown in figure 4.32. The condensate fraction $N_c/N = 1 - (T/T_C)^3$ can be extracted from measurements of the expansion of the thermal tail and the central peak, while the critical temperature is extracted only from the former.

4.8.3 Phase space density

Finally, a full calculation of the phase space density Φ after crossing the condensation threshold, gives the third signature for the phase transition, where we find $\Phi > 2.612$. In figure 4.33 we show a typical plot for the evolution of the phase space density during the RF sweep. During this sweep the phase space density increases by eight orders of magnitude, from 8×10^{-8} , to ~ 3.6 . Once more, we see that the major increase in phase space density occurs at the last few MHz of the RF sweep.

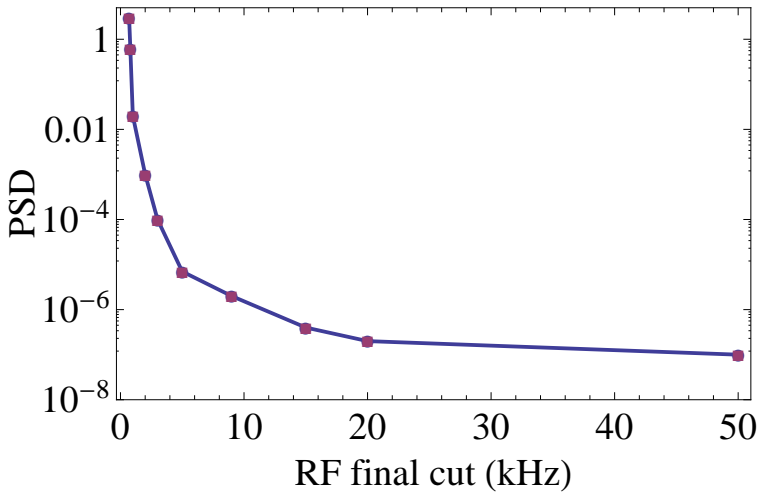


Figure 4.33: Third signature of Bose-Einstein condensation. The phase transition occurs when the phase space density becomes larger than 2.612. It could be seen that most of the phase space density gain occurs in the last stages of the RF sweep.

4.8.4 BEC properties

To summarize, we bring in table 4.1 the important properties of our BEC. The Thomas-Fermi radii, chemical potential, and critical temperature were extracted from the free-expansion images of a non-pure condensate. The trap frequencies were $(\omega_{rad}, \omega_{par}) = (935, 76)$ Hz, as measured with thermal atoms close to the phase transition. The condensate peak density was calculated in the Thomas-Fermi limit to be $n_c = \mu m / (4\pi\hbar^2 a)$. Our numbers are similar to those in other atom chip based experiments. This work serves as the experimental basis for future experiments with ultra-cold atoms near surfaces.

4. REACHING BEC

Property	Value	Units
Number of atoms	3×10^4	
Radial TF radii	1.26	μm
Axial TF radii	15.5	μm
Peak density	7.3×10^{20}	m^{-3}
Chemical potential	6	kHz
Critical Temperature	0.56	μK
de-Broglie wavelength	0.24	μm
Phase Space Density	10.4	

Table 4.1: BEC properties

Atom chip multi-state interferometer

5.1 Introduction

In this chapter I will report on experiments in which ultracold atoms are manipulated coherently on an atom chip.

We introduce a multi-state interferometric scheme that offers advances to both of these aspects. Coherent coupling between Bose-Einstein condensates in different Zeeman states is used to enhance resolution and to maximize the interferometric visibility. We realize an interferometer as a compact, easy-to-use, atom-chip device. This provides an alternative method for the measurement of the light-atom and surface-atom interactions and enables the application of multi-parameter sensing schemes in cold-atom interferometry.

Some of the results reported in this chapter has been submitted for publication, [79].

The first demonstration of coherence of a Bose-Einstein condensate (BEC) [80] has led to dramatic advancements in atom interferometry. Long coherence times and the localization in phase space of cold-atom clouds and in particular of BECs enable high precision interferometric measurements of the internal properties of atoms, many-body effects and gravity [81]. Some notable examples on cold atoms are the determination of spin squeezing [82, 83], recoil frequency [84], fine structure constant [85], density correlations [86], local gravitational acceleration [87, 88], Newtonian gravitational constant [89]

and rotation rate [90]. The unprecedented measurement precision of these interferometers justifies the building of complex and bulky apparatuses such as atom fountains for local gravity measurement its [91]. At the same time, applications outside the laboratory depend on the compactness and robustness of interferometric setups. Therefore, we can identify two important research goals: increase in sensitivity, and simplification and downsizing of interferometers.

5.2 The multi-state interferometer idea

In the classical limit the sensitivity of an interferometer, defined as the smallest signal that can be resolved, is determined by the slope of the interferometric signal and the measurement noise. The best achievable sensitivity of a conventional 2-path interferometer is determined by the shot noise and hence scales as $1/\sqrt{N}$ with the number of atoms N . It is known as the standard quantum limit (SQL). An improvement in sensitivity beyond the standard quantum limit can be achieved by entangling the input and performing a collective non-local measurement at the output. The best possible outcome in a lossless system is a sensitivity of $1/N$, known as the Heisenberg limit [92]. An advancement in this direction has recently been demonstrated by employing nonlinear atom-atom interactions to induce entanglement and therefore reduce the phase-measurement error of a Ramsey interferometer below the SQL [82]. An alternative way to improve the interferometer sensitivity is to increase the fringe slope by increasing the number of paths M as in [93, 94]. This is, however, at the same time accompanied by a decrease in the average number of atoms per path and hence by a greater susceptibility to noise. If the scaling of slope with M exceeds \sqrt{M} scaling of the shot noise, the sensitivity improves with the number of paths. The multi-path interferometry can be also seen as a fringe narrowing mechanism that increases measurement resolution [94, 95].

Here, we present an alternative multi-state cold-atom interferometer. We do not rely on external variables i.e. on spatially separated paths, but use internal atomic states. The multi-state functionality is achieved by coherent manipulation by means of radio-frequency (RF) and static magnetic fields of BECs in different Zeeman states of the same hyperfine level. The interfero-

metric fringes are sharpened due to the higher-harmonic phase contributions of the multiple energetically equidistant Zeeman states.

Several multi-path matter-wave interferometers have been proposed, the first being the atom-beam interferometer based on optical pumping between Zeeman states [94]. Multi-path interferometry with cold atoms has been based on the uses of optical lattices [84, 96, 97, 98, 99], Raman laser pulses [100] and individual laser pulses [101] to cause a controlled atom recoil. While they offer numerous advantages such as a large number of paths, easy control of the relative phase accumulation rate, and compatibility with techniques for control of atom-atom interactions, these interferometers rely on the spatial separation of paths and hence cannot be realized in a trap, crucially depend on alignment, high-resolution imaging (lattices) and require a sophisticated technology to make them compact and eventually portable. Imperfections in alignment and imaging also impose constraints on the visibility of the interferometric signal [99].

5.3 Rabi oscillations and Ramsey spectroscopy

Historically seen, coherent atom optics is an extension of techniques that were developed for manipulating internal quantum states of atoms. A big step forward in this field was the ability to change internal quantum states of atoms using RF resonance as demonstrated in [102]. Subsequently coherent superpositions of internal quantum states were intentionally created and detected [103]. The generalization and application of these techniques have created or advanced many scientific and technical fields, precise frequency standards, nuclear magnetic resonance spectroscopy, and quantum information gates.

Understanding the Rabi oscillations for a two level system is fundamental to the idea of our interferometer. A two-level atom is analogous to a spin-1/2 system with two possible states. In the dipole approximation, when the field wavelength is larger than the atomic size, the atom-field interaction problem is mathematically equivalent to a spin-1/2 particle interacting with a time-dependent magnetic field. Just as the spin-1/2 system undergoes the so-called Rabi oscillations between the spin-up and spin-down states under the action of an oscillating magnetic field, the two-level atom also performs optical Rabi oscillations under the influence of the driving electromagnetic field. An un-

5. ATOM CHIP MULTI-STATE INTERFEROMETER

Understanding of this simple model of the atom-field interaction enables us to consider our system, involving an ensemble of atoms interacting with the field and a multi-state.

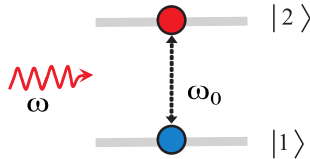


Figure 5.1: Interaction of a two-level atom with a single-mode field.

Consider a two level atom with a transition frequency ω_0 , interacting with a radiation field of frequency ω , Fig. 5.1, described by the wave function

$$|\psi(t)\rangle = C_1(t)|1\rangle + C_2(t)|2\rangle. \quad (5.1)$$

The probabilities of the atom being in states $|1\rangle$ and $|2\rangle$ at time t are described by [104]

$$C_1(t) = ie^{i\phi_0} \sin\left(\frac{\Omega t}{2} e^{i\omega t}\right) \quad (5.2)$$

$$C_2(t) = \cos\left(\frac{\Omega t}{2}\right), \quad (5.3)$$

where ϕ_0 is initial phase, and Ω is the generalized Rabi frequency

$$\Omega = \sqrt{\Omega_R^2 + \Delta^2} \quad (5.4)$$

with the detuning $\Delta = \omega_0 - \omega$ and the Rabi frequency, Ω_R , described by

$$\Omega_R = \frac{|d_{21}|E_0}{\hbar}. \quad (5.5)$$

Where d_{12} is the transition dipole moment between the two states.

The Ramsey spectroscopy, [105] is an interferometry experiment performed in the time domain to study the phase evolution of the system. We now consider the Ramsey method to detect the dephasing accumulated between the states $|1\rangle$ and $|2\rangle$. Each atom is initially prepared in the level $|1\rangle$. It then interacts in a first radiation field tuned at frequency ω , near to the $|1\rangle \rightarrow |2\rangle$ transition frequency ω_0 , and is thus prepared in a coherent superposition

of the levels $|1\rangle$ and $|2\rangle$. We let their phases evolve for a time T , then a second radiation field resonant with the transition is applied. The phase shift proportional to T is introduced in the amplitude of the state $|2\rangle$. And finally it is detected in the state $|1\rangle$ or $|2\rangle$. The probability of detecting an atom in level $|1\rangle$ or $|2\rangle$ is a periodic function of T , and thus gives characteristic fringe patterns.

If the excitation is on resonance, the fraction of the amplitude that is deflected by the transition is determined by the *pulse area* $\theta = \int \Omega dt$. A Ramsey-Bordé $\pi/2$ -pulse (named for the condition $\theta = \pi/2$) results in an equal splitting of the amplitude between states $|1\rangle$ and $|2\rangle$ by the resonant oscillating field.

If the first superposition of states by a Rabi $\pi/2$ -pulse is symmetric, it means

$$|C_1|^2 = |C_2|^2 = 1/2. \quad (5.6)$$

The final periodic function has the form:

$$|C_1|^2 = \frac{1}{2} \left(1 + \cos \left(\omega_0 T + \frac{\pi\omega}{2\Omega} \right) \right) \quad (5.7)$$

Ramsey spectroscopy has the advantage over Rabi measurements that it is most sensitive to the transition frequency during the time interval T , during which the drive is turned off. The signal is thus affected very little by spatial inhomogeneities of Ω_R , and the effect of having different internal states during the phase evolution of the interferometer is more interesting. Many atomic properties such as polarizability depend on the state; hence a Ramsey interferometer naturally measures differences of properties between the states which is generally more informative than just a property of a single state.

5.4 Multi-state interferometer set-up

To build this atom interferometer we follow the usual scheme of an optical interferometer [81].

1. State preparation, to set the initial state.
2. Coherent manipulation, splitting of the initial state to produce a superposition of states.

5. ATOM CHIP MULTI-STATE INTERFEROMETER

3. Free evolution, so that interactions can be applied to each state independently.
4. Coherent recombination, so that phase information gets converted back into state populations.
5. Detection of a specific state population, so that the relative phase of the wavefunction components can be determined from interference fringes.

The corresponding experimental procedure can be divided into three tasks: **preparation**, **manipulation** and **detection**, as shown in the scheme in Fig. 5.2. The initial state is prepared by condensing atoms in a low field seeking ground state, here $|F = 2, m_F = 2\rangle$. The atoms are manipulated by two Rabi pulses. First, a coherent transfer of atoms to other Zeeman states of the same hyperfine state is realized by application of a resonant RF pulse. The interferometer is closed by remixing these states by a second RF pulse after a controllable time delay [106]. The second pulse maps the relative phases accumulated between different states during the delay into a population distribution at the output of the interferometer. Finally, in order to determine the population of each output state, these states are spatially separated by application of the Stern-Gerlach method followed by the free-fall expansion and then imaged. Below we give details of each of these tasks.

Preparation of the initial state

For the initial state we use our ^{87}Rb BEC in $m_F = 2$. The U-shape conductor was used for the RF atom evaporation to a BEC of 3×10^4 atoms with a critical temperature of $0.5 \mu\text{K}$. The condensate was formed at the distance of $200 \mu\text{m}$ from the chip surface. Axial and transversal trap frequencies were 76 Hz and 935 Hz , respectively. For each measurement a new condensate was created. The purity of the initial state $m_F = 2$ was ensured by two considerations: one indication of this purity is coming from the fact if we optically pump the atoms to the $|F = 1, m_F = -1\rangle$ instead of applying the pumping used for BEC production, no atoms were observed during the magnetic catching. The total potential, including an effective gravity potential, proved by the atoms in the $|F = 1, m_F = -1\rangle$ is not deep enough to trap them. Hence,

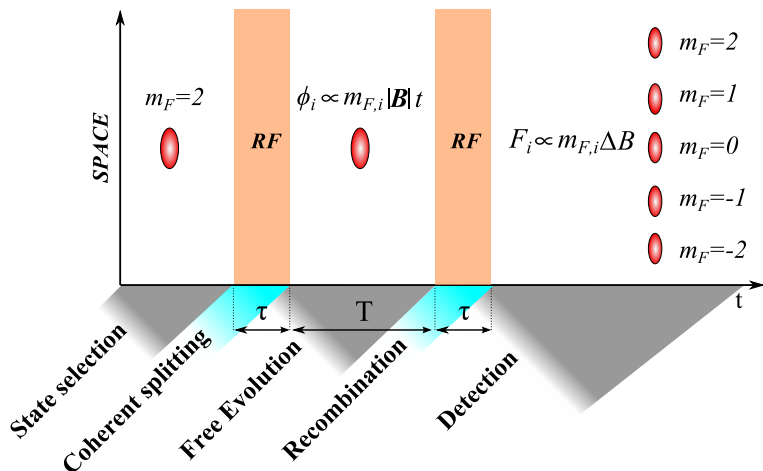


Figure 5.2: The sequence begins by a production of the initial BEC in the $|F = 2, m_F = 2\rangle$ state. The second step is a coherent splitting of the initial BEC state into BECs in other Zeeman states of the same hyperfine level. It is effected by a RF pulse, whose Rabi frequency Ω and duration τ determine the populations and initial phases of the interferometric paths. During a time T , different Zeeman states experience different potentials and hence accumulate different phases. The second RF pulse recombines these states and maps the phase differences into populations. A two-step detection scheme is applied. The states are first separated by a magnetic field gradient and are then detected by the absorption imaging.

if some atoms were in the $|F = 2, m_F = 1\rangle$ after the magnetic pumping, they would be lost in the magnetic catching, because the effective potential is not enough to hold them. Another possible cause to have atoms in the incorrect state is the RF evaporation ramp, the RF field used for the last cooling stage drive the atoms between the different m_F states. But the long time of the RF ramp, 2.5 seconds, secure us that no atoms will be in the $m_F = 1$ state.

Coherent manipulation

A pulse of frequency 700 kHz, which is matched to the separation of the Zeeman sublevels at the bottom of the magnetic trap, was used to split the atomic cloud coherently into the different sublevels.

The RF magnetic field was supplied by a waveform generator connected to a U-shape conductor in the chip holder (3), Fig. 5.3. The use of the U-shape conductor as antenna instead of an external antenna gives us two advantages.

5. ATOM CHIP MULTI-STATE INTERFEROMETER

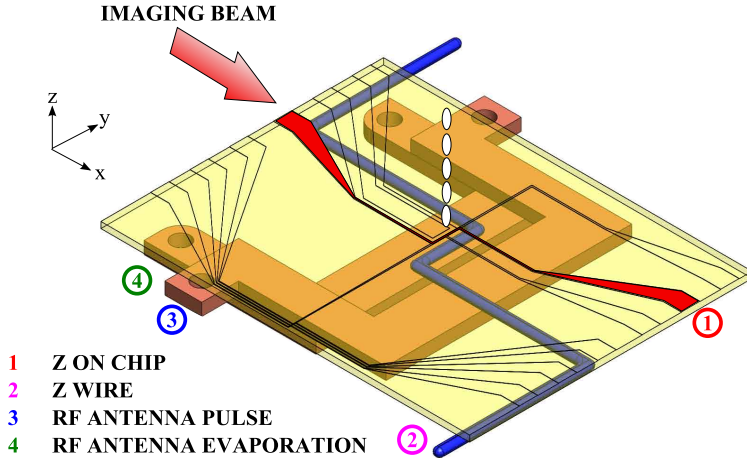


Figure 5.3: The elements of the atom chip interferometer. Magnetic trap on chip was formed by a micrometer z-wire (1) and was loaded from an ancillary magnetic trap formed by a millimeter Z-shape wire (2). Two U-shape conductors served as RF antennas for Rabi pulses (3) and evaporative cooling (4). All Zeeman states were simultaneously detected by applying Stern-Gelach deflection and subsequent absorption imaging. The z axis points in the direction of gravity.

First, its proximity to the atoms helps to increase the coupling of the wave to the atoms without the use of an amplifier system usually needed by external antennas. Second, external antennas could limit the optical access to the glass cell, while in our case the optical access remains intact.

The pulse consisted of 25 RF cycles and was short enough to cover the $\approx 10\text{kHz}$, energy spread of atoms in the BEC, see Section 4.8. A pulsed waveform has a spread in the frequency domain. Its spectrum is represented by a sinc function centered on the carrier frequency with small lobes at its sides, see Fig. 5.4. The width $\Delta\nu$ of the main lobe is $2/\tau$, whereas the width of a side lobe is $1/\tau$. The time scale τ is given by n/ν , where n is the number of cycles and ν is the frequency.

We note that the RF pulses were not locked in phase, but were phase locked to their respective trigger signals.

The relative phases between the states are accumulated due to the presence of the trapping magnetic field \mathbf{B} . In this field Zeeman states experience different potentials given by $V = m_F g_F \mu_0 |B|$ where m_F and g_F are respectively the spin and Landé numbers and μ_0 is the Bohr magneton. Therefore,

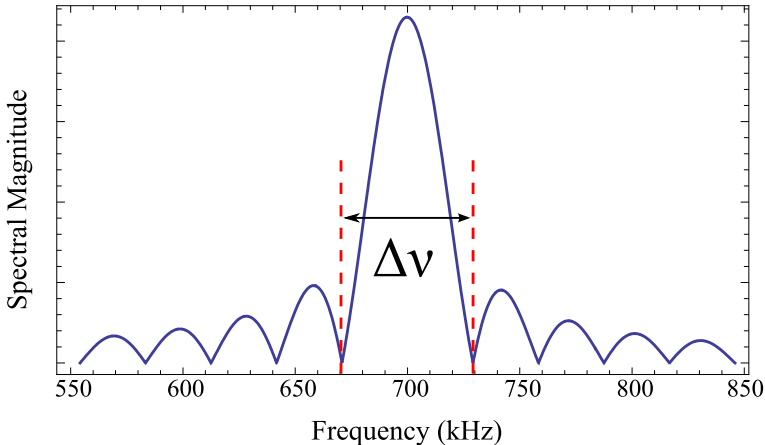


Figure 5.4: Sidelobes generated by an RF pulse of 25 cycles at a frequency of 700 kHz. The width of the central peak is with $\Delta\nu = 56\text{kHz}$ sufficient to address all atoms of the condensate.

their relative phases evolve with frequencies equal to multiples of the energy separation between adjacent levels $\omega = g_F\mu_0|\mathbf{B}|/\hbar$, yielding the interference signals rich in harmonics. These harmonics cause the fringe width to decrease with the number of states, which is the basic characteristic of a multi-state interferometer. If an external signal is applied during the delay between the two RF pulses, it will contribute to the relative phases accumulated between the states causing a shift in the fringe positions at the output. We measured spectroscopically the magnetic field stability. Its results were better than 1 mG.

Detection

The distribution of atoms across the Zeeman states was detected by the 7.5X-magnifying absorption imaging system with the imaging beam set to the $|F = 2\rangle \rightarrow |F = 3\rangle$ transition and the high dynamic range camera. Prior to the imaging the Zeeman states were spatially separated by the Stern-Gerlach method using a chip z-wire gradient. The atom number in each state was divided by the total atom number, thus rendering insignificant the measurement-to-measurement fluctuations in the BEC atom number. The measurements were repeated at least 3 times at each point. For each measurement a new BEC was created. The error of the population ratio measurement was 5%.

5. ATOM CHIP MULTI-STATE INTERFEROMETER

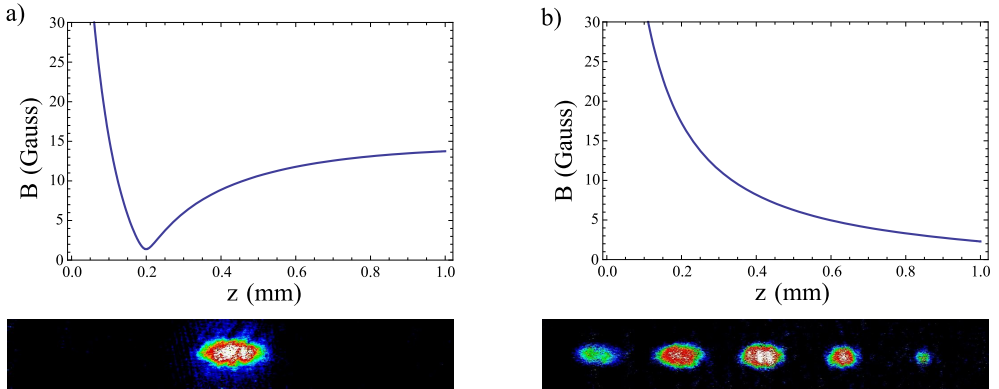


Figure 5.5: The plots show z-wire on chip magnetic fields with bias (a) and without bias (b) yielding a Stern-Gerlach type gradient. The detection of all the Zeeman states was performed by the usual absorption imaging. Under the plots an image of the absorption imaging is show for each situation.

5.5 Theoretical model

The proposed interferometer can be mathematically described by a transfer matrix J that acts on the atom-state wave-function vector

$$\Psi(t) = (\Psi_1(t), \Psi_2(t), \dots, \Psi_M(t))^T. \quad (5.8)$$

It is a product of the matrices R that correspond to the coupling Rabi pulses and the operator P that describes evolution of the states between the pulses, $J = RPR$. The matrix P is a diagonal matrix that adds a phase ϕ_n to the n^{th} state during the delay T between the pulses, $P_{n,n} = \exp(-iE_n T/\hbar)$ where E_n is the energy of the n^{th} Zeeman level. The matrix R is derived by solving the time dependent Schrödinger equation for M Zeeman states

$$i\hbar \frac{d\Psi(t)}{dt} = H\Psi(t), \quad (5.9)$$

where H is the three-diagonal Hamiltonian that couples the neighbouring m_F states. The coupling strength can be obtained by applying the angular-momentum algebra and the rotating-wave approximation [107, 108] and is

given by

$$H_{F,m_F} = \sqrt{F(F+1) - m_F(m_F+1)} \hbar\Omega/2, \quad (5.10)$$

where Ω is the Rabi frequency. For calculation, it is convenient to relabel the $|F, m_F\rangle$ states into $|N = 2F + 1, n = F + 1 + m_F\rangle$. This transformation gives

$$H_{n,n+1} = H_{n+1,n} = \sqrt{n(N-n)} \Omega/2 \quad (5.11)$$

$$H_{n,n} = \Delta_n \quad (5.12)$$

for the non-zero terms of the final model Hamiltonian, where Δ_n is the detuning of the RF field from the Zeeman transition and δ the Kronecker symbol [109, 110]. The spin system is a special periodic case of a generally quasi-periodic multi-level system [109, 111].

The Rabi pulse transfer matrix R can be found by diagonalization of \hat{H} using the method described in [109] or its generalization given in [111]. The output of the interferometer is then easily calculated by application of the transfer matrix J

$$J_{j,k} = \sum_{l=1}^M R_{j,l} e^{-i(l-1)\Delta E T/\hbar} R_{l,k} \quad (5.13)$$

to the input state vector. The interferometer output has a form of a finite Fourier series whose terms correspond to the multiples of the energy difference ΔE between adjacent Zeeman states in a magnetic field. The pulse area $\Omega\tau$ of the coupling pulse determines the number of populated states and, therefore, the number of harmonics. In general, an increase in the number of states M leads to an increase in the number of available harmonics, thus enabling further sharpening of the interferometric fringes. We note that the transfer function given by (5.13) is analogous to that of a Fabry-Pérot interferometer with a limited number of passes.

The simple model described above neglects atom-atom interactions and the relative motion of the condensates in different states. For the experimental setup used here, the collisionless model is valid due to a relatively small number of atoms in the condensate, while the stationary-condensate picture is justified for the short time delays during which movements of the condensates in their respective potentials do not degrade the fringe visibility. In the cases in which these effects are present, the full Gross-Pitaevskii equation that includes many-

body effects and the exact magnetic potentials should be used [57].

5.6 Results

Efficient use of the five Zeeman levels critically depends on the availability of atoms in these levels between the two RF pulses and therefore on the population transfer effected by the first Rabi pulse. The role of the Rabi pulses is analogous to the role of beam splitters in a Mach-Zehnder interferometer. However, here we can control the splitting by varying the pulse parameters, a feature not easily achievable in standard optical setups. The dependence of the interferometer signal on the Rabi pulse area can be understood from figure 5.6. The graph shows the measured and calculated population transfers between all five Zeeman states by a single Rabi pulse. The graphs in figure 5.7 show characteristic output signals of the interferometer and the raw absorption images from which these signals were derived for different $\Sigma\tau$.

In the experiment, the pulse duration was kept constant, while a range of Rabi pulse frequencies was sampled by changing the amplitude of the RF pulse. Sampling was random in order to reduce the effect of drifts in the setup. The scaling factor s between the RF voltage V and the Rabi pulse area, $\Omega\tau = sV$, was obtained by fitting the measured to the calculated populations in all m_F states. This simple calibration was sufficient to get an excellent agreement between the experiment and theory. Results confirm the periodicity of the coupled spin system and the characteristic features of Rabi coupling.

The Rabi pulse that populates only the highest or the lowest Zeeman states yields interferometric fringes with low visibility that approaches zero in the case of a nearly complete population cycle, figure 5.6(c). Well defined narrow interferometric fringes with enhanced sensitivity can be generated by those pulses that populate most Zeeman states as then the biggest number of harmonics allowed by the system contributes to the output signal, see figure 5.7 (a)–(c).

The performance of the interferometer in terms of sensitivity and visibility was evaluated through a comparison with an ideal 2-state interferometer. First, the available $\Omega\tau$ range of the 5-state interferometer was scanned to find the interferometer output with the sharpest fringes. The best result was obtained by Rabi pulses with an area of 3.3π (line with crosses in figure 5.8). The measured signal compares well to the theoretical result obtained for the

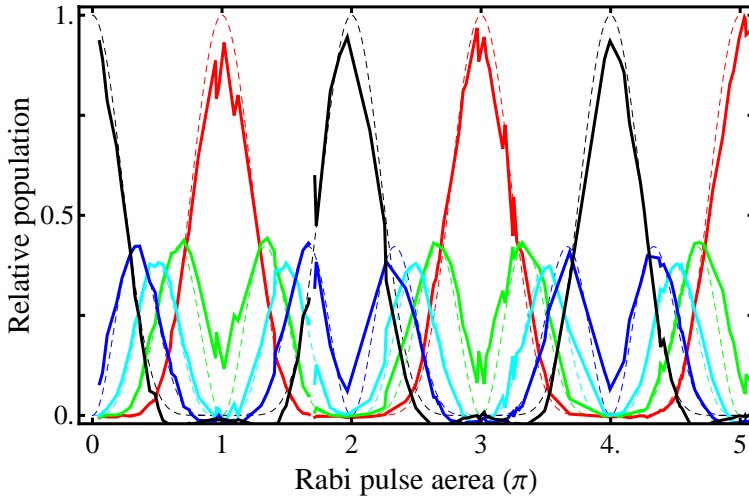


Figure 5.6: Rabi pulse population transfer between $m_F = 2$ (red), $m_F = 1$ (dark blue), $m_F = 0$ (light blue), $m_F = -1$ (green) and $m_F = -2$ (black) states as a function of the pulse area. Averaged experimental data are shown by solid lines and the simulation results by dashed lines. RF pulses consisted of 45 full cycles at 720 kHz.

same $\Omega\tau$ and, indeed, with the visibility close to 1 surpassed the theoretical prediction (solid line). The presence of a background in the theoretical signal can be attributed to the simplifications of the model discussed in Section 5.5. The corresponding fringe slope was measured to be $0.63 \pm 0.09 \text{ rad}^{-1}$ which is larger than the 0.5 rad^{-1} slope of an ideal 2-state interferometer. The estimated error is due to the population measurement error and residual magnetic field fluctuations. The increase in slope shows that the presented 5-path interferometer can be adjusted to achieve a resolution beyond that of an ideal 2-state interferometer. Finally, we note that the best measured signal approaches the optimal theoretical signal of a 5-state interferometer obtained for the given range of $\Omega\tau$ and input condition (dashed line).

Visibility is defined as $V = (A_{max} - A_{min}) / (A_{max} + A_{min})$ where A_{min} and A_{max} are the minimal and maximal output signal amplitudes.

To compare fairly the sensitivity of the realized interferometer with an ideal one, the same conditions for the population measurement must be assumed for both. The population measurement is limited by the shot noise, which in the case of an M -state interferometer causes a \sqrt{M} reduction in the signal-to-

5. ATOM CHIP MULTI-STATE INTERFEROMETER

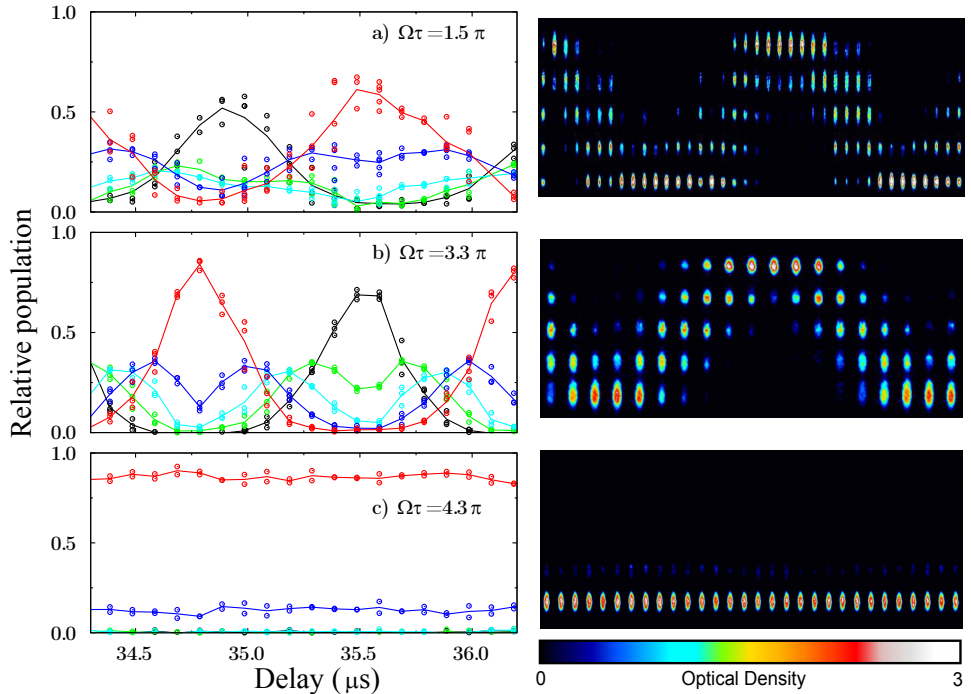


Figure 5.7: Left graphs: State populations at the output of the interferometer obtained from the absorption images by integration and normalization to the total number of atoms. The results are shown for RF-pulse areas of a) 1.5π , b) 3.3π , c) 4.3π . Color code is as in Fig. 5.6 Right figures: Raw absorption images of the interferometer output for the different RF-pulse areas at different time delays between the two Rabi pulses. Black color corresponds to the lowest atom density, red color to the highest one. The $m_F = 2$ state corresponds to the bottom row of atom clouds, the $m_F = -2$ state to the top row.

noise (S/N) ratio. For a 5-state interferometer the S/N is thus 1.58 times worse than for the 2-state interferometer. This means that, although the slope of the realized 5-state interferometer is 1.26 times steeper than of the ideal 2-state interferometer, the sensitivity of the ideal 2-state interferometer has not been overcome and that, therefore, the primary applications of the interferometer are those that require fringe narrowing.

The experimental optimization above was performed in Fabry-Pérot fashion with the highly asymmetric wavefunction at the input of the interferometer. An alternative is to start with a symmetric state, e.g. $m_F = 0$, and aim for

the fringe densification in an analogy with the multi-photon states in quantum optics [95, 112]. However, such experiments may be only possible in an optical trap that can trap all m_F states. We also note that the numerical optimization can be improved by employing recently developed optimization algorithms described in [113].

However, we have not improved the sensitivity beyond the shot noise limit. This is due to the slow increase in the fringe slope for small M with respect to the \sqrt{M} scaling of noise. For $M = 5$ the ideal slope of 0.82 rad^{-1} allows for the realization and detection of an improvement only if the measurement error is below 3%. Such a precision was not reachable in our measurements.

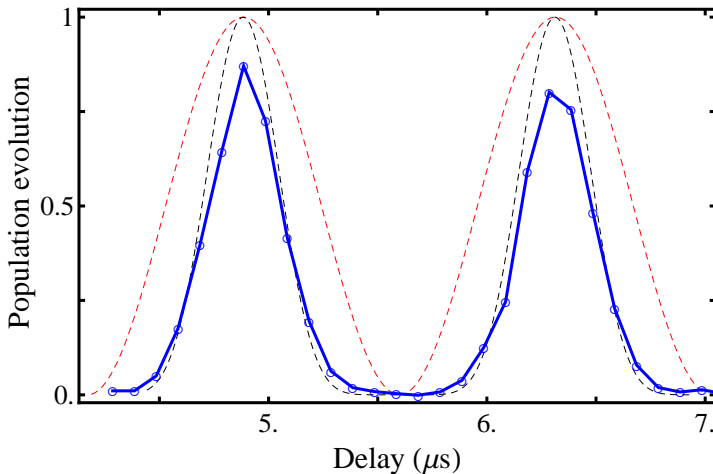


Figure 5.8: Interferometric signals for the $m_F = 2$ state. Blue circles show the best signal obtained in experiments (the blue solid line serves to guide the eye). This signal was obtained for $\Omega\tau = 1.55\pi$. Dashed black line shows the corresponding theoretical signal. For comparison, the optimal 2-state interferometer is also shown (red solid line). The realized 5-state interferometer has 1.75 times higher resolution than the ideal 2-state interferometer.

A remarkable feature of our interferometer is that the enhancement of resolution is achieved without reduction in visibility. Indeed, the full transfer of atoms from $m_F = 2$ to $m_F = -2$ and vice versa, see Fig. 5.7a), confirms the coherence of the transfer and renders the fringe visibility of 1 within the 5% experimental error. The maximum visibility is maintained for delays between the pulses of up to $50 \mu\text{s}$. For longer delays it decays exponentially with the

5. ATOM CHIP MULTI-STATE INTERFEROMETER

time decay constant of $100 \mu\text{s}$. The decay pattern showed in Fig. 5.9 for the state $m_F = 2$ is also followed by all the other states.

The decay in visibility can be attributed to the dephasing induced by additional phases accumulated during the motion of the condensates in the magnetic field [106] and by atom-atom interactions [97, 99]. The former is specific to the interferometer proposed here while the latter pertains to all interferometers with dense cold-atom gases.

Different Zeeman states experience different potentials in the same magnetic field. The condensates created by the first Rabi pulse move towards the minima of their respective potentials with different accelerations. Thereby the accumulated phase across the condensate is state dependent and affects the constructive interference between condensates in different states, for evolution times longer than $50 \mu\text{s}$. Moreover, the initial total overlap of the condensates decreases and the untrapped atoms in $m_F = 0$ and high-field seeking states eventually leave the trapping region.

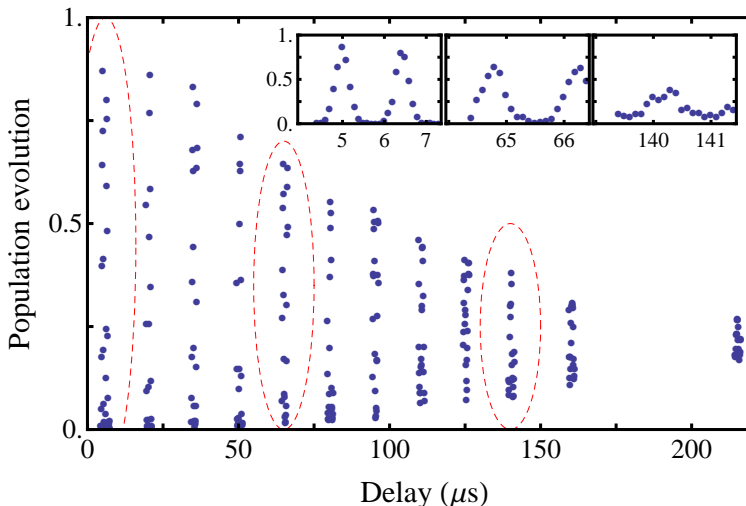


Figure 5.9: The $m_F = 2$ interferometer output at various time delays. The insets show zoom-ins on parts of the signal. Oscillatory behavior persists for delays longer than $200 \mu\text{s}$, but with a reduced fringe visibility. The observed decay in visibility is contributed mainly to the dephasing between atoms in different m_F states due to the relative phases that they accumulate during evolution and motion in their different magnetic potentials. Similar decay patterns are followed by the other m_F states.

We assessed the impact of interactions on the observed decay in visibility by comparing the interferometer made with the BEC with an interferometer made with a coherent thermal cloud with tens of times lower density. The thermal cloud was trapped in a less tight magnetic trap ($\nu_{\perp} = 574$ Hz) which additionally lowered the collision rate. The half-maximum decay time of the order of $60 \mu\text{s}$ was significantly shorter than the decay time of the BEC interferometer, indicating that the interactions are not responsible for the observed decay in visibility. Instead, the larger aperture of the thermal-cold trap causes larger relative displacements of the state-dependent potentials and hence faster dephasing. We can, therefore, conclude that the relative movement of the different m_F condensates in state-dependent potentials is the main cause of the loss of visibility. This result is in agreement with the result of [106]. Such dephasing can be ultimately avoided by performing the measurements in a optical dipole trap and in a constant bias magnetic field. Moreover, since the collisions do not significantly degrade the performance of the interferometer, they can be used to induce entanglement between atoms in different states, and hence further increase the sensitivity towards and beyond the standard quantum limit.

Applications of the proposed interferometer are based on the different responses of the Zeeman states to an external field. Due to the simultaneous measurement of populations of different states, the interferometer can be used in two basic measurement configurations: absolute measurement in which the signal is defined as a shift of fringes belonging to a chosen state, and differential measurement in which the signal is defined as the difference in shifts of fringes belonging to different states. An obvious application of the former is in a magnetometer in which the magnetic field magnitude directly maps into the periodicity of the fringes. Other applications are in the measurement of parameters of light-atom interactions, for example the relative atomic polarizability, and of light signals.

A potential disadvantage of the proposed sensor is its cross-sensitivity to the magnetic field. This problem can be resolved by using the differential measurement. In a magnetic field all fringes experience the same shift which cancels out in the differential signal. The remaining shift contains only the desired information on the state-dependent interaction of atoms with the external field. The elimination of the cross-sensitivity is paid by a decrease in sensitivity and

5. ATOM CHIP MULTI-STATE INTERFEROMETER

is thus more efficient for higher number of states and well-defined fringes.

We note that a strong interaction can distort the fringes making the read-out of the signals difficult. However, this does not have severe consequences as it limits the application of the interferometer exactly to the regime in which it performs best, in the small-signal regime in which the high sensitivity is required.

6

Conclusions

The combination of Bose-Einstein condensates and atom chips opens up a huge range of possibilities. Here I will briefly describe the latest work we are doing, and the directions that the experiment may take in the future.

In this thesis I have described the preparation of one of the first Bose-Einstein condensates to be made on an atom chip. The condensate contained 3×10^4 ^{87}Rb atoms, and formed at temperatures below 500 nK. It was prepared just 200 μm from a room temperature (290 K) substrate.

Atom sensors with confined particles and waveguides realize the matter wave analogous of optical sensors using fiber-optic devices. Matter wave based sensors represent frontier instruments for a wealth of novel applications ranging from sensing accelerations and rotations to monitoring quantum decoherence, characterizing atomic and molecular properties, and measuring fundamental constants. With respect to free-space structures integrated waveguides are much smaller, robust and easier to realize and operate. Furthermore they offer the possibility of precisely knowing the position of atoms, therefore allowing superior control and eventually the ability to manipulate the atomic states. The possibility of precisely controlling the position of a coherent system could allow fundamental test such as those to put limits on the existence of a fifth force or short range forces therefore testing quantum gravity. These novel devices open new fundamental questions about atom-surface interactions while at the same time offering the possibility to look for answers by a careful analysis of the coherence properties of atoms and atomic superpositions confined inside the microtraps. Finally the same structures that allow guiding coherent atoms

6. CONCLUSIONS

allow a consistent reduction of experimental complexity in the realization of coherent atomic samples thus making these devices perfect candidates for any potential industrial application following the scientific and technical advance in the field of ultracold matter.

Degenerate quantum gases are conventionally investigated via imaging techniques based either on light absorption or on fluorescence. Via release expansion it is possible to use these techniques to obtain a precise mapping of the atom distribution in phase space. By a careful analysis of the atomic distribution after expansion it is also possible to extract information about correlations in the atomic cloud. We intend to move a step forward by taking advantage of the many internal degrees of freedom available in atomic systems to develop atomic interferometric techniques capable of giving a direct access to macroscopic quantum properties. These would be the analogous of an optical homodyne techniques where degenerate atoms in different internal states would take the role of the local oscillator and atomic internal states would allow for balanced detection.

Atom Chips have already revolutionized the field of quantum degenerate gases allowing a great experimental simplification. Thanks to the components miniaturization, one can reach extremely large magnetic field gradients (in the order of Tesla/cm) with a few Ampere current, similar to those flowing in ordinary electronic circuits. Already very compact and robust systems have been realized and Atom Chip based experiments are so robust that can be actually used in free falling experiments. Atom Chips have also been tested as time references and as a source for atom interferometry. Being very compact they also provide a starting point for the implementation of more complicating devices by scaling up from simple structures. In our laboratory at LENS, an Atom Chip experiment, where a Bose-Einstein condensate of rubidium atoms are produced in a magnetic trap generated by microscopic wires laid on a planar surface, is already at an advanced stage. Our experimental configuration offers a very large optical access can be adapted to combine optical elements in close proximity to the atomic sample.

The integration of the interferometer with an atom chip offers several technical advantages. The small wires allow for fast switching of the magnetic fields, and shortening the experimental cycle several times with respect to the free-space setups. This is of particular importance for time-domain interfer-

ometers in which the signal is constructed from a series of measurements at different time delays. The proximity of the condensate to the chip wires enables large field gradients that facilitate imaging of the Zeeman states. The chip device is robust, easy-to-use, and a good candidate for future portable cold-atom sensors. Finally, the advantage of the described interferometer, that applies equally to non-chip setups, is that it does not use light signals and therefore does not suffer from instabilities related to the optical alignment.

To conclude, a compact time-domain multi-state interferometer on an atom chip whose sensitivity can be controlled by an RF pulse acting as a variable beam splitter. In the optimal configuration it has the resolution superior to that of an ideal two-path interferometer. The simultaneous measurement of multiple signals at the output enables a range of advanced sensing applications in atomic physics and optics, while the integration of the interferometer with an chip brings it into consideration for future portable cold-atom based measurement apparatuses. The presented multi-state interferometric scheme can be generalized to other atomic species, any BEC setup, and is compatible with a quantum state preparation. Moreover, the analogies of the couplers used here with a BEC in an optical lattice and optical waveguide arrays indicate the universality of the proposed scheme.

6. CONCLUSIONS

7

Conclusiones

La unión de los condensados de Bose-Einstein con los "atom chips" abre un amplio abanico de posibilidades. A continuación describiré brevemente nuestros resultados mas recientes así como las direcciones que el experimento pueda tomar en un futuro.

En esta tesis he descrito la preparación de uno de los primeros condensados de Bose-Einstein hecho con un "atom chip". El condensado tiene unos 3×10^4 átomos de ^{87}Rb , y se forma con una temperatura de 500 nK. Este fue hecho a una distancia de 200 μm de una superficie a temperatura ambiente (290 K).

La integración del interferómetro con un atom chip ofrece numerosas ventajas técnicas. Los pequeños conductores permiten cambios veloces en el campo magnéticos asi como el acortar los ciclos experimentales con respecto a un aparato experimental. Estos es de particular importancia para los "time-domain" interferómetros en los cuales la señal esta construida con una serie de medidas a diferentes tiempos. La proximidad del condensado a los conductores del chip permite grandes gradientes de campo que facilitan la detección de los diferentes estados Zeeman. El "atom chip" es un sistema robusto, fácil de usar, y un buen candidato para un futuro sensor de átomos fríos transportable. Finalmente la ventaja del inteferómetro descrito se pude aplicar igualmente a otros aparatos que no estén basados en el "atom chip", pero estos al estar basados en luz presentan una la complicación de delicados alineamientos ópticos.

Concluyendo, se ha construido un interferómetro compacto a multi-estado en el "time-domain" en un atom-chip, cuya sensibilidad puede ser controlada por un pulso de RF que haría las veces de un "beam splitter" variable. En

7. CONCLUSIONES

la configuración óptima este tiene una resolución superior a un interferómetro ideal a dos caminos. La medidas simultaneas de múltiples señales abre a todo un abanico de aplicaciones avanzadas de "sensing" en el campo de la física atómica y óptica, mientras que la integración de un interferómetro ad alta sensibilidad con el atom chip hace pensar en futuros aparatos transportables basados en átomos fríos. El interferometro a multi-estado aquí presentado, puede sÍer generalizado a otras especies atómicas y otros aparatos BEC. Por otra parte, las analogas del interferómetro a múltiples caminos con otros sistemas como el condensado en una red óptica o series de guías de onda ópticas, indica la universalidad del esquema propuesto.

References

- [1] J. REICHEL, W. HÄNSEL, P. HOMMELHOFF, AND T. W. HÄNSCH. **Applications of integrated magnetic microtraps.** *Applied Physics B: Lasers and Optics*, **72**(1):81–89, 2001. 1, 26, 30, 32
- [2] RON FOLMAN, PETER KRÉJČER, JILĚRG SCHMIED-MAYER, JOHANNES DENSCHLAG, AND CARSTEN HENKEL. **Microscopic atom optics: From wires to an atom chip.** **48**:263 – 356, 2002. 1, 2, 26, 29
- [3] J. FORTĚGH AND C. ZIMMERMANN. **Magnetic microtraps for ultracold atoms.** *Rev. Mod. Phys.*, **79**:235, 2007. 1
- [4] M. H. ANDERSON, J. R. ENSHER, M. R. MATTHEWS, C. E. WIEMAN, AND E. A. CORNELL. **Observation of bose-einstein condensation in a dilute atomic vapor.** *Science*, **269**(5221):198–201, July 1995. 1, 18
- [5] K. DAVIS, M. MEWES, M. ANDREWS, N. VAN DRUTEN, D. DURFEE, D. KURN, AND W. KETTERLE. **Bose-Einstein Condensation in a Gas of Sodium Atoms.** *Physical Review Letters*, **75**(22):3969–3973, November 1995. 1, 18, 23, 44
- [6] J REICHEL, W HÄNSEL, AND T W HÄNSCH. **Atomic Micromanipulation with Magnetic Surface Traps.** *Physical Review Letters*, **83**(17):3398–3401, 1999. 1, 114, 117, 118
- [7] H. OTT, J. FORTÁGH, G. SCHLOTTERBECK, A. GROSSMANN, AND C. ZIMMERMANN. **Bose-Einstein Condensation in a Surface Microtrap.** *Physical Review Letters*, **87**(23):230401, November 2001. 1, 50
- [8] W. HÄNSEL, J. REICHEL, P. HOMMELHOFF, AND T. HÄNSCH. **Trapped-atom interferometer in a magnetic microtrap.** *Physical Review A*, **64**(6), November 2001. 1, 30, 50
- [9] J. RINGOT, P. SZRIFTGISER, AND J. C. GARREAU. **Subrecoil Raman spectroscopy of cold cesium atoms.** *Phys. Rev. A*, **65**:013403, Dec 2001. 2
- [10] W D PHILLIPS, J PRODAN, AND H J METCALF. *J. Opt. Soc. Am. B*, **2**:1752, 1985. 5, 23
- [11] STEVEN CHU. **Nobel Lecture: The manipulation of neutral particles.** *Reviews of Modern Physics*, **70**(3):685–706, July 1998. 5
- [12] H. J. METCALF AND P. VAN DER STRATEN. *Laser cooling and trapping.* Springer-Verlag, 1999. 5, 7, 8, 10, 36
- [13] C S ADAMS AND E RIIS. **Laser Cooling and Trapping of Neutral Atoms.** *Prog. Quant. Electr.*, **21**:1, 1997. 7, 9, 10
- [14] T W HÄNSCH AND A SCHAWLOW. *Opt. Comm.*, **13**:68, 1975. 8
- [15] J DALIBARD AND C COHEN-TANNOUJDI. *J. Opt. Soc. Am. B*, **6**:2023, 1989. 9, 10, 12
- [16] P UNGAR, D WEISS, AND S CHU. *J. Opt. Soc. Am. B*, **6**:2058, 1989. 9
- [17] E. L. RAAB, M. G. PRENTISS, A. CABLE, S. CHU, AND D. E. PRITCHARD. **Trapping of Neutral Sodium Atoms with Radiation Pressure.** *Physical Review Letters*, **59**(23):2631–2634, 1987. 14, 117
- [18] P ZEEMAN. **Atoms Atoms in in Magnetic Magnetic Field.** *System*. 15
- [19] W. PETRICH AND ET. AL. **Behaviour of atoms in a compressed magneto-optical trap.** *J. Opt. Soc Am. A*, **11**:1332, 1994. 17, 18
- [20] C. G. TOWNSEND, N. H. EDWARDS, C. J. COOPER, K. P. ZETIE, C. J. FOOT, A. M. STEANE, P. SZRIFTGISER, H. PERRIN, AND J. DALIBARD. **Phase-space density in the magneto-optical trap.** *Physical Review A*, **52**(2):1423–1440, 1995. 17
- [21] A. M. STEANE AND C. J. FOOT. **Laser Cooling below the Doppler Limit in a Magneto-Optical Trap.** *Europhysics Letters (EPL)*, **14**(3):231–236, February 1991. 17
- [22] W. KETTERLE, K. B. DAVIS, M. A. JOFFE, A. MARTIN, AND D. E. PRITCHARD. **High densities of cold atoms in a dark spontaneous-force optical trap.** *Physical Review Letters*, **70**(15):2253–2256, 1993. 18
- [23] C. E. WIEMAN, G. FLOWERS, AND S. GILBERT. **Inexpensive laser cooling and trapping experiment for undergraduate laboratories.** *American Journal of Physics*, **63**(4):317–330, 1995. 22
- [24] W. KETTERLE AND D. E. PRITCHARD. **Trapping and focusing ground state atoms with static fields.** *Applied Physics B: Lasers and Optics*, **54**(5):403–406, 1992. 22
- [25] E MAJORANA. *Nuovo Cimento*, **9**:43, 1932. 22
- [26] H J METCALF. *Nat. Bur. Stand. (U.S.) Spec. Publ.*, **635**:59, 1983. 22

REFERENCES

- [27] ALAN MIGDALL, JOHN PRODAN, WILLIAM PHILLIPS, THOMAS BERGEMAN, AND HAROLD METCALF. **First Observation of Magnetically Trapped Neutral Atoms.** *Physical Review Letters*, **54**(24):2596–2599, June 1985. 23
- [28] W. PETRICH, M. H. ANDERSON, J. R. ENSHER, AND E. A. CORNELL. **Stable, Tightly Confining Magnetic Trap for Evaporative Cooling of Neutral Atoms.** *Physical Review Letters*, **74**(17):3352–3355, 1995. 23, 114
- [29] W. KETTERLE, D. S. DURFEE, AND D. M. STAMPER-KURN. **Making, probing and understanding Bose-Einstein condensates, in Bose-Einstein condensation in atomic gases.** In *Proceedings of the International School of Physics "Enrico Fermi"*. 23
- [30] Y GOTT, M IOFFE, AND V TEL'KOVSKII. *Nucl. Fusion, 1962 Suppl.*, Pt. 3:1045, 1962. 24
- [31] D. E PRITCHARD. **Cooling Neutral Atoms in a Magnetic Trap for Precision Spectroscopy.** *Physical Review Letters*, **51**(15):1336–1339, October 1983. 24
- [32] M.-O. MEWES, M. ANDREWS, N. VAN DRUTEN, D. KURN, D. DURFEE, AND W. KETTERLE. **Bose-Einstein Condensation in a Tightly Confining dc Magnetic Trap.** *Physical Review Letters*, **77**(3):416–419, July 1996. 24
- [33] J. SÖDING, D. GUÉRY-ODELIN, P. DESBIOLLES, G. FERRARI, AND J. DALIBARD. **Giant Spin Relaxation of an Ultracold Cesium Gas.** *Physical Review Letters*, **80**(9):1869–1872, March 1998. 24
- [34] TILMAN ESSLINGER, IMMANUEL BLOCH, AND THEODOR HÄNSCH. **Bose-Einstein condensation in a quadrupole-Ioffe-configuration trap.** *Physical Review A*, **58**(4):R2664–R2667, October 1998. 24
- [35] T. BERGEMAN, GI. EREZ, AND H. J. METCALF. **Magnetostatic trapping fields for neutral atoms.** *Physical Review A*, **35**(4):1535–1546, February 1987. 24
- [36] K. L. MOORE, T. P. PURDY, K. W. MURCH, K. R. BROWN, K. DANI, S. GUPTA, AND D. M. STAMPER-KURN. **Bose-Einstein condensation in a mm-scale Ioffe-Pritchard trap.** *Applied Physics B: Lasers and Optics*, **82**(4):533–538, 2006. 25
- [37] GOV S., S. SHRIKMAN, AND H. THOMAS. **Magnetic trapping of neutral particles: Classical and quantum-mechanical study of a Ioffe-Pritchard type trap.** *J. Appl. Phys.*, **87**:3989, 2000. 25
- [38] D SOKOLOVSKI. **Path integrals and equations of motion for the traversal-time distributions in classical diffusion and quantum mechanics.** *Physical Review A*, **52**(1):R5—R8, July 1995. 25, 34
- [39] S WILDERMUTH, P KRÜGER, C BECKER, M BRADJIC, S HAUPT, A KASPER, R FOLMAN, AND J SCHMIEDMAYER. **Optimized magneto-optical trap for experiments with ultracold atoms near surfaces.** *Physical Review A*, **69**(3):30901, 2004. 29, 62
- [40] K. BRUGGER, T. CALARCO, D. CASSETTARI, R. FOLMAN, A. HAASE, B. HESSMO, P. KRÜGER, T. MAIER, AND J. SCHMIEDMAYER. **Nanofabricated atom optics: atom chips.** *J. Mod. Opt.*, **47**:2789, 2000. 29
- [41] P. KRÜGER, X. LUO, P. BRUGGER, K. WILDERMUTH, S. GIMPEL, H. S. KLEIN, M. W. GROTH, R. FOLMAN, I. BAR-JOSEPH, AND J. SCHMIEDMAYER. **Atom fiber for omnidirectional guiding of cold neutral atoms.** *Opt. Lett.*, **29**:2145, 2004. 30
- [42] DONATELLA CASSETTARI, BJÖRN HESSMO, RON FOLMAN, THOMAS MAIER, AND JÖRG SCHMIEDMAYER. **Beam Splitter for Guided Atoms.** *Physical Review Letters*, **85**(26):5483–5487, December 2000. 30
- [43] P. HOMMELHOFF, W. HÄNSEL, T. STEINMETZ, T. W. HÄNSCH, AND J. REICHEL. **Transport, splitting and merging of atomic ensembles in a chip trap.** *J. Phys.*, **7**:3, 2005. 30
- [44] C. HENKEL, S. PÖTTING, AND M. WILKENS. **Loss and heating of particles in small and noisy traps.** *Applied Physics B: Lasers and Optics*, **69**(5):379–387, 1999. 32
- [45] D. M. HARBER, J. M. MCGUIRK, J. M. OBRECHT, AND E. A. CORNELL. **Thermally Induced Losses in Ultra-Cold Atoms Magnetically Trapped Near Room-Temperature Surfaces.** *Journal of Low Temperature Physics*, **133**(3):229–238, 2003. 33, 76
- [46] M. P. A. JONES, C. J. VALE, D. SAHAGUN, B. V. HALL, AND E. A. HINDS. **Spin Coupling between Cold Atoms and the Thermal Fluctuations of a Metal Surface.** *Physical Review Letters*, **91**(8):80401, 2003. 33
- [47] Y.-J. LIN, I. TEPER, CHENG CHIN, AND V. VULETIĆ. **Impact of the Casimir-Polder Potential and Johnson Noise on Bose-Einstein Condensate Stability Near Surfaces.** *Physical Review Letters*, **92**(5):50404, February 2004. 33
- [48] J FORTÁGH, H OTT, S KRAFT, A GÜNTHER, AND C ZIMMERMANN. **Surface effects in magnetic microtraps.** *Physical Review A*, **66**(4):41604, 2002. 33
- [49] A. E. LEANHARDT, A. P. CHIKKATUR, D. KIELPINSKI, Y. SHIN, T. L. GUSTAVSON, W. KETTERLE, AND D. E. PRITCHARD. **Propagation of Bose-Einstein Condensates in a Magnetic Waveguide.** *Physical Review Letters*, **89**(4):40401, July 2002. 33, 146

- [50] A. LEANHARDT, Y. SHIN, A. CHIKKATUR, D. KIELPINSKI, W. KETTERLE, AND D. PRITCHARD. **Bose-Einstein Condensates near a Microfabricated Surface.** *Physical Review Letters*, **90**(10), March 2003. 33
- [51] S. KRAFT, A. GÜNTHER, H. OTT, D. WHARAM, C. ZIMMERMANN, AND J. FORTÁGH. **Anomalous longitudinal magnetic field near the surface of copper conductors.** *Journal of Physics B: Atomic, Molecular and Optical Physics*, **35**:L469–L474, 2002. 33, 60, 146
- [52] J. ESTÈVE, C. AUSSIBAL, T. SCHUMM, C. FIGL, D. MAILLY, I. BOUCHOULE, C. I. WESTBROOK, AND A. ASPECT. **Role of wire imperfections in micromagnetic traps for atoms.** *Physical Review A*, **70**(4):43629, 2004. 33, 60
- [53] C. DURKAN, M. A. SCHNEIDER, AND M. E. WELLAND. **Analysis of failure mechanisms in electrically stressed Au nanowires.** **86**(3):1280–1286, 1999. 34
- [54] M. DRNDIC, K. S. JOHNSON, J. H. THYWISSEN, M. PRENTISS, AND R. M. WESTERVELT. **Microelectromagnets for atom manipulation.** *Applied Physics Letters*, **72**(22):2906–2908, 1998. 34
- [55] S. GROTH, P. KRUIĽGER, S. WILDERMUTH, R. FOLMAN, T. FERNHOLZ, J. SCHMIEDMAYER, D. MAHALU, AND I. BAR-JOSEPH. **Atom chips: Fabrication and thermal properties.** *Applied Physics Letters*, **85**(14):2980, April 2004. 34
- [56] V. BAGNATO, D. E. PRITCHARD, AND D. KLEPPNER. **Bose-Einstein condensation in an external potential.** *Physical Review A*, **35**(10):4354–4358, May 1987. 38
- [57] FRANCO DALFOVO, STEFANO GIORGINI, LEV P. PITAEVSKII, AND SANDRO STRINGARI. **Theory of Bose-Einstein condensation in trapped gases.** *Reviews of Modern Physics*, **71**(3):463–512, April 1999. 38, 41, 164
- [58] HUANG. *Statistical mechanics.* John Wiley and sons New York, 1987. 39
- [59] J. R. ENSHER, D. S. JIN, M. R. MATTHEWS, C. E. WIEMAN, AND E. A. CORNELL. **Bose-Einstein Condensation in a Dilute Gas: Measurement of Energy and Ground-State Occupation.** *Physical Review Letters*, **77**(25):4984–4987, 1996. 41
- [60] GOLDMAN, VICTOR V., SILVERAV F., ISAAC, LEGGETT, AND ANTHONY J. **Atomic hydrogen in an inhomogeneous magnetic field: Density profile and Bose-Einstein condensation.** *Phys. Rev. B*, **24**(5):2870–2873, 1981. 41
- [61] O. J. LUITEN AND ET. AL. **Kinetic theory of the evaporative cooling of a trapped gas.** *Physical Review A*, **53**:381, 1996. 44
- [62] D. SNOKE AND J. WOLFE. **Population dynamics of a Bose gas near saturation.** *Physical Review B*, **39**(7):4030–4037, March 1989. 45
- [63] J. P. BURKE, J. L. BOHN, B. D. ESRY, AND C. H. GREENE. **Prospects for Mixed-Isotope Bose-Einstein Condensates in Rubidium.** *Physical Review Letters*, **80**(10):2097–2100, March 1998. 47
- [64] A. MARTE, T. VOLZ, J. SCHUSTER, S. DÜRR, G. REMPE, E. G. M. VAN KEMPEN, AND B. J. VERHAAR. **Feshbach Resonances in Rubidium 87: Precision Measurement and Analysis.** *Phys. Rev. Lett.*, **89**:283202, Dec 2002. 47
- [65] S. AIGNER, L. D. PIETRA, Y. JAPHA, O. ENTIN-WOHLMAN, T. DAVID, R. SALEM, R. FOLMAN, AND J. SCHMIEDMAYER. **Long-Range Order in Electronic Transport Through Disordered Metal Films.** *Science*, **319**(5867):1226–1229, 2008. 60
- [66] Y. JAPHA, O. ENTIN-WOHLMAN, T. DAVID, R. SALEM, S. AIGNER, J. SCHMIEDMAYER, AND R. FOLMAN. **Model for organized current patterns in disordered conductors.** *Phys. Rev. B*, **77**(20):201407, May 2008. 60
- [67] S. SCHNEIDER. **Bose-Einstein Kondensation in einer magnetischen Z-Falle,** 2003. 63
- [68] S. SCHNEIDER, A. KASPER, CH. VOM HAGEN, M. BARTENSTEIN, B. ENGESER, T. SCHUMM, I. BAR-JOSEPH, R. FOLMAN, L. FEENSTRA, AND J. SCHMIEDMAYER. **Bose-Einstein condensation in a simple microtrap.** *Physical Review A*, **67**(2):23612, February 2003. 63
- [69] D. E. PRITCHARD, K. HELMERSON, AND A. MARTIN. World Scientific, Singapore, 1989. 76
- [70] T. W. HIJMANS, O. J. LUITEN, I. D. SETIJA, AND J. T. M. WALRAVEN. **Optical cooling of atomic hydrogen in a magnetic trap.** *J. Opt. Soc. Am. B*, **6**(11):2235–2243, November 1989. 76
- [71] W. KETTERLE, K. B. DAVIS, M. A. JOFFE, A. MARTIN, AND D. E. PRITCHARD. **invited oral presentation at OSA Annual Meeting,** 1993. 76
- [72] D. STECK. **Rubidium 87 D Line Data.** 2001. 79
- [73] W. DEMTRÖDER. *Laser spectroscopy: basic concepts and instrumentation.* Advanced texts in physics. Springer, 2003. 90
- [74] C. E. WIEMAN AND T. W. HÄNSCH. **Doppler-Free Laser Polarization Spectroscopy.** *Physical Review Letters*, **36**(20):1170–1173, May 1976. 90

REFERENCES

- [75] JUNG BOG KIM, HONG JIN KONG, AND SANG SOO LEE. **Dye laser frequency locking to the hyperfine structure ($3S_{1/2}$, $F=2 - 3P_{1/2}$, $F=2$) of sodium D_{1} line by using polarization spectroscopy.** *Appl. Phys. Lett.*, **52**(6):417–419, 1988. 90
- [76] LANCASTER G. P. T. AND ET. AL. **A polarization locked diode laser for trapping cold atoms.** *Opt. Comm.*, 1999. 90
- [77] K LINDQUIST, M STEPHENS, AND C E WIEMAN. **Experimental and theoretical study of the vapor cell Zeeman optical trap.** *Physical Review A*, **46**:4082, 1992. 119
- [78] Y. CASTIN AND R. DUM. **Bose-Einstein Condensates in Time Dependent Traps.** *Physical Review Letters*, **77**(27):5315–5319, 1996. 148
- [79] PIETRO LOMBARDI FRANCESCO S. CATALIOTTI JOVANA PETROVIC, IVAN HERRERA. **A Multi-Path Interferometer on an Atom Chip Condensation.** *Preprint*, arXiv:1111.4321/physics.atom-ph, 2011. 153
- [80] M. R. ANDREWS. **Observation of Interference Between Two Bose Condensates.** *Science*, **275**(5300):637–641, January 1997. 153
- [81] ALEXANDER D. CRONIN AND DAVID E. PRITCHARD. **Optics and interferometry with atoms and molecules.** *Reviews of Modern Physics*, **81**(3):1051–1129, July 2009. 153, 157
- [82] C GROSS, T ZIBOLD, E NICKLAS, J ESTÈVE, AND M OBERTHALER. **Squeezing and entanglement in a Bose-Einstein condensate.** *Nature*, **464**:1165, 2010. 153, 154
- [83] M F RIEDEL, P BÖHI, Y LI, T W HÄNSCH, A SINATRA, AND P TREUTLEIN. **Atom-chip-based generation of entanglement for quantum metrology.** *Nature*, **464**:1170, 2010. 153
- [84] S. GUPTA, K. DIECKMANN, Z. HADZIBABIC, AND D. PRITCHARD. **Contrast Interferometry using Bose-Einstein Condensates to Measure h/m and α .** *Physical Review Letters*, **89**(14), September 2002. 153, 155
- [85] RYM BOUCHENDIRA, PIERRE CLADÉ, SAÏDA GUELLATI-KHÉLIFA, FRANÇOIS NEZ, AND FRANÇOIS BIRABEN. **New Determination of the Fine Structure Constant and Test of the Quantum Electrodynamics.** *Physical Review Letters*, **106**(8), February 2011. 153
- [86] D. HARBER, H. LEWANDOWSKI, J. MCGUIRK, AND E. CORNELL. **Effect of cold collisions on spin coherence and resonance shifts in a magnetically trapped ultracold gas.** *Physical Review A*, **66**(5), November 2002. 153
- [87] A PETERS, K Y CHUNG, AND S CHU. *Metrologia*, 2001. 153
- [88] S MERLET, Q BODART, N MALOSSI, A LANDRAGIN, F PEREIRA DOS SANTOS, O GITLEIN, AND L TIMMEN. *Metrologia*, 2010. 153
- [89] J B FIXLER, G T FOSTER, J M MCGUIRK, AND M A KASEVICH. **Atom interferometer measurement of the newtonian constant of gravity.** *Science*, **315**(5808):74–7, January 2007. 153
- [90] T. L. GUSTAVSON, P. BOUYER, AND M. A. KASEVICH. **Precision Rotation Measurements with an Atom Interferometer Gyroscope.** *Physical Review Letters*, **78**(11):2046–2049, March 1997. 154
- [91] A. PETERS AND K. Y. CHUNG. **Measurement of gravitational acceleration by dropping atoms.** *Nature*, 1999. 154
- [92] VITTORIO GIOVANNETTI, SETH LLOYD, AND LORENZO MACCONE. **Quantum-enhanced measurements: beating the standard quantum limit.** *Science*, **306**(5700):1330–6, November 2004. 154
- [93] G WEIHS, M RECK, H WEINFURTER, AND A ZEILINGER. *Opt. Lett.*, 1996. 154
- [94] M. WEITZ, T. HEUPEL, AND T. HÄNSCH. **Multiple Beam Atomic Interferometer.** *Physical Review Letters*, **77**(12):2356–2359, September 1996. 154, 155
- [95] MITCHELL M. W., J S LUNDEEN, AND A M STEINBERG. *Nature*, 2004. 154, 167
- [96] B. P. ANDERSON. **Macroscopic Quantum Interference from Atomic Tunnel Arrays.** *Science*, **282**(5394):1686–1689, November 1998. 155
- [97] M. FATTORI, G. ROATI, B. DESSLER, C. D’ÁZZERRICO, M. ZACCANTI, M. JONASINIO, L. SANTOS, M. INGUSCIO, AND G. MODUGNO. **Magnetic Dipolar Interaction in a Bose-Einstein Condensate Atomic Interferometer.** *Physical Review Letters*, **101**(19), November 2008. 155, 168
- [98] HOLGER MÜLLER, SHENG-WEY CHIOU, QUAN LONG, SVEN HERRMANN, AND STEVEN CHU. **Atom Interferometry with up to 24-Photon-Momentum-Transfer Beam Splitters.** *Physical Review Letters*, **100**(18), May 2008. 155
- [99] M GUSTAVSON, E HALLER, M J MARK, J G DANZL, R HART, A J DALEY, AND H C NÄGERL. *New J. Phys.*, 2010. 155, 168
- [100] TAKATOSHI AOKI, KENJI SHINOHARA, AND ATSUO MORINAGA. **High-finesse atomic multiple-beam interferometer comprised of copropagating stimulated Raman-pulse fields.** *Physical Review A*, **63**(6):63611, May 2001. 155

-
- [101] H. HINDERTHÜR, F. RUSCHEWITZ, H.-J. LOHE, S. LECHTE, K. SENGSTOCK, AND W. ERTMER. **Time-domain high-finesse atom interferometry.** *Physical Review A*, **59**(3):2216–2219, March 1999. 155
- [102] J. SACHARIAS S. MILLMAN RABI, I. AND P. KUSCH. **A new method for measuring nuclear magnetic moments.** *Physical Review Letters*, 1938. 155
- [103] N. RAMSEY. **A new molecular beam resonance method.** *Physical Review Letters*, 1938. 155
- [104] MARLAN O. SCULLY AND M. SUHAIL ZUBAIRY. *Quantum Optics*. Oxford Univeristy Press, New York, 1997. 156
- [105] *Molecular Beams*. Clarendon, Oxford, 1956. 156
- [106] F. MINARDI, C. FORT, P. MADDALONI, M. MODUGNO, AND M. INGUSCIO. **Time-Domain Atom Interferometry across the Threshold for Bose-Einstein Condensation.** *Physical Review Letters*, **87**(17):1–4, October 2001. 158, 169
- [107] *Atomic Physics*. Oxford University Press, 2005. 162
- [108] W KETTERLE AND N VAN DRUTEN. **37.** Academic, San Diego, 1996. 162
- [109] COOK R. J. AND SHORE B. *Phys. Rev. A*, **20**:539, 1979. 163
- [110] BRUCE W. SHORE. **Dynamics of multilevel laser excitation: Three-level atoms.** *Acta Phys. Slov*, **58**:243, 2008. 163
- [111] VITANOV N V AND SUOMINEN K-A. *Phys. Rev. A*, **56**:R4377, 1997. 163
- [112] BANASZEK K., R DEMKOWICZ-DOBZĄŃSKI, AND I A WALMSLEY. *Nature Photonics*, 2009. 167
- [113] PATRICK DORIA, TOMMASO CALARCO, AND SIMONE MONTANGERO. **Optimal Control Technique for Many-Body Quantum Dynamics.** *Physical Review Letters*, **106**(19), May 2011. 167

Matter-wave interferometry is a powerful tool for high-precision measurements of the quantum properties of atoms, many-body phenomena and gravity. The most precise matter-wave interferometers exploit the excellent localization in momentum space and coherence of the degenerate gases. Further enhancement of sensitivity and reduction of complexity are crucial conditions for success and widening of their applications.

On the cover: State populations at the output of the interferometer obtained from the absorption images by integration and normalization to the total number of atoms.